MEASUREMENT OF THERMO-MECHANICAL PROPERTIES OF CO-SPUTTERED SiO_2-Ta_2O_5 THIN FILMS

Dissertation

Submitted to

The School of Engineering of the

UNIVERSITY OF DAYTON

In Partial Fulfillment of the Requirements for

The Degree of

Master of Science in Electro-Optics

By

Maggie E. Lankford

Dayton, Ohio

August, 2021

MEASUREMENT OF THERMO-MECHANICAL PROPERTIES OF CO-SPUTTERED SiO_2-Ta_2O_5 THIN FILMS

Name: Lankford, Maggie E.

AFRL-2021-2237

APPROVED BY:

Andrew Sarangan, Ph.D.
Advisory Committee Chairman
Professor and Chair, Department of Electro-Optics and Photonics

Jonathan Vernon, Ph.D.
Committee Member
Senior Materials Research Engineer, Air Force Research Laboratory

Lirong Sun, Ph.D.
Committee Member
Optical Scientist, Azimuth Corporation

Christopher Muratore, Ph.D.
Committee Member
Associate Professor, Department of Chemical and Materials Engineering

Robert J. Wilkens, Ph.D., P.E.
Associate Dean for Research and Innovation
Professor
School of Engineering

Margaret F. Pinnell, Ph.D.
Interim Dean, School of Engineering

© Copyright by

Maggie E. Lankford

All rights reserved

2021

ABSTRACT

MEASUREMENT OF THERMO-MECHANICAL PROPERTIES OF CO-SPUTTERED SiO_2-Ta_2O_5 THIN FILMS

Name: Lankford, Maggie E.
University of Dayton

Advisor: Dr. Andrew Sarangan

The durability of thin film optical interference filters, integrated in systems ranging from imaging sensors to energy-efficient IR-blocking windows, is affected by its stress. The purpose of this work is to explore the thermal stress in thin films, the result of a contrast in the coefficient of thermal expansion (CTE) between the substrate and the film. While much research is focused on film intrinsic stress, thermal stress should also be considered for systems designed for high temperature variability and for systems where the film and substrate material properties vary greatly.

This work characterizes the coefficient of thermal expansion and the Young's Modulus of SiO_2 and Ta_2O_5 films, common low and high-index optical materials, along with composite SiO_2-Ta_2O_5 thin films grown by reactive co-sputtering. A model for the variation of the CTE as a function of film composition is proposed, showing general agreement with the measured data.

Characterization of the thermal stress in the film-substrate system is measured using a custom-built instrument, and the Young's Modulus is verified using nano-indentation. A method for evaluating the instrument noise, and its effect on the precision of the calculated CTE and Modulus values is characterized for this instrument. A model is proposed to enhance future designs-of-experiment using this instrument.

This work is dedicated to my mother Sylvia Lankford Hadley, and to my father Larry Lankford, who tirelessly emphasized the importance and value of higher education, and who made it possible for me to pursue it.

ACKNOWLEDGMENTS

There are many people whose guidance and assistance made this work possible. I would first like to thank Walt Johnson, who first conceived of this research topic, and who encouraged me to pursue it, asking insightful questions along the way. Thank you also to Dr. Lirong Sun, who with her seemingly endless patience, taught me about sputtering deposition and assisted me in troubleshooting an unfamiliar deposition chamber so that I could fabricate thin films for study. Her mentorship in the lab spared me a great deal of painful mistakes, and spurred ahead my interest and understanding in the field.

A great deal of thanks goes to Randy Hall, who custom-built the experimental equipment that was used to measure thermal stress, and then taught me how to use it. His expertise and knowledge of experimental physics is inspiring. I would also like to thank Dr. Bill Southwell, who spent a great deal of time mentoring me through both the theoretical understanding of thin films and error analysis. He, together with Randy Hall and Walt Johnson taught me the importance and the value of determining the right questions, because only then can you start to get the right answers.

I would also like to show my appreciation for those working at the Air Force Research Laboratory, especially Dr. Matthew Lange, Nicolas Garvin, and Dr. John Jones whose encouragement and support were critical to my success.

Thank you also to Dr. Andrew Sarangan, whose guidance helped me navigate the thesis process and who provided valuable feedback in the compilation of this document. And I have much gratitude to Rosey Lawandi who, on short notice, took the time in her busy schedule to teach me how to use the EDAX system to measure my samples, and then to help me understand the results.

I would like to extend my thanks also to those on my committee, Dr Andrew Sarangan, Dr. Jonathan Vernon, Dr. Lirong Sun, and Dr. Christopher Muratore. I appreciate your interest in my work, and valued your feedback.

A very special thank you goes to UES, Inc who financially supported this research work.

And last but certainly not least, I would like to thank my husband, Robert Bacheller, who has truly witnessed both the joys and trials that have come during this project, and whose love, care, encouragement, and patience supports me each day.

TABLE OF CONTENTS

ABSTRACT iii

DEDICATION iv

ACKNOWLEDGMENTS v

LIST OF FIGURES ix

LIST OF TABLES xiii

CHAPTER I. INTRODUCTION 1

CHAPTER II. DEPOSITION OF THIN FILMS 6

2.1 Theory of Reactive Pulsed DC Magnetron Sputtering 6
2.2 Details of the Vacuum Sputter System 15
2.3 Deposition Parameters and Samples Fabricated 18

CHAPTER III. OPTICAL CHARACTERIZATION OF THE CO-SPUTTERED THIN FILMS 24

3.1 Theory of Spectroscopic Ellipsometry 24
3.1.1 Measurement of Ellispometric Parameters 25
3.1.2 Kramers-Kronig Relations 30
3.1.3 Optical Dispersion Analysis Techniques 32
3.2 Effective Medium Theory 36
3.3 Modeled Optical Properties of Fabricated Films 40
3.4 Additional Methods of Characterization for Material Composition 47
3.4.1 Dispersion Fits Using Reflection Spectra 47
3.4.2 Verification of Film Composition using EDX 51

CHAPTER IV. THEORY FOR CALCULATING THIN FILM THERMO-MECHANICAL PROPERTIES 53

4.1 Theory of Stress in Thin Films 53
4.2 Determination of Total Film Stress through Substrate Bending 59
4.3 Coefficient of Thermal Expansion (CTE) and Young's Modulus (E) Calculations from Thermal Stress 65
4.3.1 Calculation of CTE and Young's Modulus using the Two-Substrate Method 66
4.3.2 Calculation of CTE from Single-Substrate Method 68
4.3.3 Incorporation of Uncertainty from Two Measurement Sources . . 68

CHAPTER V. MEASUREMENTS OF THIN FILM THERMO-MECHANICAL PROPERTIES 70

5.1 Thermal Stress Measurement Technique 70

5.1.1 Instrumentation 71
5.1.2 Temperature Cycling Profile 76
5.1.3 Thermal Stress Calculation from Measured Data 79
5.1.4 Evaluation of Instrument Noise 85
5.2 Sensitivity Analysis: Methods to Increase the Signal-to-Noise Ratio . . . 86
5.2.1 Evidence in Support of the Sensitivity Model 93
5.3 Two-Substrate Method: Calculation of CTE & Young's Modulus 95
5.4 Young's Modulus Measurement Technique 100
5.5 Single-Substrate Method: Calculation of CTE using Measured Modulus . 108

CHAPTER VI. CONCLUSION 113

BIBLIOGRAPHY 119

LIST OF FIGURES

2.1 Diagram of the magnetron which contains the plasma to the target region. Part a) shows the magnetic field caused by the presence of the magnets, and part b) shows a silicon target that has been worn in the characteristic "racetrack" pattern. 8

2.2 This is a conceptual diagram which demonstrates the trends for sputter yield and gas/metal ratio in a re actively sputtered film as a function of reactive gas pressure. Part a) shows the metal flux, or in other words, the sputter yield, as a function of reactive gas pressure, while part b) shows that there is a minimum reactive gas pressure which results in a film of ideal stiochiometry [1]. 10

2.3 This demonstrates the build up of charge along an insulating surface layer of the cathode or target (left) and compares to the situation without the build-up of an insulating layer where electrons and ions recombine and neutralize (right). . 13

2.4 A diagram of the magnetron sputter chamber. [2] 14

2.5 The voltage profile of the TruPlasma pulsed DC power supply [3]. 16

2.6 Images of each of the samples made for this work. 22

3.1 A diagram of the reflections from the two interfaces present in a transparent thin film scenario. 25

3.2 A diagram of the determination of the total reflection and total transmission of a beam at oblique incidence on a substrate with a thin film [4]. 28

3.3 An example of anomalous dispersion of a material with three absorption resonances. The real part shown here is the index of refraction, while the imaginary part is the absorption coefficient. These are both shown as a function of frequency [5]. 32

3.4 Plots of a Lorentz absorption peak and a Tauc-modified Lorentz absorption peak. Center wavelength and bandgap are indicated and are the same for both cases. 36

3.5 A diagram of a unit cell with material "A" in host material "B", and resulting change in local field due to applied field. 38

3.6 The modelled dispersion curves for each of the 14 films characterized in this work. Each film is labeled by the target powers (W) that were used during film growth. 42

3.7 Modeled film composition and refractive index determined using the Bruggeman Effective Medium model in J.A. Woollam's CompleteEASE. 44

3.8 Modeled surface roughness versus modeled EMA composition, %SiO_2. 46

3.9 Two examples of the fits for the spectral reflectance. 49

3.10 The X-ray spectrometer counts versus energy (keV) for the X-rays emitted during EDX. 52

4.1 At left, compressive and tensile stress is shown in the film alone. The arrows indicate force direction, which are normal to the cross-sectional thickness. The right demonstrates that same film when applied to a substrate. The substrate will also be under tension (above) or compression (below) to balance out the stresses in the films. 54

4.2 A demonstration of the origins of thermal stress. The combination of differing CTE's between the substrate and film with high adhesion between them introduces curvature in the system. 56

4.3 Diagram of the strain in the substrate due to the stress of a compressive film. The horizontal arrows denote the force in the system. 61

5.1 The custom-designed beam-splitter used to create the dual-beam for the thermal stress measurements. Designs of the three applied interference coatings were done by Table Mountain Optics, and the filters were grown by LohnStar Optics, Inc. 72

5.2 Images of the exterior (left) and interior (right) of the environmental chamber. 74

5.3 An image of the exterior optics that are used in conjunction with the environmental chamber to measure the thermal stress of the samples. 74

5.4 Example of raw data for 9-Hr temperature cycling profile. Pixel separation shown in blue, temperature set-point shown in orange, reference optical flat shown by the dashed line. 77

5.5 Example of raw data for 10.5Hr temperature cycling profile. Pixel separation shown in blue, temperature set-point shown in orange, reference optical flat shown by the dashed line. 78

5.6 Thermal stress fits from measured data of SiO_2 on GaAs substrate. Top graph uses collected data and displays pixel separation versus temperature. Bottom graph converts the pixel separation into calculated curvature versus temperature. 80

5.7 The measured slopes and their associated errors plotted as a function of %SiO2 film composition. The top two plots show the measured slope, error bars demonstrating the standard error. On the left are the films on Si substrates, on the right are the films on GaAs substrates. The bottom two plots show the R^2 values of the linear best-fit slopes. 83

5.8 A diagram of the range of acceptable reported slopes with a variation of 1.9 pixels of noise. 86

5.9 The measured slopes and their associated errors, shown in conjunction with the calculated instrument noise threshold, shown as the dashed lines. 87

5.10 Plots for the "Rule of Mixtures" model for the Young's Modulus of the composite thin films, and the "Hall CTE Model" for the CTE of the composite thin films. 89

5.11 Required film thickness to be equal to the noise threshold of the instrument, for SiO_2-Ta_2O_5 composite films on 270um thick Si substrates (above), and 315um thick GaAs substrate (below). The orange line indicates the CTE contrast between the film and the substrate. The grey dots indicate the fabricated film thicknesses for this study. 92

5.12 Plots of Best-fit slopes and associated error for SiO_2 and Ta_2O_5 films of different thicknesses grown under both this program as well as [6]. 94

5.13 A histogram of he 2000 generated random numbers, with normal distribution centered around the best-fit slope, with a standard deviation equal to the standard error in the fit. The dashed lines represent a normal distribution with the properties outlined. 96

5.14 Calculated CTE vs. film composition using the two-substrate method. The top graph and the bottom graph hold the same data, but have different y-axis scales to highlight the uncertainty (top) and the calculated values (bottom). The dashed line represents the Hall CTE Model. 98

5.15 Calculated Young's Modulus using the Two-Substrate method. 99

5.16 A diagram of the nano-indentation process, along with a description of the Berkovich tip [7]. 101

5.17 Images of the iNano instrument exterior (left) and interior (right). 103

5.18 Young's Modulus determined using nano-indentation as a function of film composition. The dashed line indicates the "Rule of Mixtures" model. 104

5.19 The measured Hardness of the films, along with their reported uncertainty, using nano-indentation. The models compare the data with a linear mixing model and a modulus-weighted model. 106

5.20 Plot of the CTE vs. film composition, as calculated using the Single-Substrate method with Young's modulus measured with nano-indentation. 110

LIST OF TABLES

2.1 The deposition parameter set-points utilized in this study. 21

2.2 The deposition conditions under which the samples for this study were grown. 23

3.1 The modeled refractive index at 660 nm, the physical thickness of the films measured in nanometers, and the calculated optical thickness of the films, measured in nanometers. 44

3.2 The calculated MSE fits for the deposited films, calculated in connection with the dispersion curves shown in Figure 3.6. 47

5.1 The best-fit slope for thermal stress measurements, its error and its R^2 values for each measured sample. 83

5.2 Measured Young's Modulus, using the iNano nanoindenter, for both Si substrates and GaAs substrates, as compared to the calculated modulus using the two-substrate method. All values are reported in GPa unless otherwise stated. . . . 104

5.3 Measured Hardness, using the iNano nanoindenter, for both Si substrates and GaAs substrates. 107

5.4 Calculated CTE and uncertainty of each film using the Single-Substrate Method. All values are reported in units of ppm/°C unless otherwise stated. 110

CHAPTER I

INTRODUCTION

Thin film interference filters are the keys which unlock the potential of modern optical systems. Durable anti-reflection coatings allow for the design of complex, high-transmission optical systems, and spectral filters allow for a large range of applications from spectroscopy to energy-efficient IR-blocking windows.

Material properties such as index of refraction and absorption are critical to understanding the performance of thin film interference filters, and extensive research has been done in order to design and build these interference filters based on these properties. However, given the wide range of application for these filters, it is imperative also to understand the impact the coating material properties will have on the stress and durability of the systems into which they are incorporated.

Stress in thin films can be categorized into three areas: intrinsic, thermal, and applied stress. Intrinsic stress is the stress in the film due to the deposition process, thermal stress is the stress due to the difference in thermo-mechanical properties between the film and the substrate, and applied stress is any external force that is applied to the system which may come from handling or installing into a fixture.

In a significant fraction of the literature on stress in thin films, the thermal stress is ignored. However, this is not appropriate in applications with large temperature ranges or in applications where the system is comprised on materials with vastly differing thermo-mechanical properties.

There are many applications for thin film interference filters or thin films of dielectrics, where environmental durability under dramatically changing temperature conditions are of

critical importance. One example of this is the application of solar cells in space. Typical materials for these types of solar cells may be silicon, gallium arsenide, germanium, gallium indium phosphide, or a combination of these materials depending on cost and efficiency, as they all have bandgaps appropriate for absorption of solar radiation [8]. One of the key innovations which dramatically increases the efficiency of solar cells is the application of an anti-reflection coating on the surface of the solar cell. Typical broadband anti-reflection coatings are made by depositing an interference filter made from dielectric materials. Under most conditions, the relatively small difference in the thermal and mechanical properties between the semiconductor materials and the dielectrics (like SiO_2 and Ta_2O_5) will be negligible. However, the utilization of solar cells in space applications such as travel to and operation on Mars, requires great durability over an extended lifetime, and for space conditions, the temperature changes experienced by the semiconductor-dielectric system are dramatic. For instance, temperatures experienced on the surface of Mars range from −140°C (−284°F) to 30°C (86°F), and temperatures on the surface of Earth's moon swing from −183°C (−298°F) to 106°C (224°F) each day [9, 10].

To demonstrate a simple example of the effect that the thermal stress will play in the durability of these systems, consider an SiO_2 layer on a GaAs semiconductor. Using the material properties found in [11], an estimate of the thermal stress in a solar cell in operation on Mars would be approximately 50MPa from its day to night temperatures. Using the measurements from the same paper, the thermal stress in the solar cell on the Moon would be 80MPa. This can be compared to the intrinsic stress of the film, which is reported to range from 60-500MPa depending on the deposition processes outlined in [12]. In the scenario described in [12], where dense SiO_2 films had a stress of 60MPa, the thermal stress in the solar cell would be approximately equal to the intrinsic stress for Mars operation and

would exceed the intrinsic stress for Moon operation. In either scenario, and even for the high intrinsic stress films, the thermal stress is non-negligible, increasing the total stress by anywhere between 10% and 130%, depending on application. The successful operation of solar cells in these extraordinary temperature conditions requires thoughtful consideration, knowledge, and mitigation of thermal stress in the system. Thus an understanding of the thermal and mechanical properties of thin films can contribute to the increased durability and longevity of such systems.

There is another category of systems in which environmental durability is impacted by the thermo-mechanical properties of the materials incorporated in it. There are many systems in which materials of greatly differing mechanical properties are bonded together. One such example of this comes from a commonly-used re-writable compact discs (CD-RW and DVD-RW). Re-writable discs are typically made from a plastic substrate which is coated with a phase-change material, such as an alloy of germanium, indium, silver, antimony, and/or tellurium, which dramatically changes its optical properties between the crystalline and amorphous states [13]. This phase-change material is layered between two dielectric layers in order to control the heating of the recording medium. In order to write or erase the information on the disc, a laser is used to heat the phase-change material quickly to high temperatures causing it to change from transparent to absorbing. The longevity of the disk, and the number of re-writes that it can withstand are partially dependent on the durability of the multi-layered system which contains both elastic (plastic substrate) and inelastic (dielectric and phase-change) materials.

To demonstrate the magnitude of the thermal stress relative to intrinsic in this type of scenario, consider two cases: the phase-change material $Ge_2Sb_5Te_5$ (GST) bonded to an acrylic resin (plastic-like) dielectric heat-control layer, and second the phase-change material

GST bonded to an SiO_2 (glass-like) dielectric heat-control layer. It is common to use pulsed focused laser light to heat the phase-change material above its melting point to create an amorphous layer. Using published values of the melting point, the CTE and the Young's Modulus of crystalline GST [14, 15], and the CTE of both SiO_2 and Acrylic materials [11, 16], we can estimate that the GST bonded to the acrylic would have a thermal stress of 1.94GPa, and the GST bonded to the SiO_2 would have a thermal stress of 515MPa upon changing from the crystalline state to the amorphous state during writing of the data to the disc. This can be compared to a reported intrinsic stress of 214MPa for GST [17]. The thermal stress for the acrylic-GST system would be over nine times that of the intrinsic stress. Similarly, the thermal stress for the SiO_2-GST system would be nearly 2.5 times the intrinsic stress.

The change in expansion of these materials during rapid heating and cooling causes thermal stress in the system, which can induce fractures in the brittle layers over time due to cyclic fatigue. Understanding the mechanical and thermal properties of thin film dielectric materials is the first step to learning how to minimize thermal stress in such systems to increase longevity.

Here only two applications are detailed where understanding the thermal and mechanical properties of thin films are critical to the success and longevity of the systems, however they each demonstrate a category of system for which understanding and mitigating thermal stress in optical coatings creates the conditions for systems with better durability and longevity: a system which experiences large temperature variation, and a system which is made from materials with different thermal and mechanical properties. Interference filters are incorporated into almost all optical systems. In order to design and build filters with great environmental durability, one must consider both optical and thermo-mechanical

properties of the materials involved. Material properties such as the Coefficient of Thermal Expansion (CTE), and the Young's Modulus contribute to the thermo-mechanical properties of the interference filter, and must also be considered in the design of environmentally robust filters.

A great deal of consideration has been given to the understanding of the optical properties of common materials used in interference filters. However, the investigation of the thermo-mechanical properties of these materials is less studied.

In addition to discrete-layer spectral filters, there exists a category of interference filters which utilize gradient-index profiles. These gradient-index films are used for applications from narrow-band reflectors to novel anti-reflection coatings [18, 19]. In order to design and manufacture these gradient-index filters, the optical properties of the materials, as a function of mixed-oxide composition, are well understood and follow a theory called the Effective Medium Theory [20].

The goal of this work is to investigate the thermo-mechanical properties of two common high and low-index materials as a function of blending composition. SiO_2 and Ta_2O_5 will be used in this study, as they are commonly used materials for gradient index films, and their optical properties as a function of mixed-oxide composition are well-characterized [21, 22].

For this work, a series of depositions will be made where SiO_2 and Ta_2O_5 are co-sputtered together to form an effective medium of varying compositions ranging from 100% SiO_2 to 100% Ta_2O_5. The optical properties of these materials will be analyzed using the Effective Medium Theory (EMT), and the thermo-mechanical properties of coefficient of thermal expansion (CTE) and Young's Modulus will be measured in order to determine how these properties change as a function of film composition.

CHAPTER II

DEPOSITION OF THIN FILMS

This chapter will outline the theory of reactive pulsed DC magnetron sputtering and the deposition conditions used to fabricate the samples for this study.

2.1 Theory of Reactive Pulsed DC Magnetron Sputtering

Reactive pulsed DC magnetron sputtering is a process in which a material is atomized by ion collision with the "target" material. These atomized particles are ejected from the material toward the substrate. During the trajectory from the target to the substrate and at the substrate surface, the atomized particles interact with a reactive gas to condense and grow as a compound material on the substrate. Like many highly technical terms, the name "reactive pulsed DC magnetron sputtering" is a comprehensive descriptor of the processes involved. The following section will detail the physical phenomenon described by each word in this term, and fit them together to form a picture of the process more generally.

In general, magnetron sputtering falls under the category of physical vapor deposition, which is characterized by the creation of a gaseous material, which condenses on the substrate. This gaseous phase can be obtained using a variety of methods, including evaporation due to resistive heating or electron-beam heating, laser ablation, and sputtering [23].

For sputtering deposition, the energy source for the creation of the gaseous material is ion bombardment. Here the atoms of the target are ejected from momentum transfer from the ions. This deposition method is useful because the high momentum of the ejected particles results in a dense film at the substrate. In addition to this, the deposition can be

done at room temperature, which is the preferred method for oxides and nitrides which can decompose at elevated temperatures [23].

In order to have sputter deposition, there must be a sustained plasma located near the magnetron in order to have an ion source which will eject target material upon collision. The magnetron is also used as the cathode for a DC power supply. In order to ignite a plasma, the DC power supply is used to create a high voltage between the magnetron cathode and the substrate/chamber anode. This process is usually done under vacuum conditions, with a low pressure, inert argon gas. Free electrons in the vacuum chamber will accelerate between the cathode and anode due to the high electric potential. If they accelerate to a kinetic energy above the ionization energy of the Ar atoms in the chamber, they will ionize the Ar atoms upon collision. With each collision, an additional pair of free electrons and Ar ions are formed, which creates an avalanche effect. Some recombination of free electrons and Ar ions will occur, creating the characteristic plasma glow.

This process necessitates a precise balance between the electric potential, which accelerates the free electrons, and the Ar pressure. A high electric field is needed such that the electrons can accelerate past the ionization energy of the Ar atoms before collision, however in order to create the avalanche effect, the electrons must collide with an Ar atom before reaching the anode. The relationship between pressure and the required electric field to ionize the gas is described by Paschen's law [24]. If the ionization rate and the recombination rate are balanced, then the plasma will be stable and self-sustaining.

In order to sputter a material, the Ar ions created in the plasma will bombard the material of interest, called the "target" as it is the material to be deposited on the substrate. The plasma described above would naturally be resident over a large area between the

cathode and anode. However, the rate of ion bombardment of the target directly effects the rate of deposition of the target material. In order to increase the rate of ablation of the target material, a magnetron can be introduced behind the target in order to trap the plasma so that there is a high ion density close to the target.

The magnetron is a series of permanent magnets which are oriented so that alternate north and south pole ends are close to the target side. This creates a permanent magnetic field between the north and south poles of the magnets, as shown in Figure 2.1a [25]. Here the magnetic field is oriented perpendicular to the direction of the electric potential, and consequently the direction of travel of the electrons. Due to the nature of interaction between a traveling charged particle, and a constant magnetic field, as described by Maxwell's equations, the electrons will be trapped as they travel with helical motion along the magnetic field lines. Since the free electrons are responsible for the creation of Ar ions which sputter the target material, this will concentrate the plasma in the area of high magnetic field.

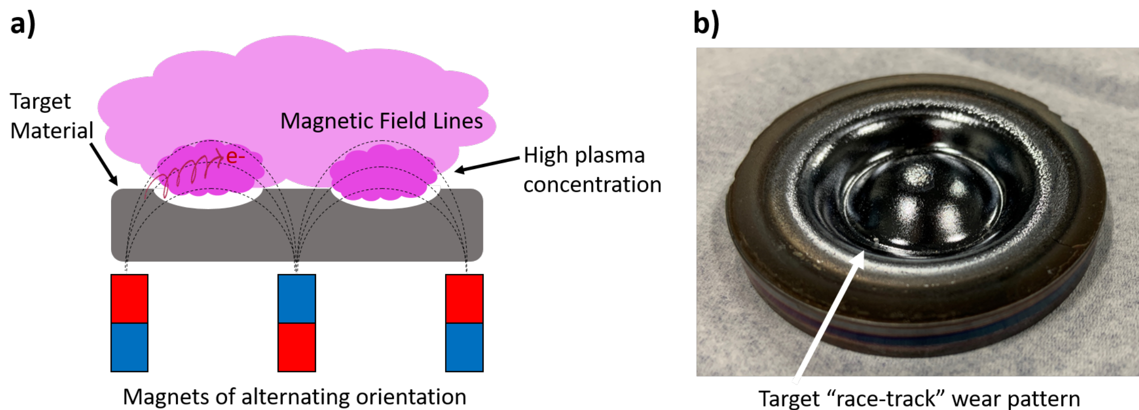

Figure 2.1: Diagram of the magnetron which contains the plasma to the target region. Part a) shows the magnetic field caused by the presence of the magnets, and part b) shows a silicon target that has been worn in the characteristic "racetrack" pattern.

For circular magnetron configurations, this is evidenced by a "race track" wear pattern which is observed as the target is used. The highest ablation of the target material occurs in regions with the highest magnetic field. For a circular magnetron, the magnetic field is radial due to the magnet configuration, which causes the greatest target ablation along a circular "race track" pattern as shown in Figure 2.1b [26].

For the materials used in this work, SiO_2 and Ta_2O_5, reactive magnetron sputtering is used. In order to deposit these oxide compounds onto the substrate, targets of silicon and tantalum are used. What makes the reactive sputtering different is that the vacuum is filled with a low pressure of a reactive gas, in this case oxygen. As the silicon and tantalum travels to, and arrives at the surface of the substrate, it reacts with the oxygen atmosphere to form SiO_2 and Ta_2O_5. Reactive sputtering is used in these cases, as the sputter yield of the silicon and the tantalum are greater than the sputter yield of their respective oxides [23]. This means that faster deposition rates can be achieved through reactive sputtering than with sputtering of the oxide itself.

The compound material composition on the substrate and the deposition rate are highly dependent on the partial pressure of the reactive gas in the chamber. There must be enough oxygen in the chamber to fully react the silicon and tantalum. However too much oxygen will result in the oxidization of the target material. This means that the sputtered material will be the compound oxide, as opposed to the target material. As mentioned before, the sputter yields of the compound oxides are much lower than of the elemental silicon and tantalum. Therefore the excess of oxygen in the chamber will decrease the sputter deposition rate. This is called "target poisoning" [1, 27]. The best oxygen flow rate is that where the oxidization rate of the target is similar to the sputter removal rate, so that there

is enough oxygen to create fully oxidized compounds, but maintain a reasonable deposition rate [23]. A diagram of this effect is shown in Figure 2.2.

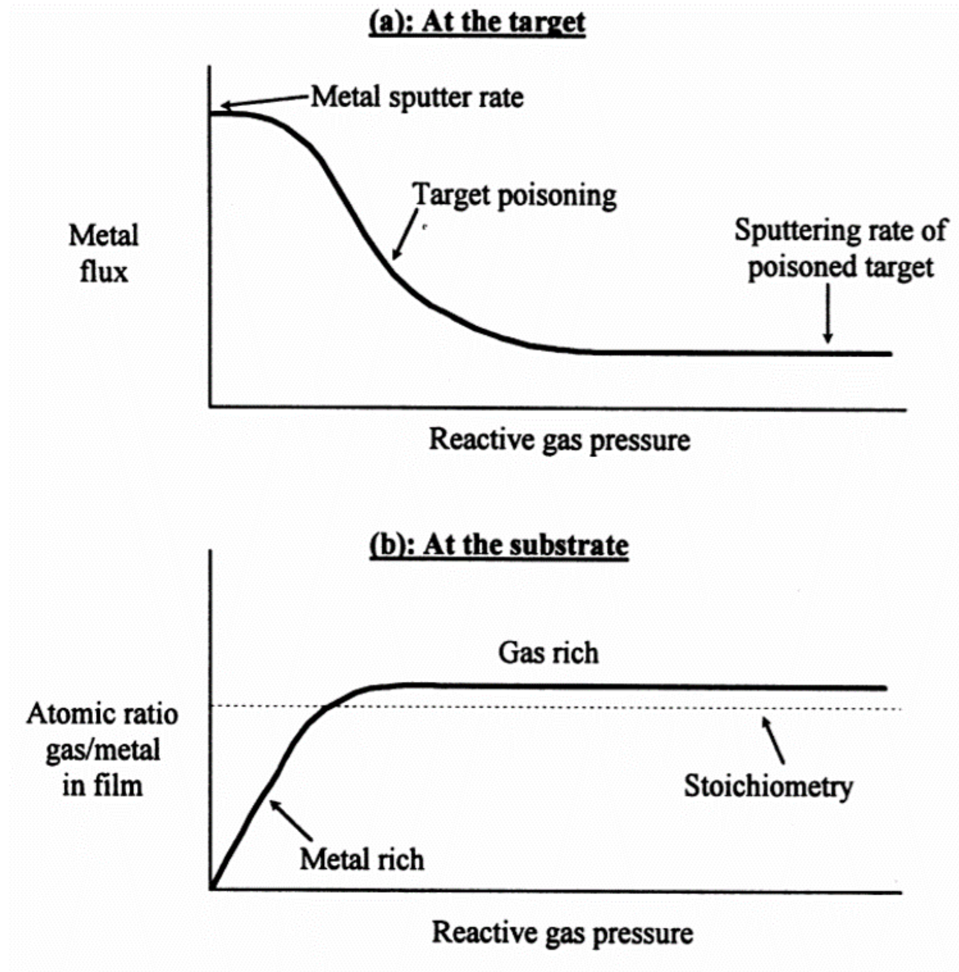

Figure 2.2: This is a conceptual diagram which demonstrates the trends for sputter yield and gas/metal ratio in a re actively sputtered film as a function of reactive gas pressure. Part a) shows the metal flux, or in other words, the sputter yield, as a function of reactive gas pressure, while part b) shows that there is a minimum reactive gas pressure which results in a film of ideal stiochiometry [1].

The graph in Figure 2.2a shows the "metal flux", meaning the amount of material ejected from the target, as a function of the reactive gas partial pressure. The sharp decline in flux indicates that an oxide is forming on the substrate surface, and the lower sputtering

rate at high reactive gas pressures is indicative of a "fully poisoned" target. In this region, the ion bombardment is ejecting an oxide from the surface of he target. The graph below, in Figure 2.2b, shows the dependence of the stoichiometry of the deposited film on the reactive gas flow. As mentioned, there must be enough reactive gas in the chamber in order to fully oxidize the film material. Otherwise, the deposited film will be more metallic than anticipated and demonstrate some absorption.

The total chamber pressure also has an effect on the deposition rate. Each ejected target atom undergoes collisions with gas atoms on its way to the substrate, losing energy to the bulk gas. These collisions will randomize the trajectory of the sputtered atoms, which expands the area of deposition and reduces the effective deposition rate. The chance that a given ejected atom will reach the substrate contributes to the deposition rate of the material, and the energy of the ejected atom, upon reaching the substrate, contributes to the film density. The total gas pressure in the chamber, along with the partial pressure of the reactive gas can be optimized for the best balance between target ablation, target oxidation, and deposition rate.

The energy of the material ejected from the target during sputtering is typically on the order of 1-10 eV, much higher than for deposition techniques such as evaporation [24]. The high energy atoms contribute to the film density, allowing for some surface mobility upon reaching the substrate, and removing voids in the film. The pressure in the chamber also contributes to the location where the metal/semiconductor-oxygen reaction occurs. An example can be used which represents the conditions used to deposit these films. For room-temperature deposition, with a total chamber pressure of around 3.5 mTorr, the total mean free path of the ejected material will be on the order of 10 millimeters. With the distance between the sputter target and the substrate being a few inches, there will likely

be on the order of 10 collisions between the ejected material and the other atoms in the chamber. Given a partial oxygen pressure of around 0.5 mTorr, the chances that more than one collision with oxygen is small. This leads to the conclusion that the majority of the reaction between the ejected material and the reactive gas will take place at the substrate surface.

Another consideration for reactive sputtering is the cathode voltage as the target oxidizes. The oxide is an insulating material which builds positive charge as the ions bombard the surface, as shown in Figure 2.3 [1]. In the metallic target case, demonstrated on the right side of the graphic, the bombarding ions will become neutralized as they interact with the electrons from the cathode. However, if an insulating material builds on the surface of the cathode, the ions hitting the insulating surface will continue to build up charge, attracting the electrons from the cathode, and resulting in a continually charging capacitor. This situation can cause arcing, which destabilizes the plasma, can damage the target, and can lead to defects in the deposited layer [1].

In order to avoid arcing and charge build-up, the DC power supply is pulsed so that periodically the polarity of the magnetron is reversed resulting in a short period of time where the surface of the target is bombarded with electrons. These electrons neutralize the positive surface charge, and discharge the capacitor in order to avoid any arcing. With a pulsed DC power supply, the frequency and pulse width of the power supply is chosen based on the target material.

Alternatively, an RF supply can be used to neutralize the charge buildup on the target. The RF supplies a sinusoidal alternating current to the magnetron, at 13.56MHz. The advantage of the RF supply is that it can be used to sputter from insulating targets.

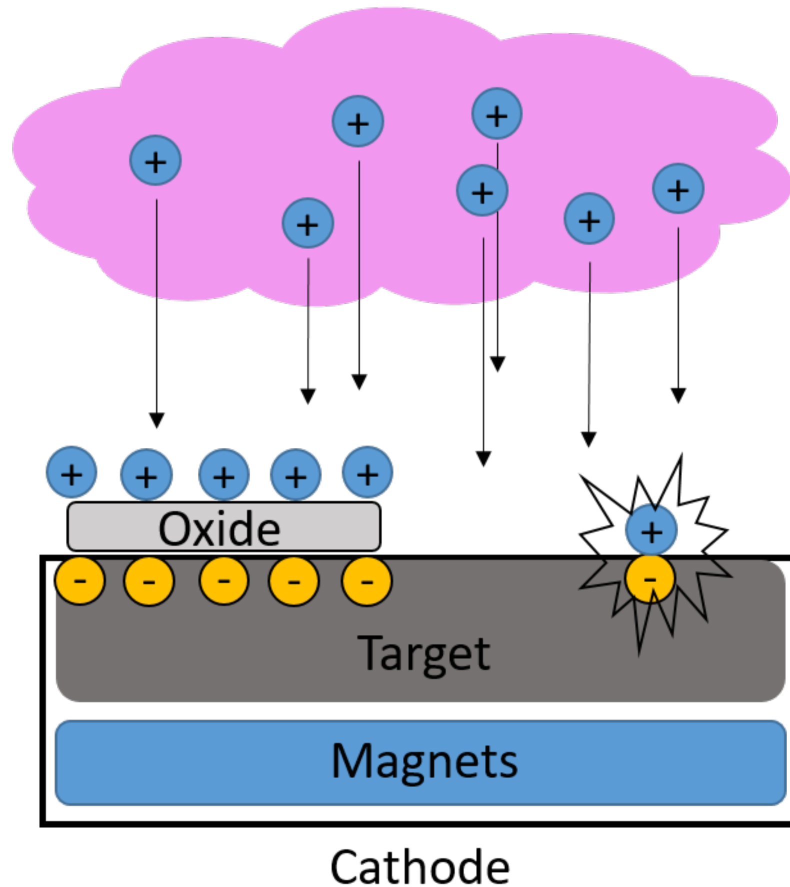

Figure 2.3: This demonstrates the build up of charge along an insulating surface layer of the cathode or target (left) and compares to the situation without the build-up of an insulating layer where electrons and ions recombine and neutralize (right).

However, the duty cycle is set to 50%. Pulsed-DC supplies allow for optimizing the duty cycle to allow for a higher deposition rate. The drawback, however, is that pulsed-DC power supplies cannot be used with insulating targets. The typical pulse frequency for these power supplies is in the 100kHz range. Many insulating materials, such as oxides, have a high impedance at these frequencies which does not allow for igniting and maintaining a plasma at voltages typically provided by a DC power supply. However at higher frequencies

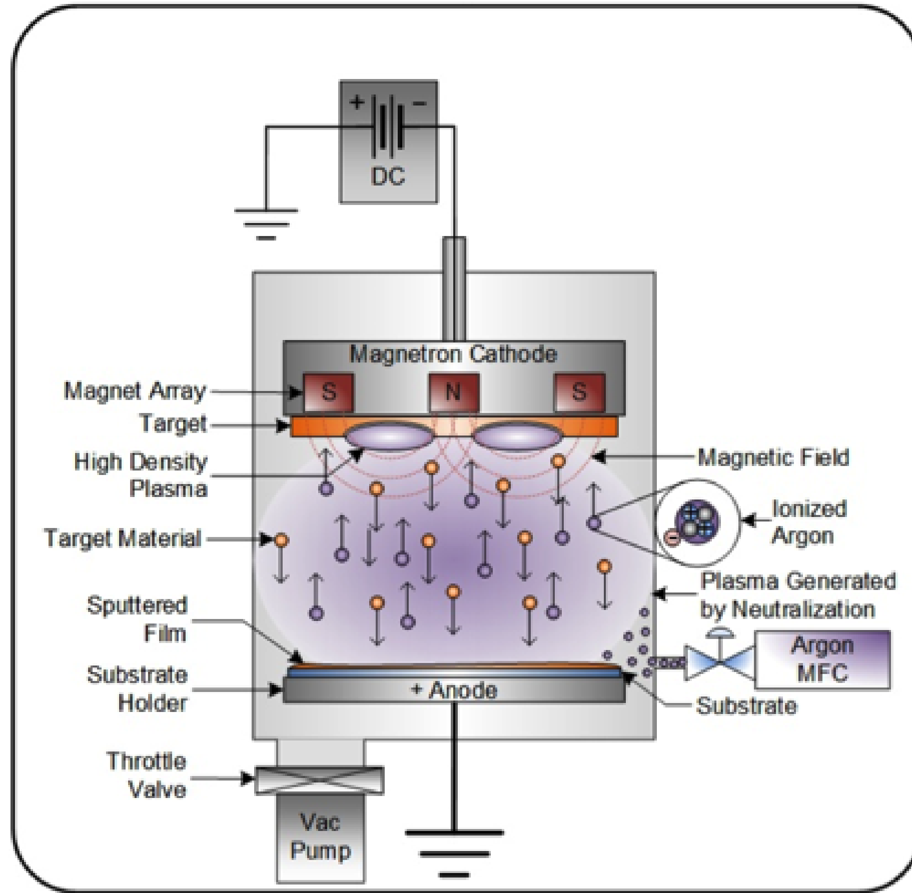

Figure 2.4: A diagram of the magnetron sputter chamber. [2]

provided by an RF power supply, the impedance reduces to allow for a plasma to form at voltages which the power supply can practically deliver [28].

With this last piece, a general overview of the theory of reactive pulsed DC magnetron sputtering has been given. All of the principles together are shown in Figure 2.4. This diagram shows each of the components detailed above. The vacuum pump at the bottom right shows how the chamber is evacuated so the gas in the chamber can be controlled, and consequently the process can be controlled in order to create the desired film. In this diagram, the argon gas is introduced at the lower right of the chamber, and the DC power

supply shown at the top of the figure is turned on to form a plasma between the magnetron cathode and the substrate anode. The magnetic field from the magnetron magnet array enables a higher density plasma at the surface of the target (shown in orange). Ionized argon atoms are accelerated toward the target, and upon collision, eject target material toward the substrate, growing a film.

2.2 Details of the Vacuum Sputter System

The vacuum sputter chamber used for this experiment was made by AJA International. It has four magnetron sputter sources, three of which are equipped with pulsed DC power supplies, and one of which is equipped with an RF power supply. This allows for the use, in this experiment, of two sputter guns simultaneously in order to grow these composite films. The two other sputter sources can be used in a variety of ways, including co-sputtering of up to four materials, and the growth of interference filters with up to four materials.

Each sputter source is slightly offset from the center of the chamber to accommodate the quantity. In the vacuum chamber the substrate is physically above the sources, leading to a “sputter up” configuration. This type of physical configuration allows for cleaner substrates. In order to accommodate for the offset of the sources from the chamber center, the substrate holder rotates. A load-lock vacuum chamber is attached to the system in order to quickly change samples without venting the main chamber.

The pulsed DC power supply used to deposit from the tantalum target for this experiment is the TruPlasma DC 4000 Series, made by Trumpf Huettinger, Inc. The maximum output voltage is 800V, with a pulse frequency of 2-100kHz, and a pause duration of 1-10us. The pulse frequency is the repetition rate of the pulse waveform, which is shown in Figure 2.5. The pause duration defines the time over which the voltage output of the

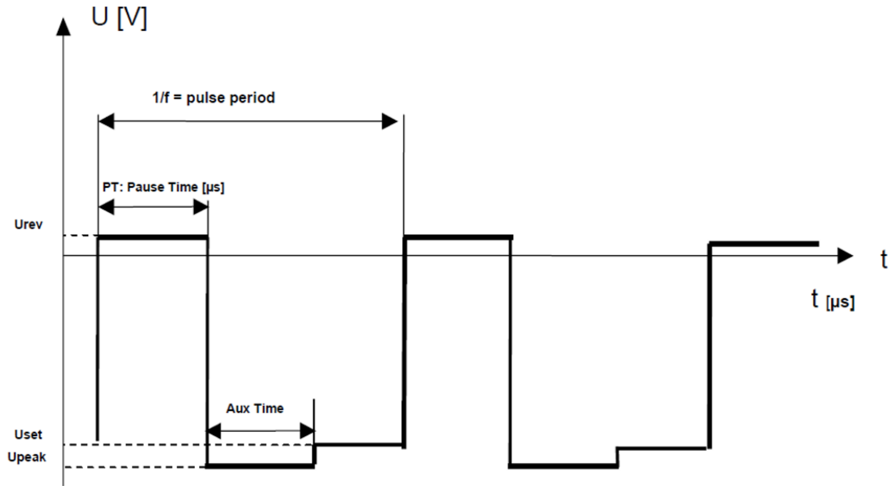

Figure 2.5: The voltage profile of the TruPlasma pulsed DC power supply [3].

power supply is positive. This change in polarity is what allows for the discharge of positive surface charge on the target, and which helps to avoid arcing and the build-up of dielectric material on the target surface, as was shown in Figure 2.3.

The voltage during the pause time (reverse voltage) is defined as -0.15 times the set voltage, and the voltage peaks at 1.15 times the set voltage when the power supply switches from reverse to forward voltage. The time period of this peak voltage, labeled in Figure 2.5 as “Aux time”, is equal to the pause time. Taken together the reverse voltage and the peak voltage will average so that the total average power is equal to the set-point power, independent of the pause duration.

The pulsed DC power supply used to deposit from the Silicon target is an ENI DC Plasma Generator (RPG-50A). This power supply was used in place of another TruPlamsa, in order to use a higher power set-point for the silicon deposition, increasing the deposition rate. The frequency for this power supply was set at a fixed 120kHz.

The magnetron sputter sources are designed and made by AJA International, as part of their Stiletto Series, which house a two inch diameter round target. Each of these sputter guns is equipped with a shutter, and shielding chimney. Gas injection can be made internal to the sputter source, which in combination with the chimney can produce a higher differential pressure on the target surface, while keeping the overall chamber pressure low [29]. The tilt of the sputter source can also be adjusted to maximize uniformity over the substrate area.

Gas flow into the chamber is controlled by an MKS G-Series Digital Mass Flow Controller, which controls the flow rate into the chamber of up to four different gases. The technique used in this system to measure gas flow is differential heating. A sensor tube is equipped with an external heater, and a small fraction of gas is flowed through the sensor tube. A temperature sensor is located both before and after the heater. The amount of energy it takes to raise the temperature of a volume of material is defined as the specific heat capacity. For this situation, the gas is known, and therefore, the difference in heat between the two temperature probes is directly related to the volume of gas that has flowed between the two temperature sensors [30]. In this manner, the gas flow can be monitored and adjusted to achieve the set point.

Once a gas is flowing into the chamber, it is critical to be able to precisely measure the chamber pressure. While there are a large variety of pressure measurement instruments, many of them use measurement techniques which rely on knowing the type of gas being measured, as they must factor into the calculation the atomic mass of the gas. This type of system is not ideal for this application, as there may be up to four different gasses flowing into the chamber at any given time, with different partial pressures. To solve

this problem, this system uses a capacitance manometer, e-Baratron by MKS, to measure chamber pressure.

Capacitance manometers have the advantage of measuring absolute pressure (force/area) which is agnostic to constituent gas atomic mass, albeit with a reduced sensitivity compared to other techniques such as ion gauge and Pirani gauge. The mechanism of measurement is a thin conductive diaphragm which is suspended between the environment (chamber with process gasses) and a high vacuum environment. On the high vacuum side of the device is a set of electrodes, which creates a capacitor between the diaphragm and the electrodes. The pressure differential between the chamber and the high vacuum sides of the diaphragm cause it to bend, changing the capacitance of the sensor.

This capacitance manonmeter can measure five decades of pressure, and is used for the pressure ranges between 5.0×10^{-4} - 5.0 Torr, which is the ideal range for the measurement and control of the process gasses. This pressure sensor interfaces with a gate valve control system, from VAT, which acts like a shutter on the vacuum pump. These systems are interfaced together in the AJA System computer control interface, allowing for independent control of gas flow and chamber pressure.

2.3 Deposition Parameters and Samples Fabricated

During the initial investigation of appropriate deposition parameters for SiO_2 and Ta_2O_5 for this chamber configuration, a number of observations were made. The first observation is that the deposition rates in this chamber are relatively low, especially for SiO_2 deposition. This lead to the use of the ENI power supply described above in order to boost this material deposition rate by enabling a higher power deposition. This observation is key to this work,

as the relative deposition rates of the two oxides effect the available combinations of Si-Ta-O films that can be made during co-sputtering.

Another early observation was the oxygen partial pressure levels for operation in the transition mode between the metallic deposition and the "target poisoning" mode were different between the two materials. Namely, the oxygen needed to fully oxidize the silicon target was lower than what was needed to oxidize the tantalum target. This observation was important because it would inform how the experimental setup was determined. The end result would be the need to use more oxygen to co-sputter the films than would be ideal if only re-actively co-sputtering from a silicon target.

It was determined that an optimal experiment would result if a series of films were fabricated in which only one deposition parameter was varied. Since the goal was to have a series of films with varying Si-Ta-O composition, that one parameter needed to be either the Si target power of the Ta target power. As mentioned above, it was found that the deposition rate of the SiO_2 was lower than the deposition rate of the Ta_2O_5, leading to the practical choice to vary the Ta target power.

The Ta power supply pulse frequency was set to 100kHz, the maximum rate for the power supply, and the pause duration was set to 4us. The power supply for the Si target was set at 120kHz with unknown pause duration.

It is generally understood that the options for thin film deposition include control of the power supply by adjusting a power set-point (W), voltage setpoint (V) or a current set-point (mA). For this study, all of the power supplies were operated in the "Power Mode", with the specified target value being the wattage. With plasma ignition for the Ta target

occurring just under 30W power, the lowest power setting for co-sputtering with this target was limited to 30W.

The upper limit of the Ta target power was also a practical choice, and was limited to 95W. Since the tantalum needs more oxygen than the silicon in order to fully oxidize the film, increasing the highest tantalum power will increase the overall oxygen needed in the chamber at the highest power condition for the two targets. Since this study does not simultaneously vary the Ta target power and the oxygen flow, any additional oxygen needed in order to fully oxidize the co-sputtered films will further poison the Si target. Some balance point must be chosen.

The power level for the Si target was chosen by the highest operational power achieved for which there was stable deposition conditions. These stable deposition conditions were determined by two methods: a voltage which did no change over the course of minutes, indicating that there was no charge build-up or heating at the target surface, and that there was no observable arching in the plasma.

A list of the resultant power levels chosen for the study is shown in Table 2.1. For the series, co-sputtering occurs for five out of the seven samples. The other two samples are pure SiO_2 and pure Ta_2O_5.

Each series of seven depositions were deposited onto two sets of 2" diameter substrates: single-crystal Silicon and Gallium Arsenide (GaAs). Images of all of the samples can be found in Figure 2.6. Notice that all of the samples are similar color, indicating that all samples have a similar optical thickness, defined as the product of the refractive index and the physical thickness. The optical thickness is directly related to the phase change of the

Table 2.1: The deposition parameter set-points utilized in this study.

SiO_2 Target Power (W)	Ta_2O_5 Target Power (W)
0	95
200	95
200	80
200	65
200	50
200	30
200	0

light as it passes through the material, therefore maintaining a constant optical thickness will produce the same interference effects between the samples.

Due to the geometry of the chamber, only one 2-inch diameter sample was grown during each deposition. The in-situ ellipsometer had a fixed angle. While the deposition chamber had the capability to vary the working distance by moving the sample up and down in relation to the targets, there is only one substrate position in which the ellipsometer can be used during growth. Since there was interest in having this in-situ data, the working distance was fixed. It was observed for depositions done at this substrate height, the area of high film uniformity was around 3 inches in diameter. This meant that for 2" diameter samples, each deposition was repeated once for the silicon substrate and once for the gallium arsenide substrate, giving a total of 14 depositions. The measured run-to-run variation in composition was less than 3%, leading to a high confidence that the deposited films were near-identical.

The base pressure in the chamber was between 4-6$\times10^{-8}$ Torr. The substrate rotation speed was consistently between 6-8 RPM during the depositions.

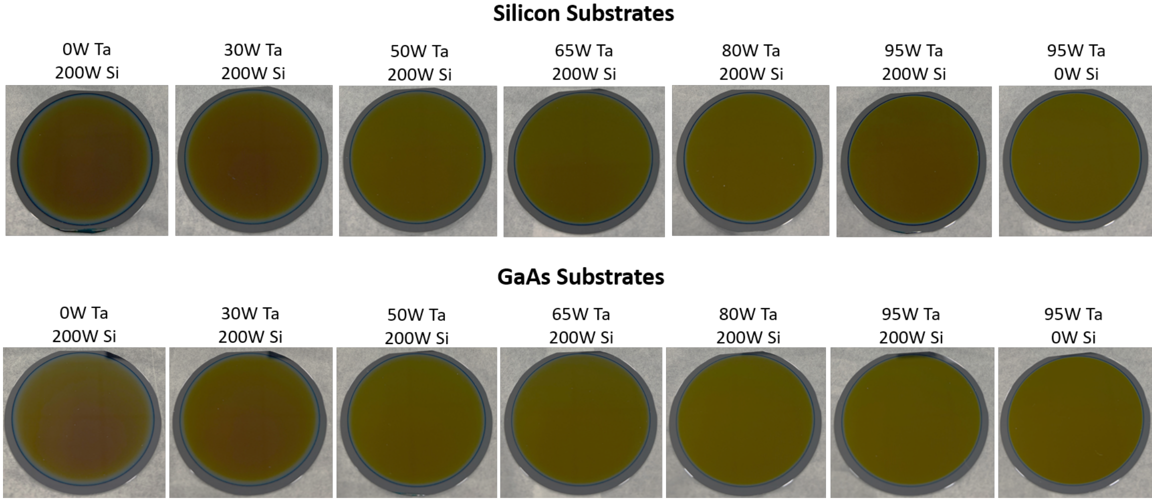

Figure 2.6: Images of each of the samples made for this work.

The method in which the chamber total and partial pressure was adjusted was the following. First, the Ar flow rate was set to 30 sccm. Then the VAT gate valve control system was set to a location where the total pressure in the chamber was 3.0 ± 0.1 mTorr, and held there for the remainder of the deposition. This held the Ar partial pressure at 3.0 ± 0.1 mTorr. The oxygen flow rate needed in order to fully react the target material when co-sputtering at the highest powers for both sources was 5.6 sccm. This value was initially determined by watching the voltage of the two targets during co-sputtering at the highest powers and determining the value of oxygen flow which allowed for stable voltage. The flow rate was then confirmed by performing a co-deposition at full powers using this flow rate, and verifying that the resultant film was indeed visibly transparent, meaning that the Si and Ta were fully oxidized during deposition. The resultant total pressure during deposition was 3.4 ± 0.1 mTorr. Due to the way in which the gas was handled, it can be concluded the oxygen partial pressure in the chamber during deposition was 0.4 ± 0.1 mTorr.

Table 2.2: The deposition conditions under which the samples for this study were grown.

Parameter	Value
Chamber Base Pressure	$5.0 \pm 1.0 \times 10^{-8}$ Torr
Substrate Rotation	7 ± 1 RPM
Ar Flow Rate	30 sccm
Ar Partial Pressure	3.0 ± 0.1 mTorr
O_2 Flow Rate	5.6 sccm
O_2 Partial Pressure	0.4 ± 0.1 mTorr
Total Chamber Pressure	3.4 ± 0.1 mTorr
Ta target Pulse Frequency	100 kHz
Si target Pulse Frequency	120 kHz
Film Optical Thickness	goal of 330 nm
SiO_2 Deposition Rate	1.6 ± 0.05 nm/min
Ta_2O_5 Deposition Rate	3.65 ± 0.05 nm/min

Each film was grown to have the same optical thickness, which is defined as the product of the refractive index and physical thickness. The stress measurement method necessitates the reflection of a laser array off the sample surface. For thin films applied to substrates with a higher refractive index, an optical thickness of half of the laser wavelength would maximize the reflection off the sample into the detector, resulting in the best quality data for the film stress measurements. At the time of the depositions, the expected laser source for investigation was a laser diode at 660nm, leading to an optical thickness for all samples of 330nm. As detailed in the following chapter, an in-situ ellipsometer was used in order to model the index in real time and determine the target physical thickness.

The information about the deposition conditions described above can also be found in Table 2.2, along with the deposition rates for the pure SiO_2 and pure Ta_2O_5.

CHAPTER III

OPTICAL CHARACTERIZATION OF THE CO-SPUTTERED THIN FILMS

In order to monitor the film fabrication, and verify that the films have optical properties consistent with published results, each of the films were characterized using ellipsometry in order to identify physical thickness and optical dispersion. In addition to these properties, ellipsometry can also give an estimate of the physical composition of the films, using an effective medium model. In this chapter, the theory behind this measurement technique is described, along with the results of these measurements and modeling of the films. The results of these measurements are used to understand the film composition, and to quantify the similarity of the sets of films grown on the two substrate materials.

3.1 Theory of Spectroscopic Ellipsometry

Ellipsometry is a useful tool in the determination of the optical properties of thin films. This method measures the change in polarization state of light due to the interference between the reflection off the thin film surface and the reflection off the substrate surface, as shown in Figure 3.1. Each of the two reflected beams shown in this figure interfere together. This encodes information about the phase difference of the two waves (a result of the optical path length difference), as well as the relative magnitude of the two reflections (a result of the refractive indices and absorption of each material). This information is most easily accessed by analyzing the difference between the incident polarization state and the polarization state of the reflected light. Ellipsometry is the measurement of the polarization state of this combined reflection. This measurement can determine the index of refraction of the film (n) and the extinction coefficient (k) of the film material over the measured spectral range, along with the thickness of the film [31, 32, 33].

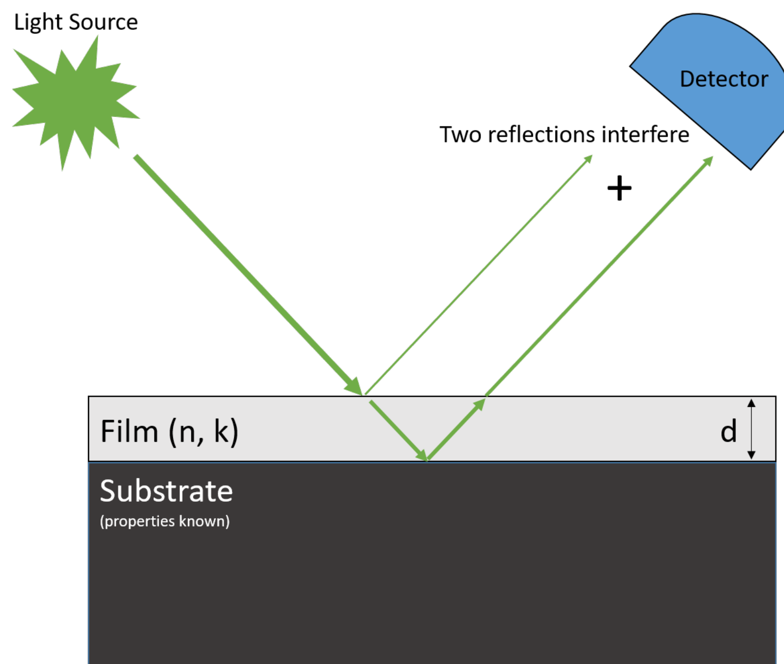

Figure 3.1: A diagram of the reflections from the two interfaces present in a transparent thin film scenario.

3.1.1 Measurement of Ellispometric Parameters

The polarization state of light is defined as the direction of oscillation of the electric field component of the electro-magnetic wave. This polarization state cannot be measured directly, as the frequency of oscillation of the waves are much too fast to measure with known detector systems. Instead, the polarization state can be determined indirectly by measuring the intensity change from a rotating polarizer and wave-plate. Four measurements are needed in order to fully define the polarization state, and the values obtained from these measurements are called the Stokes Parameters [34].

The Stokes Parameters, or sometimes called the polarization observables, represent: (1) the total intensity, (2) the amount of light that is horizontally/vertically polarized, (3) the

amount of light that is polarized at $\pm 45^\circ$, and (4) the amount of light that is right or left-handed circularly polarized. Together, these parameters describe the polarization state of light. From these parameters, a degree of polarization (DOP) can also be defined, which defines the extent to which the light can be described by a single polarization state. For instance, a DOP of unity means that the light is highly polarized, where a DOP of zero means that the light is completely un-polarized.

Any polarization state can be described as a superposition of two vectors, each with an amplitude, and with a relative phase between them. For ellipsometry measurements, the reference vectors are the s and p-polarization states, which are defined by the plane of incidence of the light. The plane of incidence is determined by taking two rays of light, the incident ray and the reflected ray, and forming a plane from these two rays. The p-polarization state is the electric field oscillation direction parallel to the plane of incidence. The s-polarization state is the electric field oscillation direction perpendicular to the plane of incidence.

The s and p-polarization components of light interact with material interfaces in different ways. The direction of oscillation of the electric field determines its interaction at a material boundary, due to the continuity conditions imposed by Maxwell's equations. There are three conditions that determine the interaction of an electro-magnetic wave at a dielectric interface: the magnetic field component perpendicular to the interface is continuous across the interface, the electric field component parallel to the interface is continuous across the interface, and the phase of the electro-magnetic waves is continuous across the interface.

These three conditions lead to the determination of the reflection and transmission coefficients of the s and p-polarization components at an interface, which are described as

$$
\begin{aligned}
r_p &\equiv \frac{E_{rp}}{E_{ip}} = \frac{n_t \cos\theta_i - n_i \cos\theta_t}{n_t \cos\theta_i + n_i \cos\theta_t}, \\
r_s &\equiv \frac{E_{rs}}{E_{is}} = \frac{n_i \cos\theta_i - n_t \cos\theta_t}{n_i \cos\theta_i + n_t \cos\theta_t}, \\
t_p &\equiv \frac{E_{tp}}{E_{ip}} = \frac{2n_i \cos\theta_i}{n_t \cos\theta_i + n_i \cos\theta_t}, \\
t_s &\equiv \frac{E_{ts}}{E_{is}} = \frac{2n_i \cos\theta_i}{n_i \cos\theta_i + n_t \cos\theta_t},
\end{aligned}
\tag{3.1}
$$

where $r_{p,s}$ is the reflection of the p or s-polarized light $t_{p,s}$ is the transmission of the p or s-polarized light, $E_{rp,rs,tp,ts,ip,is}$ is the electric field where r is for reflected, t is for transmitted, i is for incident, and s, p is for s or p-polarization, $n_{i,t}$ is the refractive index of the incident and transmitted medium respectively, and $\theta_{i,t}$ is the incident angle of the incident or transmitted ray respectively [4].

For light that is transmitted, it is important to also define a phase thickness of the transmission. This takes into account the optical thickness of the material, the angle of transmission which impacts the path length travelled by the light beam, and the phase accumulated by the wave traveling that distance. This phase thickness can be described as

$$
\beta = 2\pi \left(\frac{d_1}{\lambda} \right) n_1 \cos\theta_1, \tag{3.2}
$$

where d_1 is the physical thickness of the layer in question, n_1 is the refractive index of the layer in question, and θ_1 is the angle of the ray propagating through the layer with respect to the surface normal.

If there is a circumstance where a thin layer of transparent material is deposited on a reflective surface, then some of the light will be transmitted and reflected at the air-film interface, and some of the light will interact with the substrate-film interface. This scenario is shown in Figure 3.2 with the notation of Eqn. 3.1, and Eqn. 3.2 [4]. This

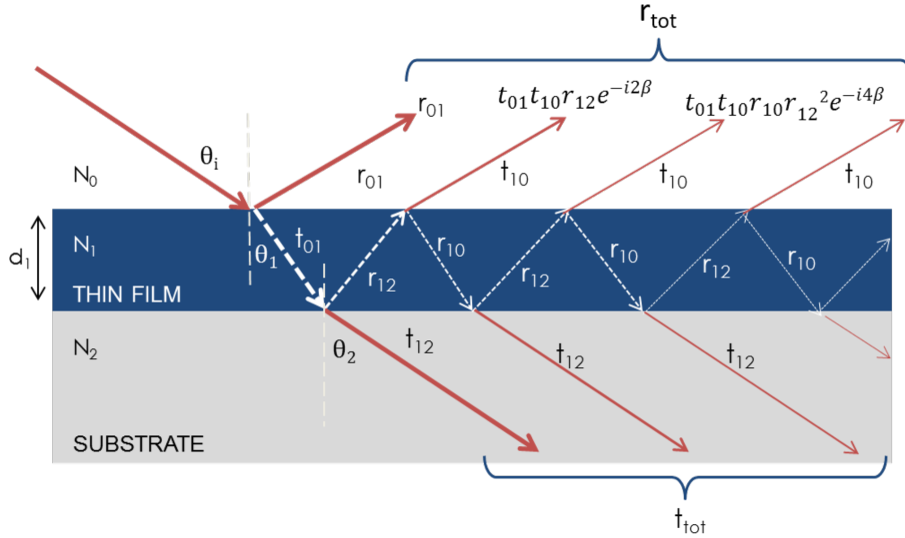

Figure 3.2: A diagram of the determination of the total reflection and total transmission of a beam at oblique incidence on a substrate with a thin film [4].

figure shows the scenario of a transparent thin film on a substrate. Multiple reflections from each interface contribute to an overall transmission, indicated at the bottom, and an overall reflection, indicated at the top. Each interaction with an interface has an associated reflection coefficient, each transmission through the bulk film has an associated transmission and phase accumulation. The resultant total reflection is the superposition of each of the reflected waves.

Ellipsometry measures the ratio between the component of reflected light which is p-polarized, and the component of the reflected light that is s-polarized, and the relative phase between them. Each of the waves describing the reflected light is a complex value, as it has some components that have accumulated phase by traveling through the thin film. The ratio of these two complex reflections can be described as an ellipse with amplitude and phase, and the classic ellipsometry values associated with that ellipse are Ψ and Δ as

described in Eqn. 3.3 [4].

$$\rho \equiv \frac{\tilde{r}_p}{\tilde{r}_s} = \tan \Psi \mathrm{e}^{\mathrm{i}\Delta} \tag{3.3}$$

From this definition of the polarization ellipse, one of the distinct measurement advantages is that the state is self-referencing so is not affected by fluctuating or low light levels, or by diffuse scattering.

One note of importance is that the equations above, determining the reflection and transmission of the light at each interface are written as if the incident light is a single wavelength. In spectroscopic ellipsometry, a large range of incident wavelengths are scanned such that wavelength-dependent nature of the optical constants can be determined.

The basic components of the ellipsometer are a broadband light source, a polarizer, and a compensator on the source side. The polarization state of the light emitted from this instrument is wavelength-calibrated and well-defined. This light is then reflected from the sample. The detector side contains an analyzer and a CCD spectrometer which is also wavelength-calibrated. Based on the ratio of the reflected light that is p-polarized and s-polarized, the ellipsometry parameters Ψ and Δ are reported.

While the ellipsometry parameters are informative quantities, the useful information from these measurements is a determination of the refractive index and the thickness of the film. This presents an inverse problem. Here the result is measured, as opposed to the cause, and in order to identify the material properties of the sample (the cause), an "educated guess" must be made and a model formed to calculate the anticipated optical constants and thickness of the film.

For most samples, the equations to convert the measured Ψ and Δ values into the refractive index, n, and the absorption coefficient, k, are transcendental, meaning that

a model must be built and its parameters adjusted in order to fit the data. Typically, a regression analysis is used in order to fit the data, where the values of Ψ and Δ are calculated for a given model and compared to the measured data to understand how "good" the model is. A mean-squared error (MSE) is used to quantify the difference between the experimental and model-generated data, where the smaller MSE implies a better fit.

3.1.2 Kramers-Kronig Relations

Since a variety of models have the capability to describe the same collected data, the general rule of analysis is to find the simplest optical model that fits the experimental data, and to verify the uniqueness of the model. The simplest unique model that fits the data is assumed to be the model that best describes the physical film.

Another constraint on the model of the optical properties is the Kramers-Kronig relations. This states that the refractive index and the absorption coefficients of a material are not independent parameters, and describes the physical relationship between the two as a function of wavelength [35].

Conceptually, the interaction between light and matter can be thought of as a damped-driven harmonic oscillator. The electric field of the light waves are the driving force, the atoms in the material are the harmonic oscillators, and the damping is due to the inter-atomic forces in the material. As is well-described in a physical model, the damped-driven harmonic oscillator has a resonant frequency which is dependent on the material properties of the oscillator. In the light-matter interaction model, this can be interpreted as an absorption resonance. The energy from the incoming electric field is absorbed, giving the oscillator atoms the needed energy to have a heightened oscillation amplitude, characteristic of the resonance response.

Along with a resonant absorption, the oscillator model describes the time lag between the driving frequency and the oscillator response. This characteristic lag changes the way that the energy, carried by the electric field, propagates through the material. The greater the response time, the longer the energy takes to be carried from one side of the material to the other. This concept is called the electric susceptibility of the material, and is directly related to its refractive index.

From the oscillator model, it can be calculated that there is a change in phase (from positive to negative) between the driving frequency and the response frequency which is centered around the resonant frequency. This change is due to the fact that the oscillation amplitude has dramatically increased. Since the atoms in the material are moving larger distances, the response time is longer.

This concept translates to the light-matter interaction model. In spectral regions without absorption, the refractive index will increase with decreasing wavelength. This is known as "normal dispersion". Since the refractive index is like the phase delay and the absorption is like the resonant frequency, the relation between the two is such that there can only be a change in the direction of the index of refraction where there is an absorbing region. This absorbing region, resulting in the refractive index decreasing with decreasing wavelength is called "anomalous dispersion". A diagram showing the relationship between the anomalous dispersion and absorption is shown in Figure 3.3, where there are three absorption peaks which correspond to three anomalous dispersion regions. This causal relationship between absorption peaks and anomalous dispersion limits the models for the optical constants so that the models have a physical interpretation.

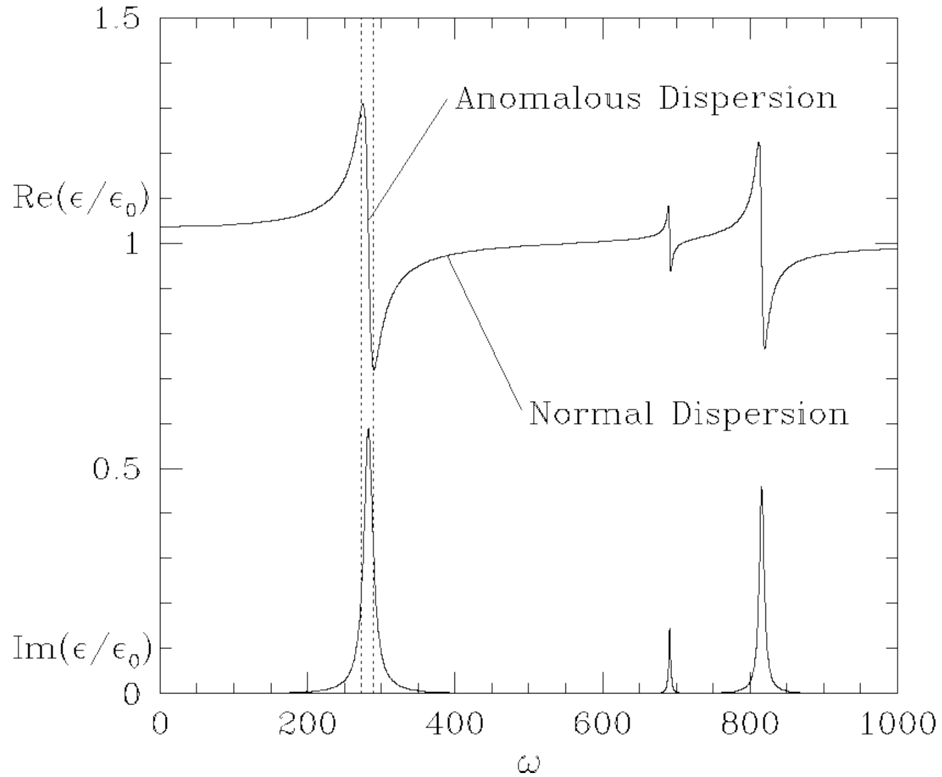

Figure 3.3: An example of anomalous dispersion of a material with three absorption resonances. The real part shown here is the index of refraction, while the imaginary part is the absorption coefficient. These are both shown as a function of frequency [5].

3.1.3 Optical Dispersion Analysis Techniques

Ellipsometric measurements result in two measured quantities (Ψ and Δ) for each wavelength. Therefore, two pieces of information can be calculated from this data for each wavelength. However, it is often necessary to know n, k, and thickness for the film. In order to determine all three pieces of information, the transparent spectral region must be used. If a film (or a spectral region of the film) is loss-less, then the extinction coefficient (k) is equal to zero. Given this information, the two measured quantities (Ψ and Δ) can be used to determine the other two values of interest: n and thickness. The index (n) will be a function of wavelength, but the thickness will be constant over all wavelengths.

One common model that is used to describe transparent films is the Cauchy model, which is an empirical description of the index dispersion of transparent materials. The key to this model is that it is valid only for regions where the extinction coefficient is zero. The Cauchy model describes the dispersion relation as,

$$n(\lambda) = A + \frac{B}{\lambda^2} + \frac{C}{\lambda^4}, \tag{3.4}$$

where A, B and C are the fit parameters. The transparent region gives the opportunity to model the material with a simple Cauchy model in order to find both the index in the transparent region, as well as the thickness of the film. This information, together with the use of other models for the absorbing region, can allow for the determination of n, k and thickness for the film over the full spectral range. It is common to model the optical dispesrion of SiO_2 films using a Cauchy function.

The other film of interest however, Ta_2O_5, has some small absorption in the UV spectral range. The Cauchy model cannot accurately model these absorbing regions. Instead, a model such as the Tauc-Lorentz Oscillator model can be used in order to model the UV absorption region.

An oscillator model uses the concepts described in Section 3.1.2 to model the material response to the incident electric field as an oscillator. There are a variety of oscillator models, such as Drude, Gaussian, and Lorentz, which describe the shape of the material response (dipole oscillations and dielectric polarization) as a function of incident photon energy.

The Lorentz oscillator is the oscillator model that describes a classical harmonic oscillator, which relates the dielectric constants (ϵ_1 and ϵ_2) to the incident photon energy. The

complex dielectric function is related to the optical constants as

$$\begin{aligned}\tilde{\epsilon} &= \epsilon_1 - i\epsilon_2,\\ \epsilon_1 &= n^2 + k^2,\\ \epsilon_2 &= 2nk.\end{aligned} \tag{3.5}$$

The Lorentz oscillator model describes the shape of the absorption peak as a Lorentz function with the form

$$\epsilon_2(E) = \frac{A\Gamma E_0 E}{(E_0^2 - E^2)^2 + \Gamma^2 E^2}, \tag{3.6}$$

where A is the peak amplitude, Γ is the full-width half-max peak width, and E_0^2 is the peak center energy [36].

While this oscillator model is useful for modeling the absorption behavior of metals, the dielectric nature of SiO_2 and Ta_2O_5 necessitate a different handling of the absorption near the bandgap of the material. The dielectric nature of the two materials means that the bandgap energy is high, putting it in the UV region. While the peak of the absorption might not be measured, the response of the material to incident light with energies slightly lower than the bandgap energies will not have the same response as those above the bandgap energy. As the majority of the measured spectra will be in the range of energies starting at slightly below the bandgap energy, a model must be used which takes into account the bandgap of the materials.

The Tauc-Lorentz oscillator model uses a modified Lorentz oscillator which includes a bandgap energy such that there is no absorption at energies below the bandgap. This model is commonly used for dielectrics with UV absorption, and accounts for both the transparent and the absorbing regions. Near the band edge of the material, the absorption is modified

by the term

$$\epsilon_2(E) \propto \frac{(E - E_g)^2}{E^2} \tag{3.7}$$

so that it reaches an absorption of zero at the bandgap energy (E_g) [36].

With this modification term, the imaginary part of the dielectric function for the Tauc-Lorentz model becomes [36]

$$\epsilon_{2TL}(E) = \left\{ \begin{array}{cc} \dfrac{AE_0\Gamma(E - E_g)^2}{(E_0^2 - E^2)^2 + \Gamma^2 E^2}\dfrac{1}{E}, & E > E_g \\ 0, & E \leq E_g \end{array} \right\}. \tag{3.8}$$

The bandgap energy is used as the fourth fit parameter for this modified Lorentz oscillator model. The dielectric constant, ϵ_1, is calculated from the Kramers-Kronig relations using the absorption shape determined in the Tauc-Lorentz oscillator model. From these two functions, the optical constants can be calculated using Eqn. 3.5 for each measurement wavelength.

In order to compare the shape of the two absorption functions, Eqn. 3.6 and 3.8 have been plotted on the same graph using the parameters, $A_{(Lorentz)}$=3.15, $A_{(TaucLorentz)}$=100, Γ=0.5, E_0=3 eV, and E_g= 2.5 eV, as shown in Figure 3.4. This represents an absorption peak that is close to the material bandgap. The Tauc modification to the Lorentz function makes the absorption peak asymmetric, but accounts for the decrease in absorption due to the presence of the material bandgap.

The material Ta_2O_5 can be accurately modelled into the UV region by using two Tauc-Lorentz oscillators placed in the UV spectral region. These together model the shape of the absorption in that region, and allow for a good fit across the entire measurement spectral range.

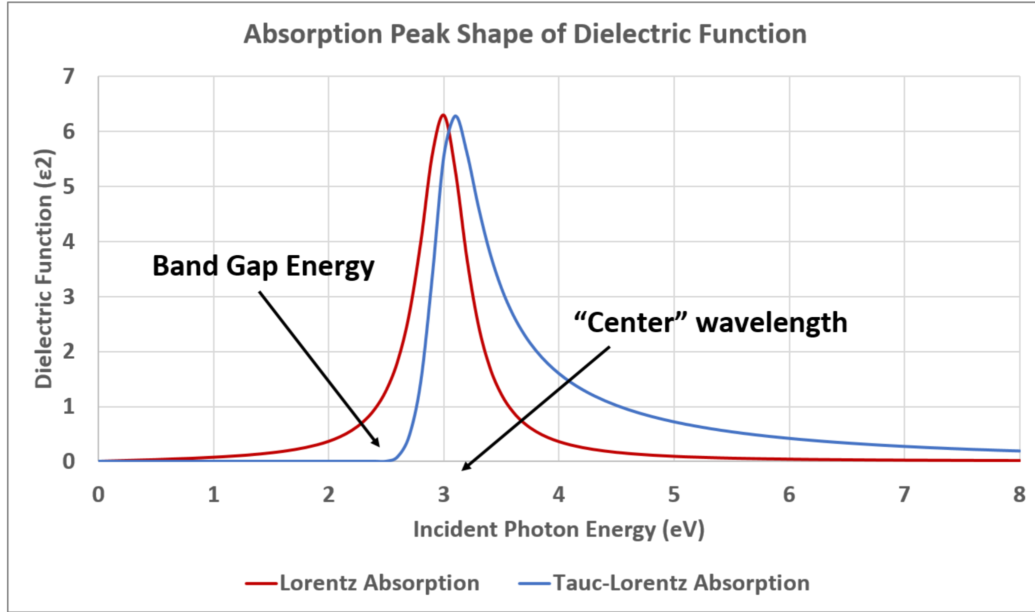

Figure 3.4: Plots of a Lorentz absorption peak and a Tauc-modified Lorentz absorption peak. Center wavelength and bandgap are indicated and are the same for both cases.

3.2 Effective Medium Theory

The purpose of this study is to determine the optical and thermo-mechanical properties of a composite SiO_2-Ta_2O_5 materials, and investigate the change in these properties as a function of material composition. Once the films are deposited onto their substrates, the composition of the film can be estimated from their optical properties using ellipsometry.

An assumption is being made here that the films are indeed composites, and that there is little to no Si-Ta bonds forming in the film. A brief literature review was conducted to investigate the likelihood of this interaction taking place during the deposition process. Based on the information from [37, 38, 39, 40], it appears that the formation of Si-Ta bonds occurs at temperatures above 600°C. Since the substrate was not heated during deposition, it is unlikely that the substrate surface temperature reached this threshold,

and therefore unlikely that these bonds were formed. Additionally, since both elemental Si and Ta have non-negligible extinction coefficients in the visible and NIR spectral regions, it would be expected that Si-Ta bonds would affect both the refractive index and the extinction coefficient of the films. As will be discussed, the optical dispersion fits did not indicate the presence of absorption in the measured spectral range. Based on this information, it is deemed reasonable to use the effective medium approximation for films which are composite SiO_2-Ta_2O_5, and assume that Si-Ta bonds are not present.

Bulk film composition is approximated using the effective medium theory for heterogeneous materials. This theory states that the dielectric permitivity of a composite material can be expressed in terms of a weighted average of the dielectric permittivities of its constituent materials [20, 41, 42].

The effective medium approximation, as described in 1935 by Bruggeman, breaks down the composite material into unit cells which contain a sphere of material "A", encompassed in a host material "B". This model requires the size of the spheres to be below the resolution limit of the optical waves, which is in fact the case for an aggregate material such as a co-sputtered oxide. Thus, in order to determine the effect of the aggregate material, one must find the effective permittivity of each unit cell, a sphere of material "A" in host material "B", and a sphere of material "B" in host material "A" and find the total permittivity by weighing each unit cell by its probability of occurrence.

In order to find the permittivity of a unit cell that includes a sphere of material "A" encompassed in a host material "B", first it must be understood that the sphere of material "A" can be treated as a dipole, which will react to an external electric field, such as incident light. The external electric field applied to the unit cell will cause a charge build-up along

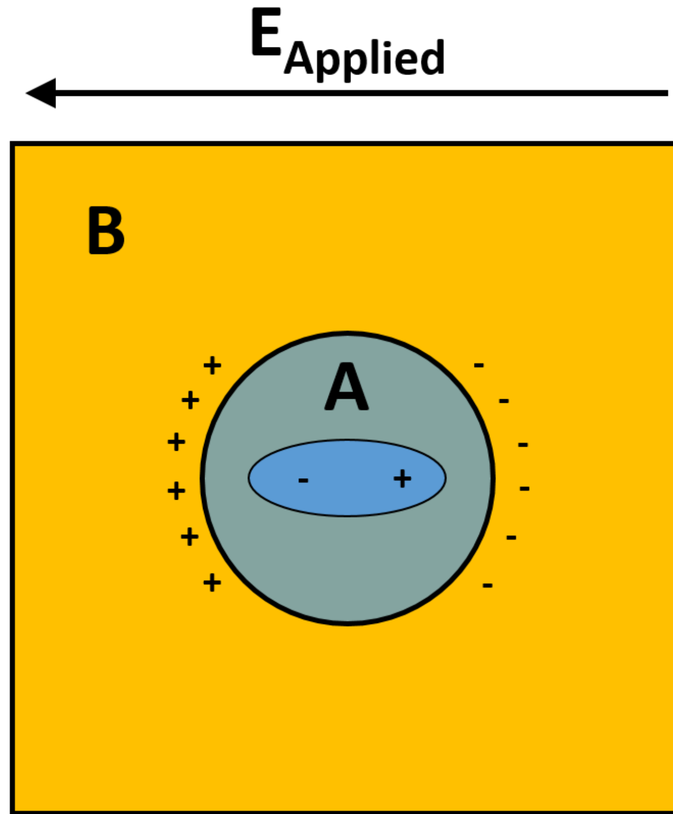

Figure 3.5: A diagram of a unit cell with material "A" in host material "B", and resulting change in local field due to applied field.

the boundaries of the sphere, as the dipole moment aligns with the electric field, as shown in Figure 3.5. This creates a local electric field around material "A".

Using this concept, the change in electric flux through the unit cell, due to the presence of the sphere of material "A" can be shown to be

$$\Delta\Phi_A = 2\pi r^2 \epsilon E_{Applied} \left(\frac{\epsilon_A - \epsilon}{\epsilon_A + 2\epsilon} \right), \tag{3.9}$$

where r is the radius of the sphere, ϵ is the permittivity of the unit cell, $E_{Applied}$ is the applied electric field, and ϵ_A is the permittivity of the material "A" [42]. A similar statement can be made for the unit cell where the sphere is material "B" in a host of material "A".

Bruggeman's effective medium theory states that the total change in flux of the composite material, which includes both types of unit cells, is equal to zero. This can be otherwise stated as

$$\begin{gathered}\eta_A \Delta\Phi_A + \eta_B \Delta\Phi_B = 0, \text{or} \\ \eta_A \left(\frac{\epsilon_A - \epsilon}{\epsilon_A + 2\epsilon} \right) + \eta_B \left(\frac{\epsilon_B - \epsilon}{\epsilon_B + 2\epsilon} \right) = 0 \\ \epsilon = \eta_A \epsilon_A + \eta_B \epsilon_B,\end{gathered} \tag{3.10}$$

where η_A is the volume fraction of material "A", and η_B is the volume fraction of material "B" such that $\eta_A + \eta_B = 1$ [42]. Using this theory, if the permittivity of the two constituent materials is known, and the permittivity of the composite material is measured, the volume fraction of the two materials can be calculated.

The key conclusion from Bruggeman's model is the material permitivities combine linearly with composition (but not linearly with refractive index). The insight can be gleaned from this statement comes from the relationship between the permitivity, the dielectric constant and the refractive index of a material, as shown in Eqn. 3.11 for non-magnetic materials, where κ is the dielectric constant and ϵ_0 is the permitivity of free-space.

$$n = \sqrt{\kappa} = \sqrt{\frac{\epsilon}{\epsilon_0}} \tag{3.11}$$

A linear relationship in permitivity leads to a linear relationship in the dielectric constant. However, the relationship between the composition and the index is non-linear. Bruggeman's model shows a composite material can be described by the volume-fraction weighted average of the dielectric constants, and the index of refraction therefore, does not vary linearly with composition.

3.3 Modeled Optical Properties of Fabricated Films

In practice, the theory described in Sections 3.1.1-3.2 are incorporated directly into the instrument and software used to do ellispometric measurements. For the measurements of these films during fabrication, an in-situ J.A. Woollam M-2000 was used.

This in-situ measurement capability allowed for the calculation of refractive index of the co-sputtered films during growth, and allowed for a target physical thickness to be set in real-time based on the calculated index, resulting in the achievement of a series of films which are close to a target optical thickness of 330nm. With the in-situ ellipsometry, the determination of the physical thickness and the index could be determined and targeted during a single growth.

It was found during the analysis of the in-situ ellipsometric measurements that the model being used for the SiO_2 films showed a refractive index much less than the literature values. This affected not only the fits for the SiO_2 films but also the estimates of the co-sputtered film compositions using the Bruggeman effective medium approximation. Due to this finding, ex-situ variable-angle spectroscopic ellipsometry (VASE) was completed using an α-SE instrument from J.A. Woollam. This instrument has a smaller spectral measurement range (380-890nm), but allows for simultaneous fitting of data collected by reflection from three different incident angles: $65°, 70°$, and $80°$. This type of fitting increases the precision of the fits, and decreases the correlation between film thickness and refractive index.

In the spectral range of the α-SE instrument, good fits can be made with a Cauchy model for the Ta_2O_5 material, as the imaginary part of the refractive index, k is zero in this range. For the following fits done for this study, the α-SE data will be presented.

The modeling of these layers incorporates a multi-layered structure, taking into account not only the properties of the substrate and the deposited layer, but also the native oxide layer on the substrate and any surface roughness present in the film. The properties of the substrates and their native oxides have been measured and modelled by J.A. Woollam, and their models were used in the fitting of the film dispersion curves.

The roughness in the films are modeled by J.A. Woollam by approximating a thin layer at the surface of the film whose index properties are an effective medium with composition 50% film material and 50% air.

The calculated dispersion curves for all 14 samples are shown in Figure 3.6. The SiO_2 dispersion is modelled well by the data reported in Palik's 1985 Handbook of Optical Constants of Solids [43]. The Ta_2O_5 is modeled with a Cauchy dispersion curve in this wavelength region, which has an index value in the expected range for this material. All of the co-sputtered films are then modelled using an EMA mixture of these two dispersion models.

One item to note is that the modelled dispersion curve for the Ta_2O_5 films on different substrates is slightly different. However, as will be described, the EMA mixing models predict very similar compositions between the sets of films on Si and GaAs substrates. Another observation is that the dispersion curves of SiO_2 and Ta_2O_5 have different shapes, in the lower-wavelength region. While both curves are relatively flat in the NIR spectral region, both have increasing index with decreasing wavelength, showing normal dispersion. If the spectral range of these fits were extended farther into the UV, the shape of the curves would not be adequately described by the same function, leading to the use of the Tauc-Lorentz model of dispersion to characterize the Ta_2O_5 material.

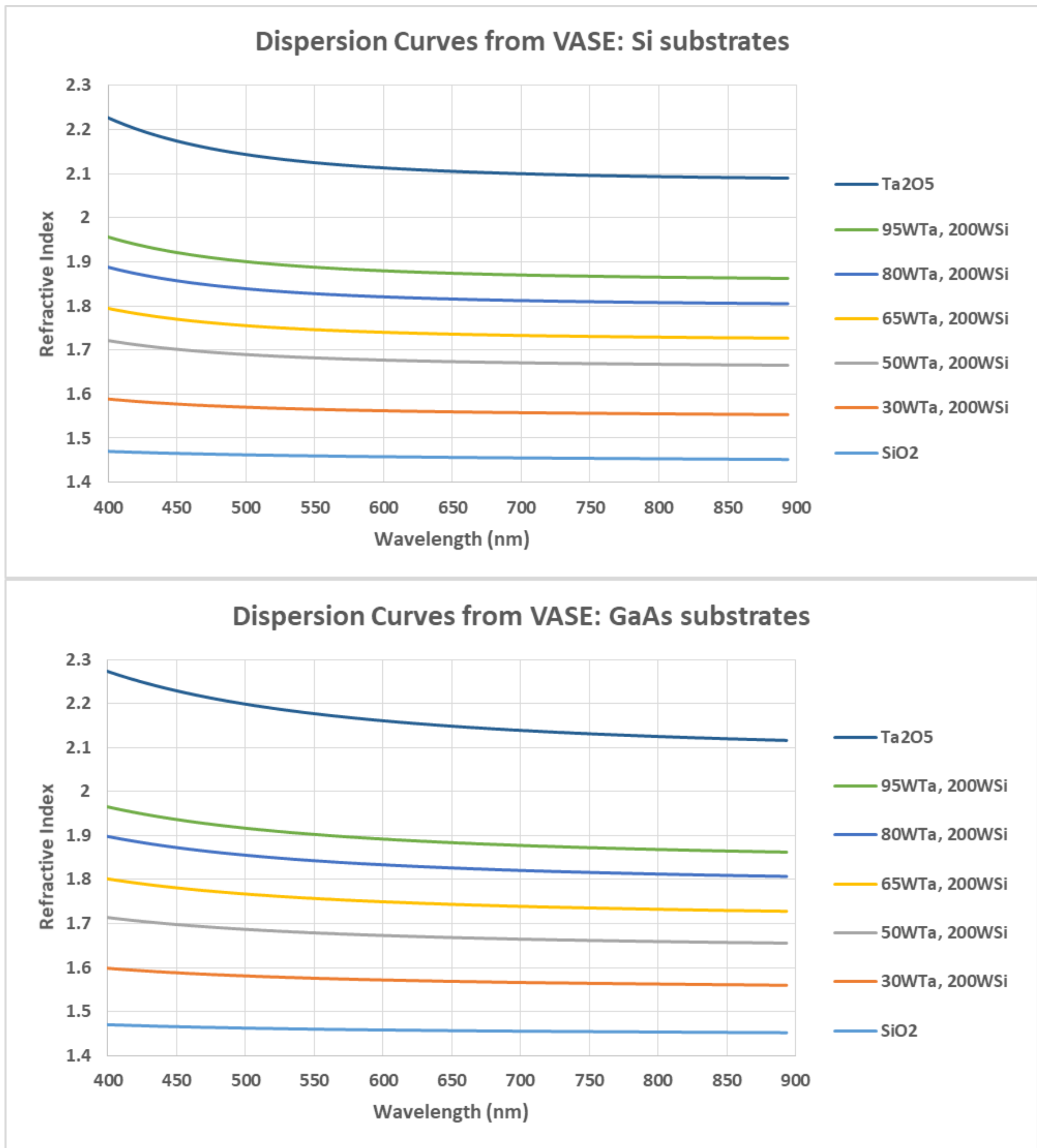

Figure 3.6: The modelled dispersion curves for each of the 14 films characterized in this work. Each film is labeled by the target powers (W) that were used during film growth.

It is additionally useful to look at the index of refraction at a single wavelength. Since each of the films were grown to a target optical thickness of 330nm by using the calculated index at 660nm during growth, this diode laser wavelength would be an ideal choice for this analysis. These values are described in list format in Table 3.1, which also describes the physical thickness of the films, as determined by the ellipsometer, and the calculated optical thickness at 660nm. The difference in calculated index between the films on two substrates is small, the maximum being for the two Ta_2O_5, the difference is 0.05. This gives confidence that the films match across substrates. Additionally, even though the index varies with composition, target optical thickness was reached for each film to within 30nm or less. For most of the films, the target optical thickness was achieved to within 10nm, however the larger discrepancy in the films with higher SiO_2 composition can be explained by the in-situ ellipsometry measurements indicating a low refractive index for SiO_2. This was resolved post-deposition using the VASE to increase the fit precision. The optical thickness can be visualized in Figure 2.6, where all of the samples appear close to the same color. Since there is some discrepancy in optical thickness of the SiO_2 films and the 30WTa, 200WSi films, this shows up in a color that is a little more red than the other samples.

In addition to the modeled dispersion curves, the J.A. Woollam ellipsometer analysis software CompleteEASE can be used to estimate the composition of the film, based on Bruggemann's Effective Medium Approximation (EMA). The composition is calculated based on the EMA volume fraction mixtures of the dispersion curves for SiO_2 and Ta_2O_5 shown in Figure 3.6.

The resultant estimated composition, plotted versus the refractive index at 660nm is shown in Figure 3.7. This plot shows two fits: one for the films on Si substrates and one for films on GaAs substrates. These are shown separately, as the films were grown at

Table 3.1: The modeled refractive index at 660 nm, the physical thickness of the films measured in nanometers, and the calculated optical thickness of the films, measured in nanometers.

Target Powers	Si Substrates			GaAs Substrate		
	n	Physical Thickness	Optical Thickness	n	Physical Thickness	Optical Thickness
95W Ta, 0W Si	2.10	157	330	2.15	150	323
95W Ta, 200W Si	1.87	182	340	1.88	173	325
80W Ta, 200W Si	1.81	186	337	1.83	179	328
65W Ta, 200W Si	1.74	192	334	1.74	189	329
50W Ta, 200W Si	1.67	202	337	1.67	197	329
30W Ta, 200W Si	1.56	231	360	1.57	223	350
0W Ta, 200W Si	1.46	247	360	1.46	244	356

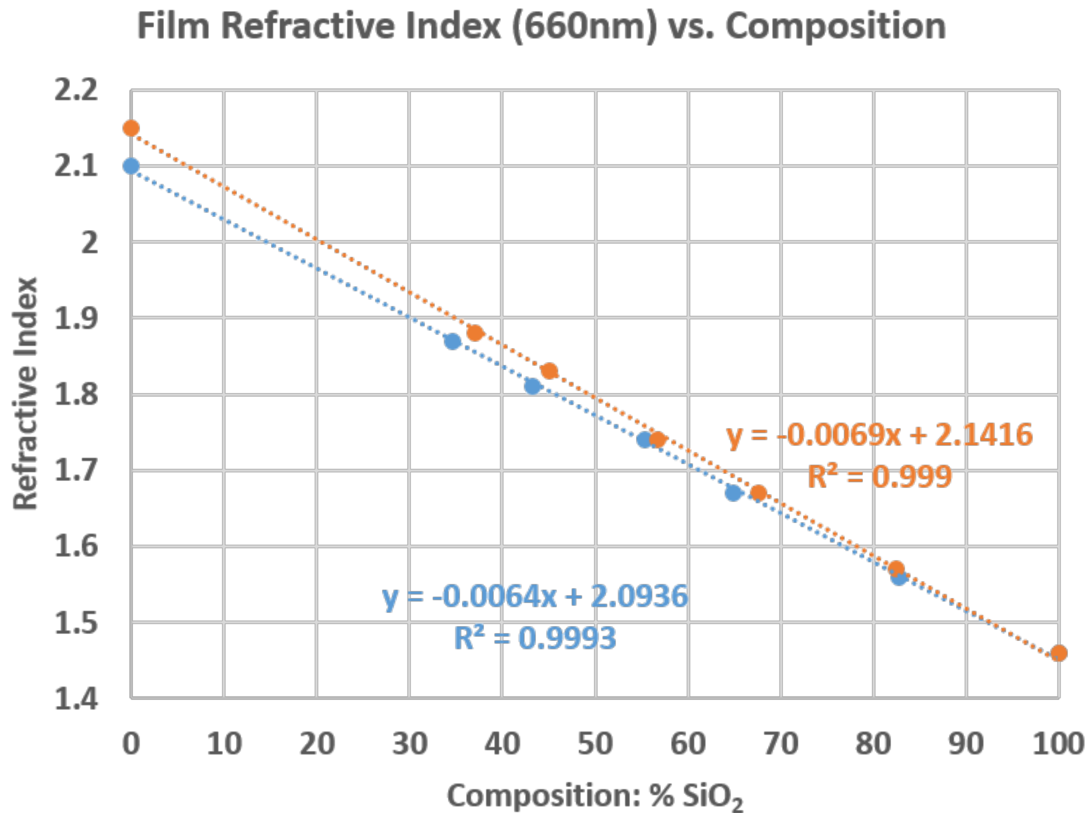

Figure 3.7: Modeled film composition and refractive index determined using the Bruggeman Effective Medium model in J.A. Woollam's CompleteEASE.

different times and so could have a slightly different composition. However, the variation in the modeled composition of the films between the two substrates is very small, with a run-to-run variability of less than 3%.

Both fits show a linear relationship between tantalum target power and film composition, with the R^2 value being greater than 0.99 for both sets of films. The difference between the slopes of the two curves is small, only 3.9%, indicating that the films are very similar between the two substrates.

The demonstration that the composition variation between the films in each series is small is important, as the measurements of the CTE and Young's Modulus using the two-substrate method will necessitate the use of two matching films, each on a different substrate. The variation in composition between the films increases the error in any CTE and Young's Modulus calculation.

An additional feature that is modeled using ellipsometry is the surface roughness of the film. This is modeled as a thin layer of effective medium %50 film and %50 air. Introducing some surface roughness in the model improved the fit for the films. The surface roughness is plotted in Figure 3.8 as a function of tantalum target power.

Based on this modeling, it appears that there is some surface roughness of the SiO_2 films, and that there is very little surface roughness for the Ta_2O_5 films. The co-sputtered films show a surface roughness between that of the two end-point materials, based on their composition. In Figure 3.8 this relationship has been fit with an exponential, however it is not self-evident that this will be the best fit function to describe the physical phenomenon of the growth of the film. However, the fits for this exponential model has a higher R^2 value

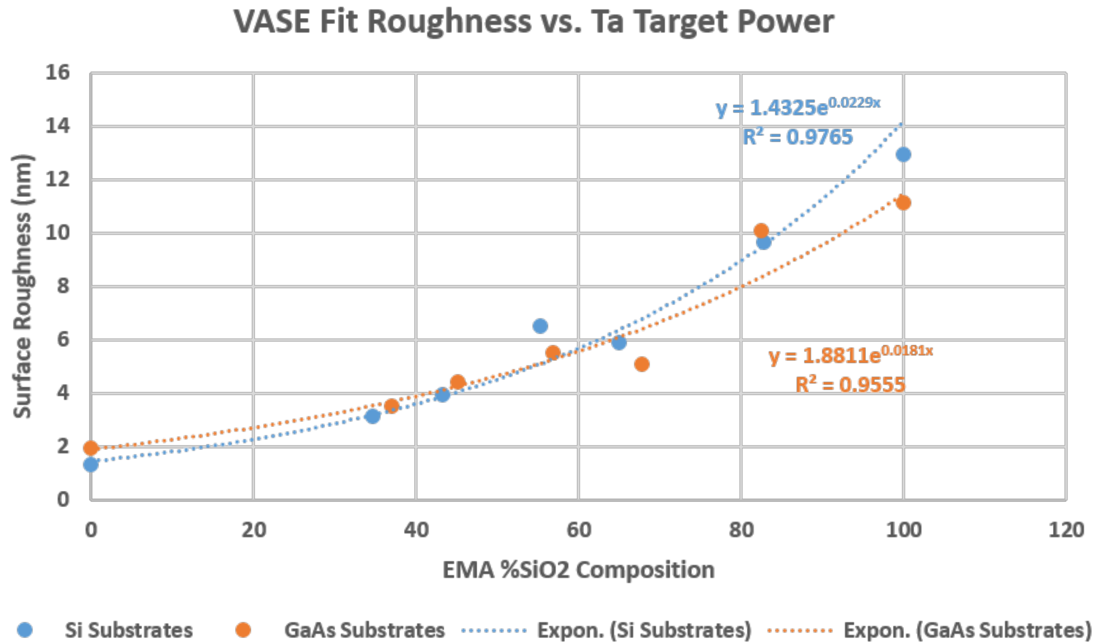

Figure 3.8: Modeled surface roughness versus modeled EMA composition, $\%SiO_2$.

than those with a simple linear fit (6.7% higher for the Si substrate data, 12% higher for the GaAs substrate data).

In order to demonstrate the efficacy of the models shown, where both dispersion and composition are determined, the MSE values calculated by the CompleteEASE software are published in Table 3.2. The MSE reflects the difference between the model and the measured data, and is calculated over the 510nm spectral range. The lower the MSE, the better the model matches the data. Generally, the acceptable maximum values for publishable MSE depend on the system complexity. It should be noted here that the simplest model in this series is the fit to the Palik data for the pure SiO_2 film. As this is a relatively simple model, these MSE values may be used as a demonstration of the lowest reasonable MSE for each series of films.

Table 3.2: The calculated MSE fits for the deposited films, calculated in connection with the dispersion curves shown in Figure 3.6.

Target Powers	MSE (Si Substrate)	MSE (GaAs Substrate)
95W Ta, 0W Si	6.127	7.051
95W Ta, 200W Si	8.066	10.074
80W Ta, 200W Si	8.58	11.769
65W Ta, 200W Si	8.371	8.477
50W Ta, 200W Si	10.054	8.859
30W Ta, 200W Si	5.077	8.558
0W Ta, 200W Si	10.486	8.821

Each of the 14 films were characterized using variable-angle spectroscopic ellipsometry, indicating that the films were high-quality SiO_2 and Ta_2O_5 films, and various mixtures in between. The ellipsometry data allowed for the estimation of the film material dispersion, for its thickness, and for its roughness. From the film optical dispersion, the composition was estimated, indicating that each series of films, while grown at different times, are indeed very similar.

3.4 Additional Methods of Characterization for Material Composition

In addition to ellipsometry, two other methods of characterization were used: another optical method using reflection spectra to ascertain the film optical constants, and energy-dispersive x-ray spectrscopy (EDX). Based on the data collected for these two methods, in addition to the ellipsometry, it was determined that ellipsometry was the best technique to determine the film composition.

3.4.1 Dispersion Fits Using Reflection Spectra

Another way in which to model the material composition using optical measurements is by using normal-incidence reflection spectra to determine the dispersion characteristics

of the film material. Similarly to ellipsometry, an effective medium model can be used in order to estimate the material composition based on its dispersion.

This method was used in order to obtain an estimate of the film composition. A Filmetrics normal-incidence spectrometer was used, which collected both normal-incidence reflection and transmission spectra from the samples. Since there was very little transmission through the silicon and gallium-arsenide substrates at the wavelenths measured by this spectrometer, only the reflection spectrum was used in order to find the best-fit dispersion curves.

Similar to the dispersion properties from the ellipsometer fits, the SiO_2 films fit well to the data reported by Palik [43]. For the Ta_2O_5 films, good fits were found using the dispersion curves which fit Ta_2O_5 films made by an industry partner.

The "goodness" of the fits were determined using a Global Merit Function, which indicates the root-mean-square difference between the model and the measured data. Since there is always some inherent noise in the measurement data, it is assumed that a Global Merit Function of 1.0 or less indicates a fit to within 1% spread in the measurement data.

The composition of the mixed-oxide films were modeled as an alloy of the SiO_2 and the Ta_2O_5 layers, using the effective index approach first described by Southwell in [44].

Good fits were found for all 14 of the modeled films, with a Global Merit Function of less than or equal to 2.0 for all modeled films. Two representative examples of the fits for the spectral reflectance fits are shown in Figure 3.9.

A couple of features of the spectral reflectance fits are noteworthy. The first item of note is that there are only two features that will be fit: the reflection minimum, and the

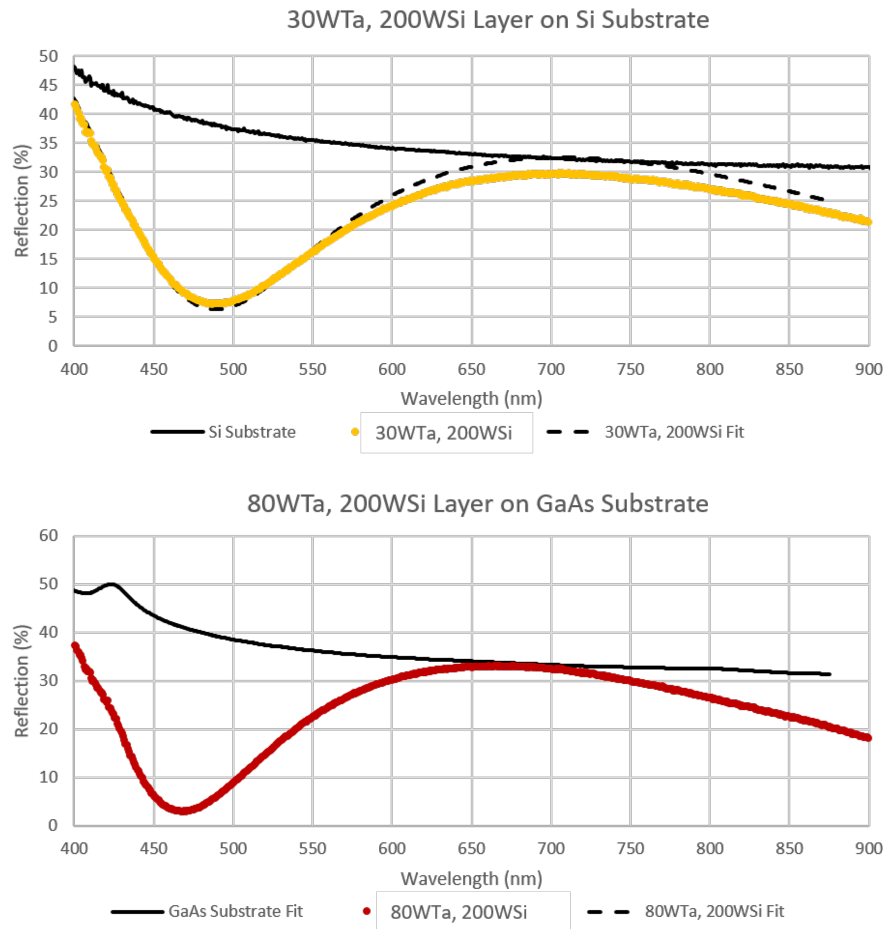

Figure 3.9: Two examples of the fits for the spectral reflectance.

reflection peak. The reflection minimum is indicative of the film index, as the depth of the minimum reflectance indicates a condition at which there is an anti-reflection condition met between the substrate and the film. Therefore, the precision to which this minimum is characterized is critical to the modeling of the dispersion relation for these thin films.

The location of this minimum, along with the broader location of the reflectance maximum contribute to the determination of the film thickness.

The reflectance peak spectral feature indicates the wavelength at which there is an absentee layer. These films were designed to have maximum reflectance at 660nm, which for these films will occur when there is an absentee layer of optical thickness 330nm, also known as the half-wave condition. If the measurements of reflectance have high precision, and the film is homogeneuos, a single layer of half-wave optical thickness will meet the conditions of the half-wave layer and have the same reflectance as the substrate. This condition is met in the lower of the graphs in Figure 3.9, but not in the upper graph. This difference could come from variation in reflectance measurements or in inhomogeneity in the film.

It was found during the data analysis for these reflectance measurements that the calibration and reflectance standard used for the measurements changed the magnitude of the reflectance of the system. Since there is great sensitivity of the dispersion curves to the magnitude of the reflectance at these key locations, it was determined that ellipsometry would be a better method to estimate the film composition optically.

3.4.2 Verification of Film Composition using EDX

Energy-dispersive X-ray spectroscopy (EDX) is a direct way to measure the composition of matter of thin films. This measurement method was done using a system from EDAX, which mounts into a scanning electron microscope (SEM) instrument. A focused electron-beam from the SEM instrument is used to eject the ground-state electrons from the atoms in the bulk of the film. The electrons that decay to the ground state, replacing the ejected electrons release X-rays which conserve the total energy of the system. The energy of these X-rays correspond to the band-structure of the atom from which it came, each atom having a unique structure. This phenomenon allows for the identification of the atomic composition of the film through the use of an X-ray spectrometer [45].

For these films, the relative composition of silicon, tantalum, and oxygen could allow for the determination of the film composition directly. However, it was discovered during measurement that the X-Ray emission energy from the silicon and tantalum where too close together to be resolved by the spectrometer.

Figure 3.10 shows a plot of the spectrometer counts versus energy for a film on a gallium-arsenide substrate. The peaks for oxygen, gallium, and aresnic are well-defined and separated from each other. However, the tantalum and silicon peaks are indistinguishable with this resolution. According to the Periodic Table for EDS Analysis, published by JEOL [46], the characteristic X-ray from Silicon has an energy of 1.709 keV, while the characteristic X-ray from Tantalum has an energy of 1.739 keV, only 0.03 keV difference in energy.

To estimate the spectrometer resolution, the oxygen line can be investigated. It would be expected that the oxygen measured energy would be a single line at 0.525 keV, however the limitations of diffraction spread the collected light over the spectrometer detector,

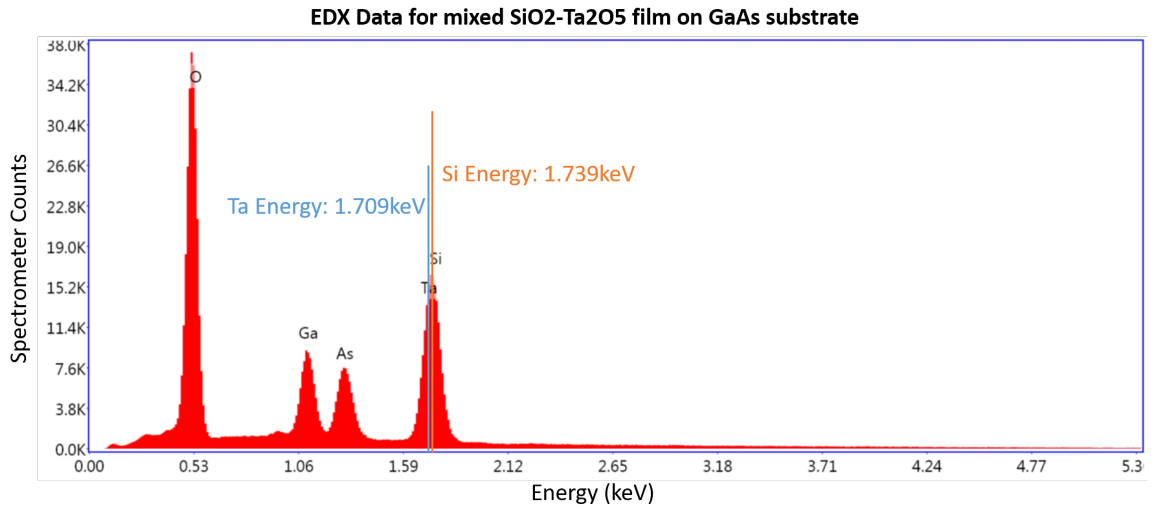

Figure 3.10: The X-ray spectrometer counts versus energy (keV) for the X-rays emitted during EDX.

broadening the peak. The full width of this oxygen peak appears to be approximately 0.015 keV. This value is close to the reported spectrometer resolution of 130 eV, which defines the difference in energy peaks which can be distinguished by the instrument. Since the two peaks needed to determine the composition of the films are closer together than this resolution (30 eV energy difference), this method cannot be effectively used to determine the composition of the films.

CHAPTER IV

THEORY FOR CALCULATING THIN FILM THERMO-MECHANICAL PROPERTIES

Gerald Stoney was the first to describe how total stress in a thin film can be indirectly determined by observing the response of the substrate to the force applied by the film. Due to the adhesion forces between the substrate and film, the forces in the film, interacting with the substrate at the film-substrate interface will cause the substrate to bend.

This chapter will derive Stoney's stress equation from first principles, will apply it to the determination of thermal stress in a system and relate this stress to the CTE and the Young's Modulus of the film material. A discussion is also included for the incorporation of multiple sources of uncertainty into the calculations of these values.

4.1 Theory of Stress in Thin Films

The theory of stress-development in thin films is extensive and dates back over a century. Stress, in general terms, is a measure of the force per unit area acting on a system, and therefore has the same units as pressure (Pascal). There are many types of stress, which refer to the geometry of the system, along with the direction of the force with respect to the area in question. For stress in thin films, the typical type of stress referenced is a uni-axial in-plane stress, meaning that the cross-section in question is the thickness of the film, and the stress is perpendicular to that surface. Such in-plane stresses are referred to as compressive and tensile stresses and a diagram of the forces involved are shown in Figure 4.1.

The substrate curvature shown in this figure is a result of the balancing of forces between the substrate and the film, which are adhered together. Using the compressive stress case as

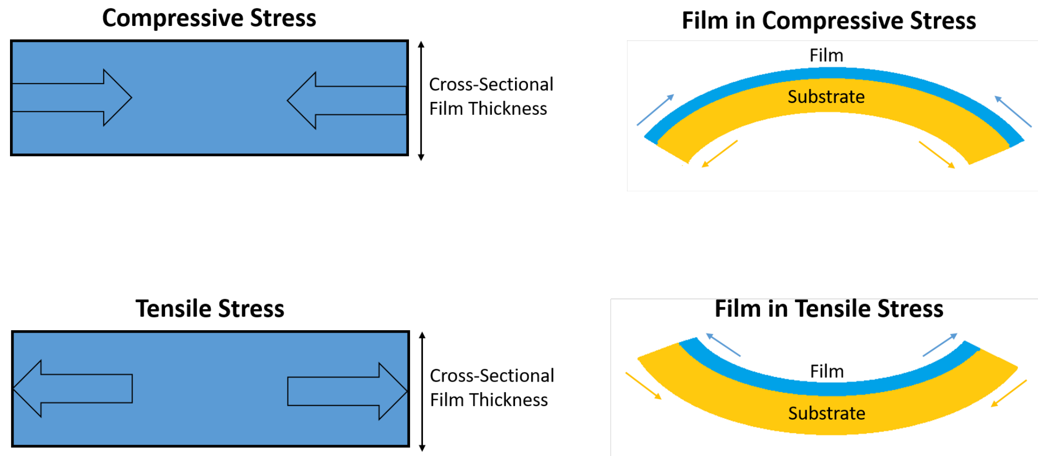

Figure 4.1: At left, compressive and tensile stress is shown in the film alone. The arrows indicate force direction, which are normal to the cross-sectional thickness. The right demonstrates that same film when applied to a substrate. The substrate will also be under tension (above) or compression (below) to balance out the stresses in the films.

an example, the atoms in the film are closer together than their relaxed state, and if given the opportunity would move apart, cause the film to elongate. Assuming the film remains adhered to the substrate, it will limit the elongation of the film, causing strain. The balance of the strain from the substrate limiting the expansion of the film and the strain from the film elongating the substrate creates the characteristic substrate curvature.

Stress in thin films develops from a number of sources, including deposition parameters and substrate and film material properties. Magnetron sputtering deposition techniques typically result in compressive films. This compressive stress is the result of atomic peening of the film during growth, where the bombardment of the substrate and film by the argon ions in the plasma during the growth compress the film, removing voids [47]. Atomic peening, in addition to the high energies of the sputtered species upon arrival at the substrate surface, can result in a high compressive stress in the film. Some compressive stress in the film will prevent crack initiation and propagation through the film, however with too

much compressive stress delamination of the film from the substrate can occur. The balance between the film-substrate adhesion strength and the film stress is key to the system durability.

The stress introduced into the system through the process of film growth is called "intrinsic stress" (σ_{int}). In addition to the stresses introduced during growth, there are two other ways in which stress is introduced into the system. One of these ways is "thermal stress" (σ_{therm}), and the other is "applied stress" (σ_{ap}).

Thermal stress is introduced when the temperature of the film-substrate system varies from the deposition temperature. At the deposition temperature, the thermal stress can be assumed to be zero. However, all materials expand or contract with changes in temperature, which is characterized by a Coefficient of Thermal Expansion (CTE). When the CTE of the substrate is different from that of the film, the different rates of expansion/contraction will introduce a thermal stress at the interface between the film and substrate as shown in Figure 4.2. This stress is a function of both the amount of size change due to the differences in the Coefficients of Thermal Expansion of the two materials, along with the elasticity of the two materials, characterized by their Elastic or Young's Modulus.

The equation for thermal stress in a system can be derived using the definition of the Young's Modulus (E), which is the ratio of the stress (σ) and strain (ϵ) in a material, as shown in Eqn. 4.1, where F/A is a pressure, or force per unit area, and $\Delta l/l$ is the fractional change in length of the object. In other words, this quantity is a measure of the amount of pressure needed to cause deformation of the object (size change). For thin films, the only length change that is considered is the in-plane length change. The Poisson ratio will later be introduced to account for the two-dimensional change in the film.

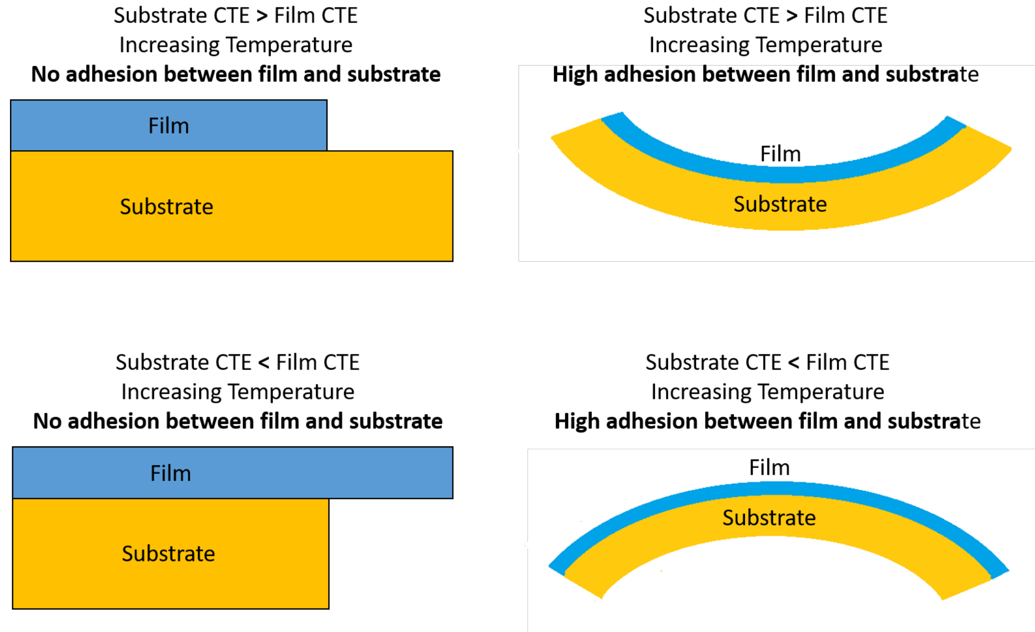

Figure 4.2: A demonstration of the origins of thermal stress. The combination of differing CTE's between the substrate and film with high adhesion between them introduces curvature in the system.

$$E \equiv \frac{\sigma}{\epsilon} = \frac{F/A}{\Delta l/l} \tag{4.1}$$

From this definition of the Young's modulus, it becomes apparent that the stress in the system is the product of the Young's Modulus and the strain, as shown in Eqn. 4.2.

$$\sigma = E\epsilon = E \times \frac{\Delta l}{l} \tag{4.2}$$

Here it is prudent to stop and think about the cause of the strain in this system. As shown in Figure 4.2, the strain in the system is due to the difference between the change in size of the substrate and the change in size of the film. Therefore, Eqn. 4.2 should be re-written to take into account the two materials involved: the film (f) and the substrate

(s) so that the source of strain in the system is taken into account. Given that the film and the substrate were the same size at the deposition temperature (T_d), Eqn. 4.2 is re-written as Eqn. 4.3, where E_f is the Young's Modulus of the film.

$$\sigma_f = E_f \times \frac{(\Delta l_f - \Delta l_s)}{l} \tag{4.3}$$

This change in size is a result of the heating and cooling of the system away from the deposition temperature, and is described by the CTE of the materials, defined in Eqn. 4.4. Here, the variable l denotes the length of the object, and the variable T is the temperature.

$$CTE = \frac{1}{l} \times \frac{\Delta l}{\Delta T} \tag{4.4}$$

This equation demonstrates a linear relationship, which is typically a good approximation over temperature ranges for which the materials involved do not experience any phase change. For this study, the linear CTE that will be used is specified from $0 - 100°$C, which is well within that range for the materials investigated in this study.

The difference in CTE between the substrate and the thin film is shown in Eqn. 4.5. Here it is important to note that at the deposition temperature, the size of the film and the substrate are equal ($l_f = l_s$). Additionally, the temperature of the two parts of the system will be equal in all but the most extreme cases ($T_f = T_s$). Given these pieces of information, Eqn. 4.5 can be simplified into Eqn. 4.6

$$CTE_f - CTE_s = \left(\frac{1}{l_f} \times \frac{\Delta l_f}{\Delta l_f}\right) - \left(\frac{1}{l_s} \times \frac{\Delta l_s}{\Delta l_s}\right) \tag{4.5}$$

$$CTE_f - CTE_s = \frac{1}{l} \times \frac{(\Delta l_f - \Delta l_s)}{(T - T_d)} \tag{4.6}$$

By combining Eqn. 4.3 and 4.6, the thermal stress in the film is shown in Eqn. 4.7. Unlike intrinsic stress, thermal stress is independent of the deposition energy, and is dependent on the material properties of the film and substrate along with the temperature. This equation also follows the sign convention where compressive stress is negative, and tensile stress is positive.

$$\sigma_{therm} = E_f \left(CTE_f - CTE_s\right)(T - T_d) \tag{4.7}$$

The last source of stress can be called "applied stress" (σ_{ap}), which includes any applied stress to the system after deposition. This could include the bending of the substrate during handling, the cutting of the substrate into smaller pieces, or the mounting or clamping of the substrate into a holder. All of these things can add stress to the system, increasing the total stress. An equation for the total stress in a thin-film-coated system is shown in Eqn. 4.8.

$$\sigma_{total} = \sigma_{int} + \sigma_{therm} + \sigma_{ap} \tag{4.8}$$

Many other papers which investigate the effects of thin film stress focus on the intrinsic stress component and will therefore combine the thermal and other applied stress into a single "extrinsic" stress category. In this work, the thermal stress is being isolated and measured in order to determine the thermo-mechanical properties of the thin films. For

this reason, the thermal stress has been singled out in the stress equation, and all other applied forces in the substrate-film system are categorized under "applied" stress.

4.2 Determination of Total Film Stress through Substrate Bending

Total stress in a thin film can be measured indirectly by measuring the curvature of the substrate. This phenomenon, where the properties of the film can be derived using the properties of the substrate was the groundbreaking work of Gerald Stoney in his 1909 paper "The tension of metallic films deposited by electrolysis" [48]. In his paper, he describes that the metallic films that he has deposited cause their substrates to bend. He postulates that this bending is due to the balancing of forces between the substrate and the films, and that since the system is in equilibrium, a great deal of information regarding the film can be deduced by measuring the curvature of the substrate.

Stoney derived his famous equation for stress by understanding that the bending in the substrate is a result of the strain in the system, and this strain is the result of the balancing of forces between the film and the substrate. The force in the film causes an equal and opposite force within the substrate, distributed throughout its thickness such that the total force in the system is zero. A diagram of the forces distributed throughout the substrate is demonstrated by the horizontal arrows in Figure 4.3, which is a diagram inspired by the detailed theory outlined by Southwell in [6].

Given the nature of a curved substrate, one edge of the substrate must be in tension, while the other is in compression. This phenomenon is shown in also shown in Figure 4.3. Given this, Stoney argued that there must exist some neutral plane, for which the force is equal to zero, denoted as "b".

Additionally, the force from the film is acting within the plane of the film, which causes a torque on the system, where the substrate thickness acts as a lever arm for the force. Since the system is in equilibrium, the net torque must also be zero. Using these concepts, Stoney's Equation can be derived.

The argument that Stoney gives for the relationship between the radius of curvature of the substrate and the stress in the film is centered around the concept of strain, which is defined in Eqn. 4.1 as the fractional change in length of an object. The change in length of an object is due to the force applied to it, in this case by the film. The relationship between the stress (force per unit area) and strain is the Young's Modulus (E).

As with the derivation of the thermal stress, the total stress in the system can be derived starting from Eqn. 4.2. Referencing Figure 4.3, we can define the change in length of the substrate with reference to the force-neutral plane as the original length. Using the geometry of Figure 4.3, the strain can be shown in Eqn. 4.9, and given the assumption that the radius of curvature is much larger than the substrate length, the trigonometry function can be replaced with their small-angle approximations.

$$\epsilon \equiv \frac{\Delta L}{L} = \frac{(b+z)\tan\theta}{r\sin\theta} \approx \frac{(b+z)}{r} \tag{4.9}$$

Young's Modulus defines the relationship between strain and stress for a given material, and therefore can be used in this case to solve for the stress in the substrate due to the film. Subsequently, this stress definition can be used to define both the force and the torque in the system, whose net total must be zero. Eqns. 4.10 show the stress, the force, and the torque equations for the system.

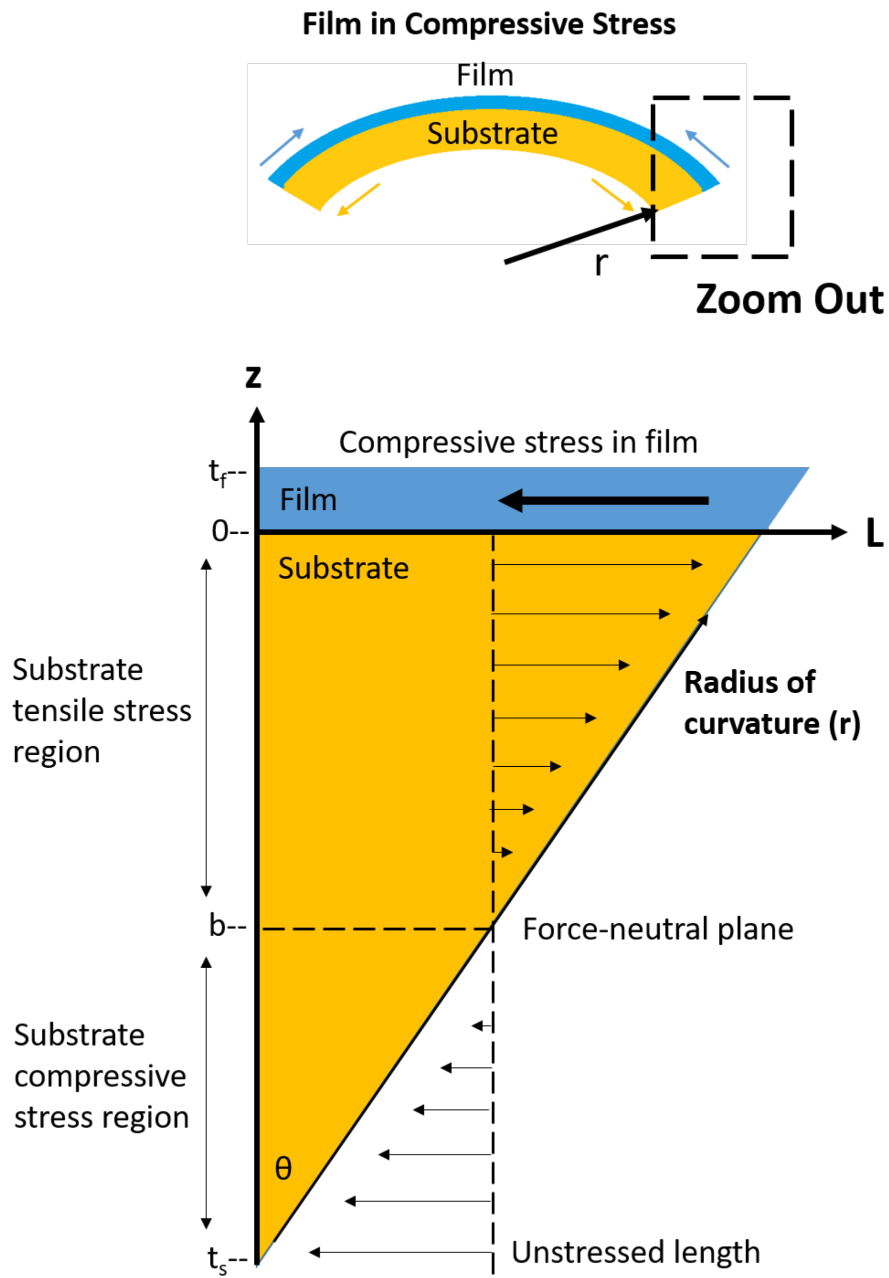

Figure 4.3: Diagram of the strain in the substrate due to the stress of a compressive film. The horizontal arrows denote the force in the system.

$$\sigma = E\epsilon = \frac{E_s}{r}(b+z)$$

$$F = \sigma dz = \frac{E_s}{r}(b+z)dz \tag{4.10}$$

$$\tau = Fz = \frac{E_s}{r}(b+z)zdz$$

The definitions of stress, force, and torque show that these values are defined by a given plane of depth "z", and that they are functions of depth. The solution to the stress equation comes from the knowledge that a system in equilibrium has a net zero force and a net zero torque. The net torque can be calculated by integrating the torque function over the system depth, as shown in Eqn. 4.11. The equations can be simplified with the stipulation that the thickness of the substrate is much greater than the thickness of the film ($t_s >> t_f$). This assumption that the film thickness is very small allows for the condition where there is no torque contribution from the film, as it has no lever arm due to its very small thickness. This is the condition that makes the Stoney Equation possible.

$$\Sigma\tau = \int_{-t_s}^{0} \frac{E_s}{r}(b+z)zdz = 0$$

$$= -\frac{b}{2}t_s^2 + \frac{1}{3}t_s^3 = 0 \tag{4.11}$$

The net torque equation, Eqn. 4.11, allows for the calculation of the location of the neutral plane, which is key to calculating the stress and force from Eqn. 4.10. Using this equation, it is a simple algebraic step to find that the location of the neutral plane is 2/3 the depth of the substrate ($b = \frac{2}{3}t_s$).

This is a notable conclusion in itself, as the location of the neutral plane is not dependent on the magnitude of the stress in the thin film or on the relative thicknesses of the substrate and film.

The next concept that Stoney utilizes to determine the stress in the thin film is Newton's Third Law. For this case, the force in the film must be balanced by the force in the substrate, as the system is in equilibrium. Having solved for the position of the neutral plane, the total force in the substrate can be calculated, as shown in Eqn. 4.12. It is noteworthy that the determination of the total force only needs to consider the force in the substrate.

$$\begin{aligned} F_s &= \int_{-t_s}^{0} \frac{E_s}{r}(b+z)dz \\ &= \frac{1}{6}\frac{E_s}{r}t_s^2 \end{aligned} \tag{4.12}$$

Given that the force in the film is equal in magnitude (and opposite in direction) to the total force within the substrate, the stress can be calculated from this equation, as shown in Eqn. 4.13. The sign convention used for these equations defines compressive stress as negative, and tensile stress as positive. Since the example that is worked in this paper, shown in Figure 4.3 is that of a compressive film, a negative stress is consistent with the sign convention.

$$\sigma_f = -\frac{1}{6}\frac{E_s}{r}\frac{t_s^2}{t_f} \tag{4.13}$$

There is one more piece of information to consider before the Stoney equation for stress in thin films is completed. In his original paper, Stoney was considering the deposition of

nickel onto thin steel rules. In this context the length of the rule was nearly ten times as long as the width. For this reason, Stoney considered only the dimensional change in a single direction, and could therefore use the Young's modulus in his stress equation [48].

For thin films on two-dimensional substrates, such as silicon or glass discs, a two-dimensional shape change must be taken into account. In order to characterize the change in width of the film in response to the change in length, the Poisson ratio can be used. It is generally accepted that a Biaxial Modulus can be defined as in Eqn. 4.14 if the in-plane stresses are equal in every direction [49]. This is a reasonable expectation for these thin films, as we expect the stress to be in-plane and uniform over the film. Additionally, the films in question in this report are amorphous, so should have equal stress distribution along each of the in-plane axes.

$$E' = \frac{E}{(1-\nu)} \tag{4.14}$$

Replacing the uniaxial Young's Modulus in Eqn. 4.13 with the Biaxial Modulus in Eqn. 4.14 so that the equation represents a two-dimensional film, the final version of the Stoney's Equation s shown in Eqn. 4.15.

$$\sigma_f = -\frac{1}{6}\frac{t_s^2}{t_f}\frac{E_s}{r(1-\nu_s)} \tag{4.15}$$

This is the equation that is commonly used to relate the total stress in a film to the bending curvature of the substrate. Notice that the stress is determined almost exclusively from the substrate properties, and that the only film property that is considered is its

thickness. Stoney's Equation is the total stress in the system, which takes into account both the intrinsic and the thermal components of stress.

4.3 Coefficient of Thermal Expansion (CTE) and Young's Modulus (E) Calculations from Thermal Stress

The effects of the thermal stress in the system can be isolated from the intrinsic stress effects by recording the change in curvature versus temperature. It is assumed that intrinsic stress is constant with temperature over the temperature range of interest (0-100°C), as the films are not expected to anneal. Therefore the change in curvature as a function of temperature is a direct measurement of the thermal stress in the system.

Recall from Eqn. 4.7 that the thermal stress in the film is a function of both the CTE and the Young's modulus of the film and substrate materials. By isolating the effects of the thermal stress alone, it is possible to solve directly for the CTE and the Young's Modulus of the film by combining Eqns. 4.7 and 4.15. This results is Eqn. 4.16, where ΔC is the change in curvature with units of curvature-diopters (m^{-1}). The $\pm$ indicates that opposites trends will be measured if the curvature is measured from the film side versus the substrate side. For this convention, measurements from the film-side use the positive sign, while measurements from the substrate-side use the negative sign.

$$CTE_f = CTE_s \pm \frac{1}{6}\frac{t_s^2}{t_f}\frac{E_s(1-\nu_f)}{E_f(1-\nu_s)}\frac{\Delta C}{\Delta T} \tag{4.16}$$

Assuming that the substrates are a well-characterized material, the values of the substrate properties will be known. This results in two unknowns in the above equation: the CTE of the film, and the Young's Modulus of the film. Two ways in which these

thermo-mechanical properties can be determined are explored in this work, in addition to a discussion of the strengths and weaknesses of both methods.

The first method is to deposit the same film onto two substrates with different thermo-mechanical properties. The curvature change with temperature will be different for each substrate, allowing for two separate equations (one for each substrate) that can be used to solve for both CTE_f and E_f simultaneously [11, 50].

The second method is to measure the Young's Modulus of the film by a different method, and incorporate it into the above a equation as a known quantity. For this work, the direct measurement of the Young's Modulus was done using nano-indentation.

4.3.1 Calculation of CTE and Young's Modulus using the Two-Substrate Method

For the Two-Substrate Method, the same film is grown on two different substrates with different thermo-mechanical properties. Using Eqn. 4.16, an expression can be determined for the calculation of the CTE of the films in terms of the film thicknesses and the substrate parameters. This is shown in Eqns. 4.17.

$$\begin{aligned} CTE_f &= CTE_{s1} \pm \frac{1}{6}\frac{t_{s1}^2}{t_{f1}}\frac{E_{s1}(1-\nu_f)}{E_f(1-\nu_{s1})}\frac{\Delta C_1}{\Delta T} \\ CTE_f &= CTE_{s2} \pm \frac{1}{6}\frac{t_{s2}^2}{t_{f2}}\frac{E_{s2}(1-\nu_f)}{E_f(1-\nu_{s2})}\frac{\Delta C_2}{\Delta T} \end{aligned} \tag{4.17}$$

This set of equations can be solved as analytic expressions for both the CTE and the modulus of the film, as shown in Eqns. 4.18, where each film property is dependant on the curvature change from both samples. The use of the factor Q is included only to simplify the

CTE and Young's Modulus equations, gathering together the constants, and highlighting the measured quantities.

$$CTE_f = CTE_{s1} \pm \frac{Q_1 \left(CTE_{s1} - CTE_{s2}\right) \left(\frac{\Delta C_1}{\Delta T}\right)}{Q_1 \left(\frac{\Delta C_1}{\Delta T}\right) - Q_2 \left(\frac{\Delta C_2}{\Delta T}\right)}$$

$$E_f = \pm(1 - \nu_f) \frac{Q_1 \left(\frac{\Delta C_1}{\Delta T}\right) - Q_2 \left(\frac{\Delta C_2}{\Delta T}\right)}{CTE_{s1} - CTE_{s2}}$$

$$Q_1 = \frac{t_{s1}^2 E_{s1}}{6t_{f1}(1 - \nu_{s1})}$$

$$Q_2 = \frac{t_{s2}^2 E_{s2}}{6t_{f2}(1 - \nu_{s2})} \tag{4.18}$$

One of the strengths of this method is that both the CTE and Young's Modulus can be calculated from simple curvature measurements. This can be an easy way to measure the Young's Modulus of a thin film without the use of nano-indentation, which is often expensive instrumentation.

The drawback, however, comes from the compounding of the uncertainties from two measurements. As will be investigated thoroughly in a later section, data from the curvature versus temperature slope is described by a linearly fit to measured data. Each of these fits has some error. Both the CTE and the Young's Modulus calculations here are then very sensitive to any uncertainties in these fits.

4.3.2 Calculation of CTE from Single-Substrate Method

The calculation of the film CTE from a single-substrate requires the knowledge of the film modulus, which can be determined using nano-indentation. This is a reliable method for determining the modulus of thin films, however the thinner the film, the more the substrate properties will affect the measurement. After completing the nano-indentation measurements, the measured modulus can be used in Eqn. 4.16 to find the film CTE.

The strength of this method is that only a single sample is needed in order to determine both the CTE and the modulus of the film. This removes the need to deposit two identical films. The drawback of this method is that nano-indentation is a destructive test, and can be an expensive instrument to obtain and maintain.

4.3.3 Incorporation of Uncertainty from Two Measurement Sources

For both methods detailed above, it is important to be able to estimate the uncertainty in the measurements. For the two-substrate method, the sources of the uncertainty that are considered in this study come from the fits of the curvature versus temperature to measured data points. Since both the calculated CTE and modulus depend on two slope fits, it is imperative that both are taken into consideration in the calculations, and the total uncertainty reported.

For the single-substrate method, the calculation of the CTE and the modulus depend on a single fit for curvature versus temperature, but should also include uncertainty from a series of nano-indentation measurements. As with the two-substrate method, the uncertainty in the two measurements may be different magnitudes, and both must be taken into account in order to report an accurate estimate of uncertainty.

For this work, the method that is used to take into account uncertainty from two measurement sources is as follows. First, a normal distribution is created for each measurement, centered on the measured value, with a standard deviation equal to the standard deviation of the measurement set (in the case of nano-indentation) or standard error in the fit (in the case of the curvature versus temperature linear fits). Each of these distributions is randomly sampled and that random number is used as an input into the calculation of the CTE and the Young's modulus. This results in a normal distribution of the CTE and a normal distribution of the Young's modulus, centered around the calculation which uses the measured values, with a standard deviation equal to the uncertainty of the calculated values. Therefore, the center of the normal distribution is the reported values, and the standard deviation of the distribution is reported as the uncertainty.

In this way, uncertainties from multiple sources are incorporated into the calculations of both the CTE and Young's modulus, for both the single and two-substrate methods in order to report most accurately the uncertainties in the measurements.

CHAPTER V

MEASUREMENTS OF THIN FILM THERMO-MECHANICAL PROPERTIES

The coefficient of thermal expansion and the Young's Modulus of the films were calculated using two different methods. The two-substrate method utilizes the change in curvature with temperature of the same film applied to two different substrate materials. It became apparent that this technique was sensitive to measurement uncertainty. Therefore, an additional technique was used in order to increase the measurement precision. This technique utilized nano-indentation to determine the Young's modulus of each of the films. This measurement allowed for the calculation of the film CTE with a single thermal stress measurement, increasing the precision. A discussion of these measurement instruments, techniques, and results will be shown.

5.1 Thermal Stress Measurement Technique

As discussed in Section 4.3, the CTE and Young's Modulus of a film can be determined by measuring the substrate curvature, if the thermal stress can be isolated from the intrinsic stress. One method to isolate the thermal stress effects is to measure the change in curvature as a function of temperature. Here, it is assumed that the intrinsic stress in the film has its origins in the deposition of the film, and is therefore temperature-invariant. This is a reasonable assumption given that the source of this intrinsic stress is the atomic peening effects during the sputter deposition of the film. Therefore, the total curvature measured at any given temperature is the sum of the intrinsic and thermal stresses, however the change in curvature as a function of temperature is a marker of the thermal stress only.

5.1.1 Instrumentation

The system used to measure the curvature versus temperature is designed and custom-built by Randy Hall of Conejo Valley Research, in collaboration with Bill Southwell of Table Mountain Optics for this purpose. The instrument consists of three main parts: the generation of parallel laser beams, the environmental chamber with sample holder, and the camera capture of the reflected beams. The operating principle of the instrument is as follows: parallel beams reflected off a curved mirror will deviate based on the curvature of that mirror.

Two parallel beams are produced from a single HeNe (632nm) laser source operating in the Gaussian mode. This is done through reflection from a thick optic which has been coated with three unique interference filters, designed by Bill Southwell of Table Mountain Optics and deposited by LohnStar Optics, Inc. The purpose of these coatings is to create two, equal-intensity beams, traveling parallel paths, whose intensity is close to half of the input laser intensity. The front of the optic is coated where half of the surface has a coating designed for 50% reflection at the laser wavelength, while the other half of the surface is coated with an anti-reflection (AR) coating. These two coatings were designed so that they were deposited at the same time, with the first layers of the coating layers being the AR coating, and the total coating creating the 50% reflection. The back surface of the thick optic was coated with a 100% reflector interference filter. All three filters are designed to be used at 45° incident angle. In summation, the dual-beam is created when 50% of the laser is reflected upon interaction with that coating. The 50% of the beam that is transmitted is reflected nearly 100% on the back surface of the optic. The thick optic creates a displacement in the beam due which allows it to exit the optic through the side

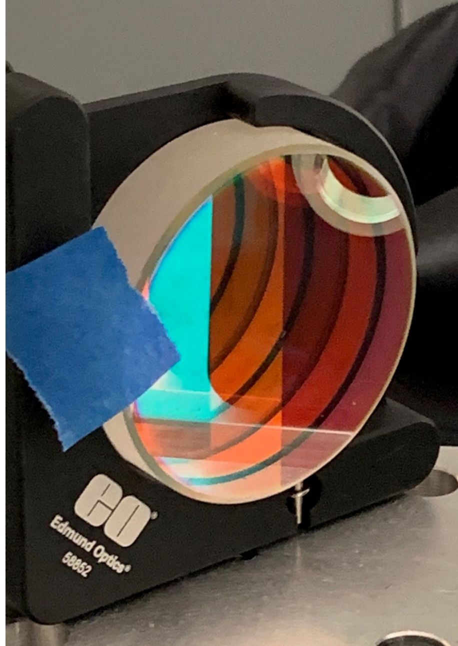

Figure 5.1: The custom-designed beam-splitter used to create the dual-beam for the thermal stress measurements. Designs of the three applied interference coatings were done by Table Mountain Optics, and the filters were grown by LohnStar Optics, Inc.

that is coated with an AR. These two beams travel in parallel, 5.4 mm apart. A picture of this beam-splitter optic is shown in Figure 5.1.

After these parallel beams are generated, they are reflected off a turning "scraper" mirror, and enter the environmental chamber through the optical port. The turning mirror is referred to as a scraper mirror because the beams will be reflected at the top edge of the mirror. Upon reflection from the sample, the system is aligned in such a way that the reflected beams will pass just above the optic. This optic was used instead of a beam-splitter, as the beam-splitter has more surfaces which cause multiple reflections which can confound the data. The optical port in the chamber is a dual-pain window filled with air. This allows for an optical probe to enter and exit the chamber while it maintains the temperature setting.

The environmental chamber is a Tenney Junior Environmental Test Chamber from Thermal Product Solutions (TPS). This chamber has an interior size of 1.2 cubic feet, with a temperature range of -68 to $+180°$C. Inside the chamber is a mount which holds the test sample or reference optical flat.

Images of the exterior and interior of the environmental chamber are shown in Figure 5.2. In this image, the reference optical flat sits in the sample holder, and red arrows show how the dual-beam enters the chamber. The two beams will be reflected from the sample, and travel back along the same path in the opposite direction back out of the chamber. Shown also is the fan which blows hot or cold air into the chamber during temperature set-point changes. It was postulated during early testing that the effect of this fan blowing down onto the substrate could cause it to change temperature much faster than the chamber interior, introducing systematic noise. Therefore, an aluminum sheet was added which blocks the direct airflow from the fan onto the substrate. Lastly, a thermocouple is attached to the mounting fixture, to monitor the temperature of the mounting block.

The last part of the instrument is the capture of an image of the two laser spots. After reflection off the sample, the two beams are directed back out of the chamber, through the optical port. They pass above the "scraper" mirror and encounter a rotating screen, which helps to eliminate the laser speckle. A camera is focused onto the plane of the rotating screen. An exposure time of 1 second for the camera, coupled with a screen rotation speed of 120RPM allows for two full screen rotations during the camera exposure time, averaging out the laser speckle in the image. An image of the exterior optics for the thermal measurements are shown in Figure 5.3.

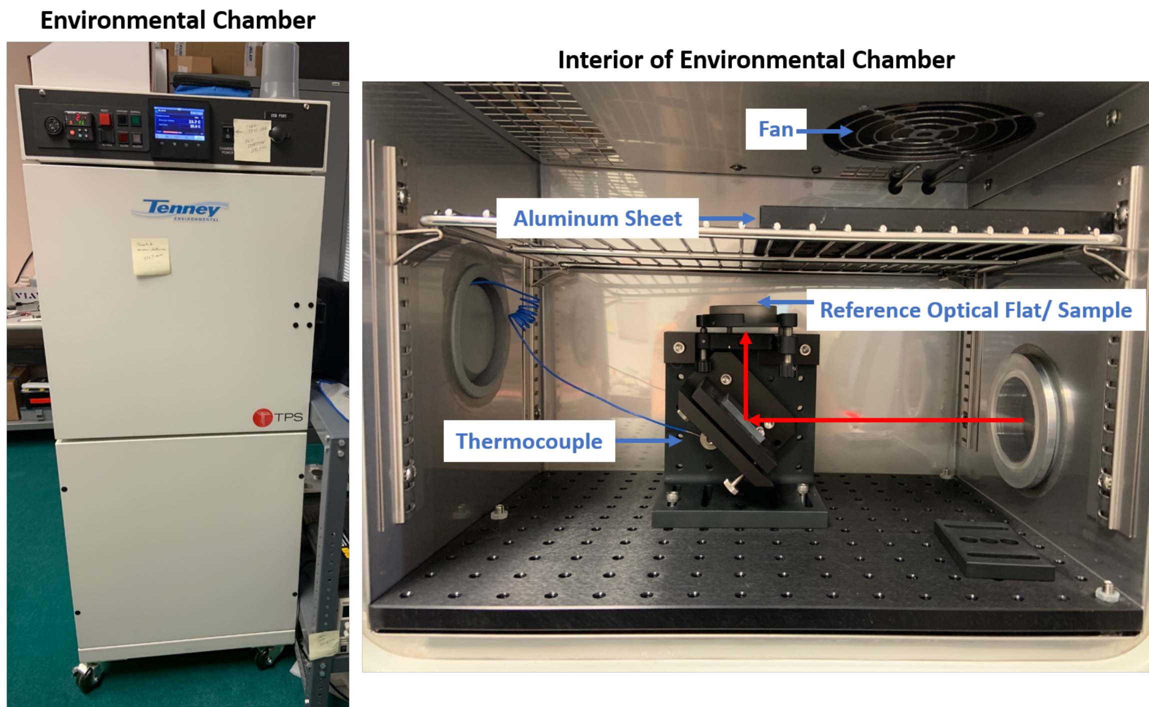

Figure 5.2: Images of the exterior (left) and interior (right) of the environmental chamber.

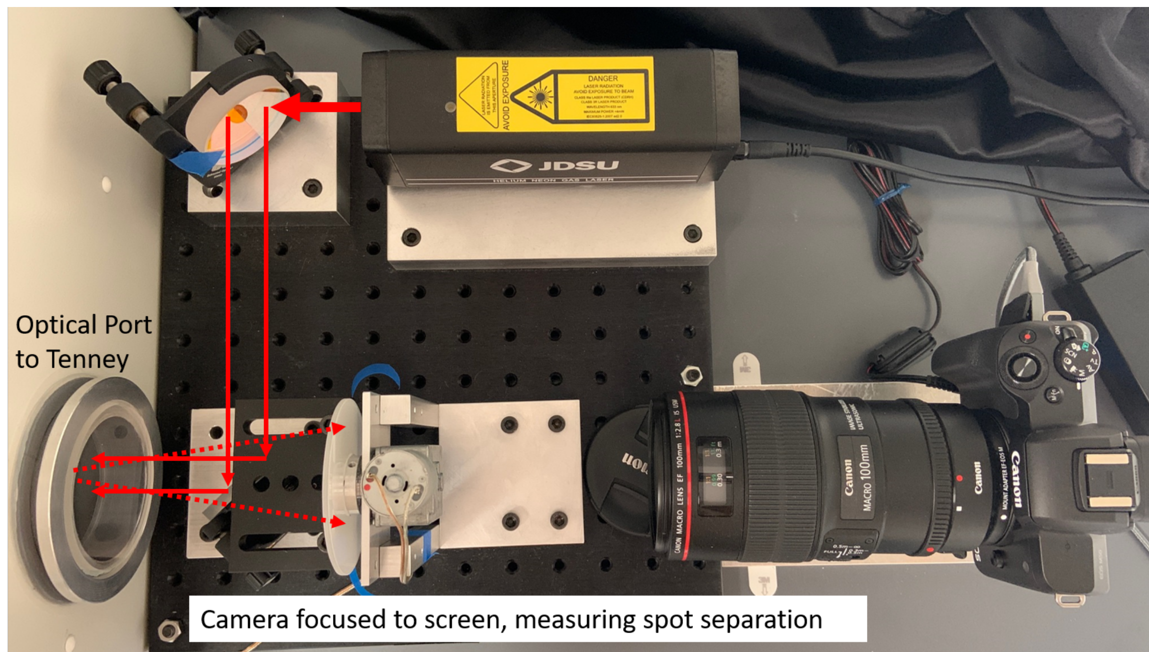

Figure 5.3: An image of the exterior optics that are used in conjunction with the environmental chamber to measure the thermal stress of the samples.

The determination of the separation of the laser beams after reflection from the sample is made by analyzing the raw image data from the camera. The image data from the camera presents a distribution of pixel intensity. Since the laser is operating in the Gaussian mode, and the laser speckle is removed by the rotating screen, the pixel intensity distribution is remarkably Gaussian for both laser spots. A program designed Bill Southwell and written by Joseph Peeples of Table Mountain Optics is used to analyze the camera data and find the pixel location of the two spots. The reported data from this program is the pixel separation of the two spots, and is accurate to sub-pixel resolution. The camera pixel size is approximately 3 μm, so this method of measuring the separation of the two laser spots, reflected off the substrate is very precise.

The pixel separation of the two laser spots on the camera focal plane can be converted to a sample curvature by using the principles of the focal length of a curved mirror. The pixel separation of the two beams, upon reflection off an optical flat is used as the reference for zero sample curvature. This reference is taken before and after each measurement. The pixel separation on the camera focal plane after reflection off the sample is then compared to the separation from the optical flat. By knowing the distance from the sample plane to the camera focus, the curvature of the sample can be characterized. The relationship between the measured pixel separation and the curvature is described in Eqn. 5.1, where the curvature calculated here has the units of m^{-1} or Curvature Diopters, and the variable D is the distance (in meters) between the sample and the camera focal plane.

$$C_v = \frac{1}{2D}\left(\frac{\text{Sample Pixel Separation}}{\text{Reference Flat Pixel Separation}} - 1\right) \tag{5.1}$$

It should be noted that the substrate-film system may deviate somewhat from a perfect sphere, which is the theoretical model that is being used to convert the spot separation into substrate curvature. Any imperfections in the substrate may cause some small warping which can result in a calculated spot separation which is dependent on the location on the wafer. However, the thermal stress can still be obtained by probing a single spot and observing the change in spot separation with temperature. This effect is dependent on the differential thermo-mechanical properties of the substrate and the film, and will be independent of the initial system curvature.

5.1.2 Temperature Cycling Profile

The temperature range that was measured for these samples was from 0-100°C, using the Tenney Environmental Chamber. A temperature cycling profile can be programmed on the chamber, and a variety of different temperature profiles between the temperature extremes were investigated.

The temperature profile that was originally used for these samples followed the profile used for another program. It started at room temperature, increased to 100°C in 25°C increments, decreased to 0°C in 25°C increments, and then returned to room temperature in 25°C increments. At each temperature set-point, the sample would soak for one hour, resulting in a 9-hour test.

An example of the data collected during this 9 hour test is shown in Figure 5.4. The raw data collected are the images from the camera, which record the two laser spots. These are then processed, using the SpotFitter program from Table Mountain Optics to find the spot separation by fitting the laser spots to Gaussian distributions. Plotted in blue on the left axis in Figure 5.4 is the calculated spot separation from the camera images. During the

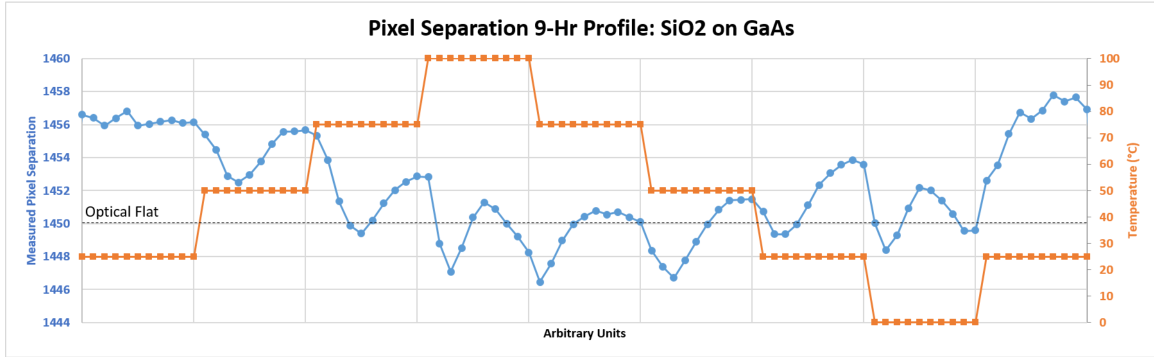

Figure 5.4: Example of raw data for 9-Hr temperature cycling profile. Pixel separation shown in blue, temperature set-point shown in orange, reference optical flat shown by the dashed line.

test, the camera takes an image every six minutes, and the timer on the camera is synced with the timer on the environmental chamber to within a few seconds. This gives 10 data points every hour, and results in 10 data points for every set-point temperature.

Since it will take the environmental chamber and the sample some time to stabilize in temperature, not all 10 data points are utilized for each set-point temperature. Instead, the last 5 data points (30 minutes) are averaged in order to obtain the sample curvature at a given temperature. For this to be high-quality data, the curvature of the sample needs to be stable over at least a 30 minute period.

Scrutinizing the spot separation data in Figure 5.4, it is evident that this stable curvature criteria has not been met. However, due to the shape of the curves toward the end of each temperature set-point, it appears as if the curvature is about to reach a stable range. In response to this hypothesis, the temperature profile was extended to a 2-hour soak for each temperature set-point.

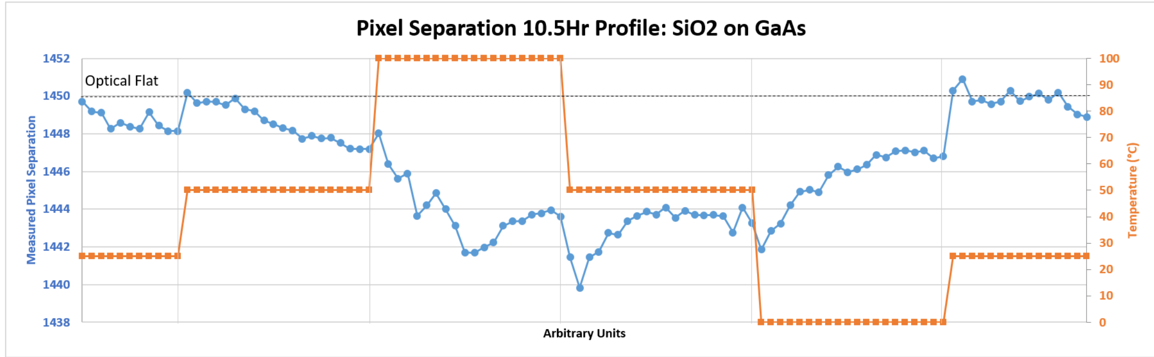

Figure 5.5: Example of raw data for 10.5Hr temperature cycling profile. Pixel separation shown in blue, temperature set-point shown in orange, reference optical flat shown by the dashed line.

Due to the allotted time available for use of the instrument, the temperature cycling profile was kept to under 12 hours so that two samples could be measured in one day. With this limitation, the temperature cycling profile was modified to a 10.5 hour test, shown in Figure 5.5.

For the 10.5 hour test, the sample is held at room temperature for 1Hr, followed by 2 hour at temperatures 50°C, 100°C, 50°C again, 0°C, followed by 1.5 hour at room temperature. As shown in Figure 5.5, the longer soak time resulted in a stabilization of sample curvature.

Based on the sharp change in curvature at the beginning of a temperature set-point change in the 9Hr test, it was hypothesized that the fan inside the chamber, which blows directly down onto the sample (as shown in Figure 5.2), was affecting the temperature change and stabilization of the sample. In addition to the change to the 10.5Hr test, an aluminum sheet was placed below the fan to block some of the direct airflow from the fan onto the sample (shown in Figure 5.2). The two modifications combined show a region of stable curvature for each temperature set-point.

Figure 5.5 shows the pixel separation data for a single sample: SiO_2 on a GaAs substrate. This same data collection was done for all 14 samples, using the 10.5 hour temperature cycling test. The reference optical flat was measured at the beginning and end of each data set.

5.1.3 Thermal Stress Calculation from Measured Data

In order to convert the collected pixel separation data into a thermal stress curve, the last five data points from the temperature set-point (the data from the last 30 minutes of the soak) are averaged to calculated a pixel separation/curvature at that temperature. It is then possible to plot both pixel separation and sample curvature as a function of temperature, as shown in Figure 5.6 for SiO_2 on a GaAs substrate.

Plotting both the pixel separation and the curvature calculations are useful for different reasons. Plots of the pixel separation versus temperature give an idea of how close the collected data is to the noise floor of the instrument, while curvature versus temperature data gives a more tangible metric.

For Figure 5.6, the top graph shows the pixel separation versus temperature. The range of the graph's y-axis for this plot is only 10 pixels, which indicates that this measurement could be influenced easily by noise as the measurement range is small. It is likely the variation in this graph is not a hysteresis effect, but mostly influenced by instrument noise, given the small pixel range.

The bottom graph shows curvature versus temperature. Here intuition can be gleaned from the data, as curvature can be compared directly to other tangible metrics. It is worthy of note here that all of the measured curvatures are negative, indicating that the film is in

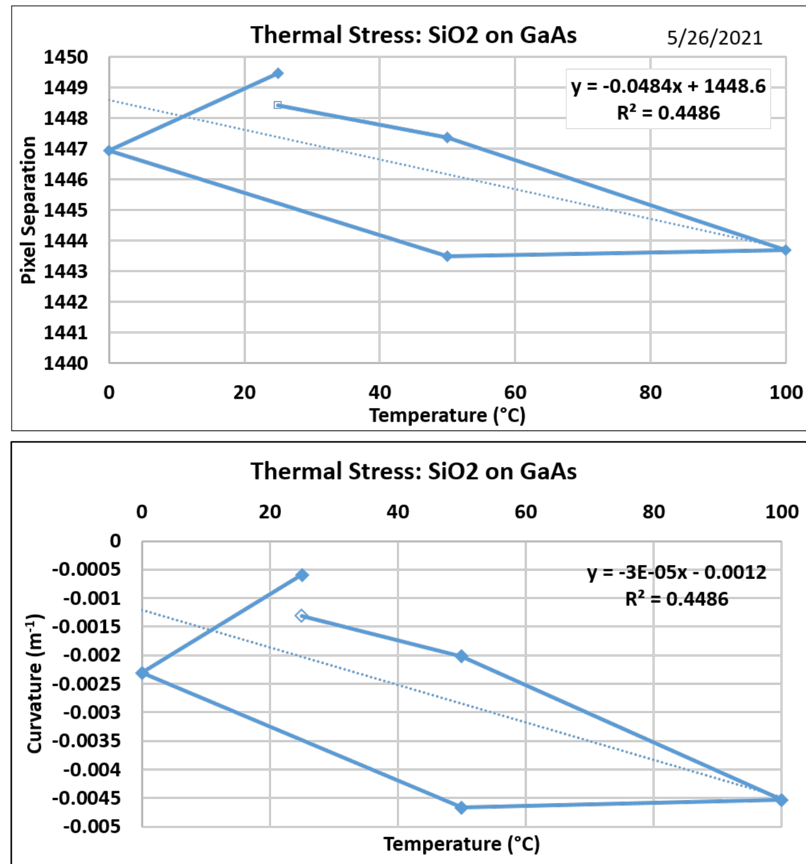

Figure 5.6: Thermal stress fits from measured data of SiO_2 on GaAs substrate. Top graph uses collected data and displays pixel separation versus temperature. Bottom graph converts the pixel separation into calculated curvature versus temperature.

compression for all measured temperatures. Additionally, the magnitude of the curvature is very small.

Curvature, when reported in Curvature Diopters (1/m) can be used to gain intuition about the system. For instance, curvature diopters and power diopters are conceptually related. Curvature diopters indicate the curvature of a mirror, which will have a focal point at half the radius of curvature, leading to a direct relationship between the surface curvature and the magnification power. Optometrists will typically prescribe lenses to patients in steps of 0.25 power diopters. Those who wear prescription eye-wear will have a sense that the magnitude of 0.25 power diopters is small, and may be able to imagine the curvature of a surface that would give that focal length. In Figure 5.6, the maximum curvature of the sample is -0.005 curvature diopters, indicating that the sample is very flat. For the data analysis, the pixel separation data will be used as it is the quantity that is measured, and can be directly investigated for sources of noise or uncertainty. The accompanying curvature plots are a reference to give a sense of scale to the reader.

Another observation from this data is that the slope of the best-fit line is negative. This indicates that the curvature becomes more concave with increasing temperature. As demonstrated in Figure 4.2, when the substrate expands more than the film with increasing temperature, the sample (measured from the film side) will become increasingly concave. This is consistent with predictions of the system shown in Figure 5.6, as the CTE of bulk Fused Silica is 0.55 ppm/°C [51], and the CTE of GaAs is 5.73 ppm/°C [52].

A last key observation from Figure 5.6 is that the R^2 value is low (0.4486), indicating that the quality of the fit is in question. Since the fit of this curve is used, and it has been shown in Section 4.3.1 that the calculation of CTE and Young's Modulus are sensitive to

the slope and its errors, it is important to fully characterize the uncertainty in the slope fit for each thermal stress measurement set.

These data were analyzed in Microsoft Excel, which can report a linear best-fit slope, along with its standard error, given any set of data. The reported standard error is used in order to characterize the uncertainty of the linear fit. For the sample shown in Figure 5.6, the reported standard error in the slope of the pixel separation versus temperature is 0.0268, leading to a calculated slope of -0.0484 ± 0.0268. This is a high uncertainty, and must be further explored to determine if this is anomalous data or holds some further information about the samples and the measurement system.

These same measurements and analyses were completed for all 14 samples. These measured slopes and their associated errors are plotted in Figure 5.7, and shown in table format in Table 5.1.

These data are worthy of some discussion. Figure 5.7 shows all of the pertinent information on the linear fits for the slopes of pixel separation versus temperature. On the left is the data for the films on Si substrates, on the right is the data for films on GaAs substrates. The top line shows each point as the best-fit slope, and the error bars are the values for the standard error in the slope. A linear trend-line has been superimposed on the graph to underscore the trends in the data. The bottom line shows the associated R^2 value for each data point.

Focusing first on the films on silicon substrates, shown on the left side of Figure 5.7, there is a trend of decreasing slope with increasing SiO_2 content, which crosses the x-axis with zero slope at some composition around 55% SiO_2. This finding is consistent with the current understanding of the material system. The CTE of single-crystal Si substrates is

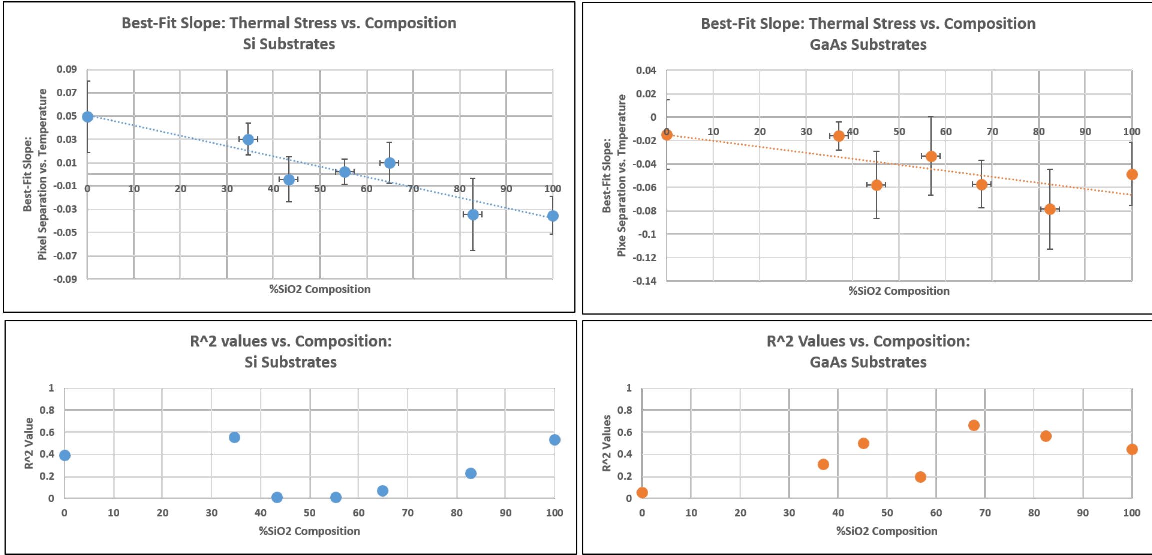

Figure 5.7: The measured slopes and their associated errors plotted as a function of %SiO2 film composition. The top two plots show the measured slope, error bars demonstrating the standard error. On the left are the films on Si substrates, on the right are the films on GaAs substrates. The bottom two plots show the R^2 values of the linear best-fit slopes.

Table 5.1: The best-fit slope for thermal stress measurements, its error and its R^2 values for each measured sample.

Si Substrates			
Target Powers	Slope (Pixels/°C)	Slope Error (Pixels/°C)	R^2
0WTa, 200WSi	-0.0352	0.0164	0.5371
30WTa, 200WSi	-0.0343	0.0311	0.2327
50WTa, 200WSi	0.0098	0.0175	0.0733
65WTa, 200WSi	0.0023	0.0110	0.0108
80WTa, 200WSi	-0.0043	0.0192	0.0121
95WTa, 200WSi	0.0303	0.0136	0.5553
95WTa, 0WSi	0.0496	0.0307	0.3943
GaAs Substrates			
Target Powers	Slope (Pixels/°C)	Slope Error (Pixels/°C)	R^2
0WTa, 200WSi	-0.0484	0.0268	0.4486
30WTa, 200WSi	-0.0786	0.0342	0.5684
50WTa, 200WSi	-0.0571	0.0202	0.6671
65WTa, 200WSi	-0.0332	0.0336	0.1958
80WTa, 200WSi	-0.0576	0.0287	0.5012
95WTa, 200WSi	-0.0160	0.0119	0.3116
95WTa, 0WSi	-0.0147	0.0298	0.0574

reported to be 2.6 ppm/°C [53, 54], the CTE of Fused Silica is reported to be 0.55 ppm/°C [51], and the CTE of Ta_2O_5 is reported to be between 4.4-6.8 ppm/°C [11, 55]. Recall from Figure 4.2 that when the CTE of the substrate is larger than the CTE of the film, the film will bend more concave with increasing temperature when measured from the film side. With the curvature sign-convention used in this study, a negative slope is consistent with a system where the substrate CTE is greater than the film CTE. Therefore, the slopes of the films with higher SiO_2 composition indicate that the film CTE is less than that of the substrate (2.6 ppm/°C), while those films with higher Ta_2O_5 contents indicate that the film CTE is higher than the substrate. There will then be some film composition at which the CTE of the substrate and the film match exactly resulting in no change in curvature with temperature. Another observation from this data set is that the R^2 values for the slope values which are close to zero are also very small, reinforcing the idea that the best-fit slope is nearly zero and fitting to noise.

Shifting focus to the films grown on GaAs substrates, a similar analysis can be done. The reported CTE of GaAs is 5.73 ppm/°C [52]. Since all of the best-fit slopes are negative, this indicates that all of the film compositions have a CTE smaller than that of the substrate, which is consistent with the understanding of the properties of the single-material films.

A similar observation regarding the R^2 values for the films on GaAs substrates can be made. The R^2 value decreases as the best-fit slope decreases.

Lastly, it is important to note that the standard errors for these slopes are quite large, given that the calculations for CTE and Young's Modulus are sensitive to these values. It is valuable information from the measurements of these samples that the trends in the

best-fit slopes are consistent with intuition about these film-substrate systems. However, an exploration of the source of these uncertainties will be further discussed.

5.1.4 Evaluation of Instrument Noise

One exploration that was done in response to the high uncertainty in the best-fit slope data is to evaluate the noise level of the instrument. The definition of noise for this application will be the variation in measured spot separation from reflection off the reference optical flat. Other factors such as variation in temperature across the sample, or drift in the instrument over time can also contribute to added uncertainty in the measurements, but may be accounted for and corrected through modification of the data collection protocols or through data-analysis techniques. The variation in the measurement of the optical flat is indicative of the base-level noise in the system.

In order to characterize this noise threshold, the optical flat was placed in the sample holder and the spot separation was measured 25 times at room temperature, removing and replacing the optical flat between each measurement. The measured spot separation of these two beams, reflected from the optical flat had a variation of 1.9 pixels. This translates into a sensitivity in curvature of 0.0013 Curvature Diopters (1/m), which is a high instrument sensitivity.

This noise threshold only comes into play when attempting to measure curvatures and slopes that are close to zero. As shown in Figure 5.8, a slope that is 0.038 pixels/°C will be indistinguishable from a slope of zero for a temperature range of 100°C.

With this in mind, an analysis of the data presented in Table 5.1 can be done to determine if the measured slopes are larger than this noise threshold. This analysis is shown

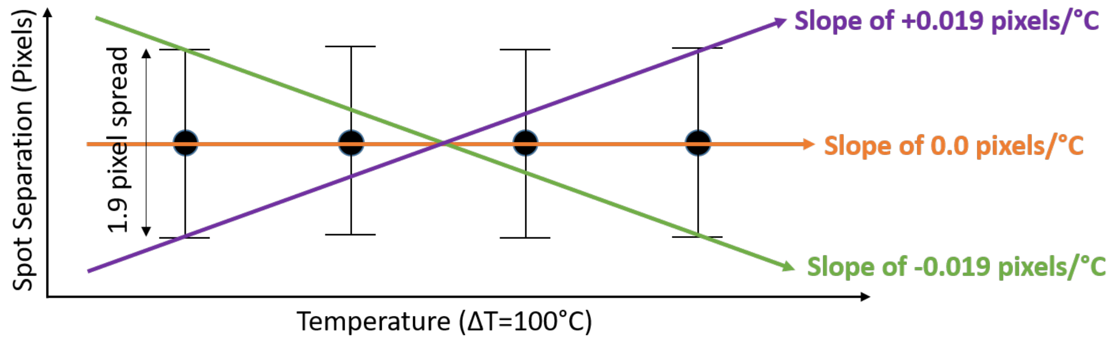

Figure 5.8: A diagram of the range of acceptable reported slopes with a variation of 1.9 pixels of noise.

in Figure 5.9, demonstrating that almost all of the measured points (or their uncertainty bars) fall within this instrument noise range.

It is worth reiterating at this point that the instrument noise is in fact, very low, with a sensitivity of 0.0013 Curvature Diopters (1/m). However, the curvature change with temperature for these samples is also very small, leading to the conclusion that the effect must be enhanced for future samples in order to calculate the thermo-mechanical properties of these films with high precision. An exploration of how this can be achieved will be explored through an instrument sensitivity analysis.

5.2 Sensitivity Analysis: Methods to Increase the Signal-to-Noise Ratio

The noise level of the instrument has been fully characterized, and determined to be low. However, the signal from the thermal stress measurements of these samples is low enough that most of the measurements fall at or below the noise threshold. This explains the high-uncertainty in the measured values of the slope for curvature as a function of temperature. For follow-on studies which use these measurement techniques, it will be

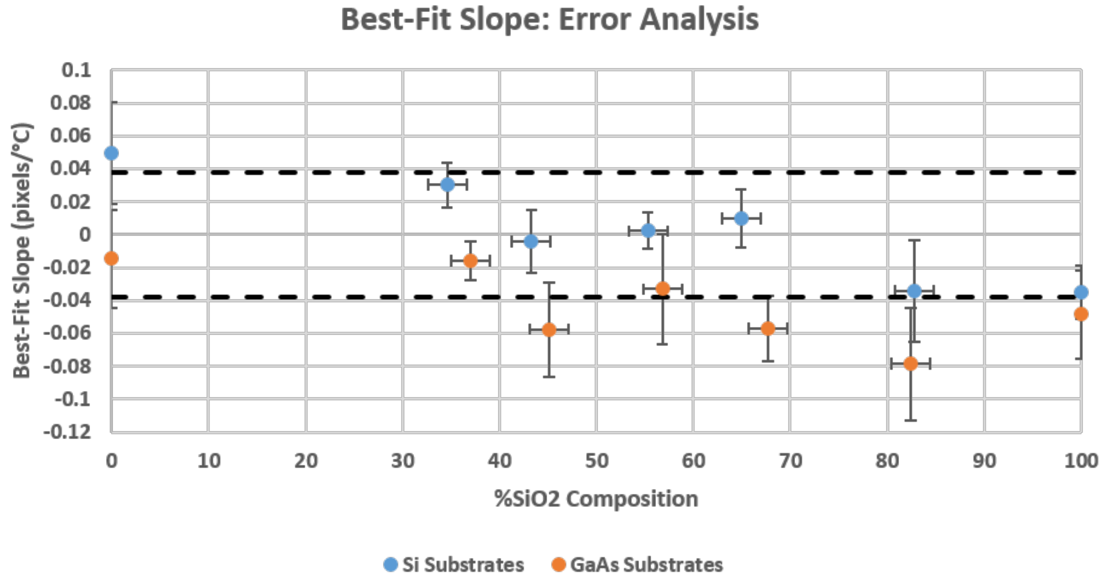

Figure 5.9: The measured slopes and their associated errors, shown in conjunction with the calculated instrument noise threshold, shown as the dashed lines.

useful to understand the factors that contribute to the measured slope, and the sensitivity of the measurements to those factors. This will build the tools for future experiments to be designed with the instrument limitations in mind, and be designed according to the principles discussed in this work.

The limitation in the sensitivity of the thermal stress measurement instrument comes from the spread in measurements of spot separation from repeated measurements of the same sample. As discussed above, this case was done for an optical flat, demonstrating the noise threshold of the instrument. This limitation comes from an analysis of the pixel separation of the two spots on the camera focal plane array. Therefore, it can be useful to describe the thermal stress calculation in terms of the pixel separation. This is a straightforward calculation by combining Eqns. 4.16 and 5.1 to express the factors which affect the pixel separation. The resultant is Eqn. 5.2, where p is the sample pixel separation, D is the

distance between the sample and the focal plane, ref is the reference flat pixel separation, and E' refers to the biaxial modulus.

$$\Delta p = \pm 12D(ref)(CTE_s - CTE_f)\left(\frac{E'_f}{E'_s}\right)\left(\frac{t_f}{t_s^2}\right)\Delta T \tag{5.2}$$

This makes it possible to see the factors that will increase the signal-to-noise ratio for future experiments that will use the same instrument. With the limit in the sensitivity being the variation is pixel separation, there are a variety of options that can be made to increase the signal to be well above that threshold of 3.8 pixels for measurements of thermal stress.

From Eqn. 5.2, it is a straight-forward argument that decreasing the substrate thickness will most accentuate the change in curvature for a given material system, as this is the only term that is squared in the expression. Additionally, there are other methods which will increase the signal (Δp): increasing the film thickness, increasing the measurement temperature range, and changing the substrate material to maximize the difference in CTE and the biaxial modulus ratio.

There are a number of different ways in which to analyze this sensitivity. For the purposes of being the most practical for this research group, what follows will be an in-depth discussion of determination of the best film thickness to grow, given the substrates available. It would be straightforward also to analyze instead, the thickness or material choice of the substrate if a specific film thickness was desired. However, there are a variety of practical purposes which might make variation of the substrate material and thickness challenging, cost and availability being some of the most likely, whereas there exists the capability to grown films of different thicknesses.

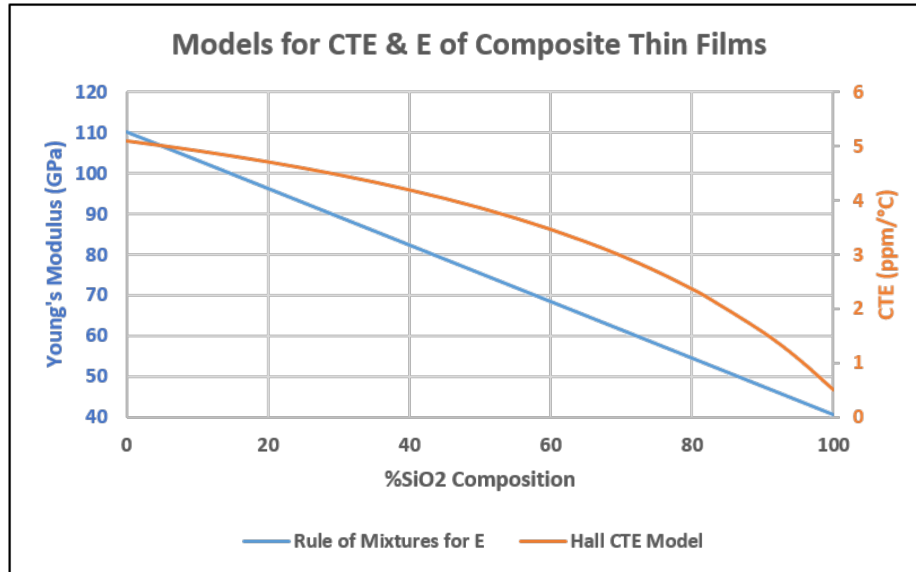

Figure 5.10: Plots for the "Rule of Mixtures" model for the Young's Modulus of the composite thin films, and the "Hall CTE Model" for the CTE of the composite thin films.

Using Eqn. 5.2, it is straightforward to plot the film thicknesses needed in order to measure a pixel separation slope that is at the noise threshold of the instrument. This can be done to compare the film thicknesses grown for this project with the film thicknesses that can be grown in the future to measure this effect with more precision.

In order to determine the film thickness required to be at the noise threshold of the instrument for these mixed-oxide films, a model must be applied to estimate both the CTE and the Young's modulus of the films. It is not required to know these values precisely in advance, however it is helpful to have an estimate which will guide a choice of film thickness.

There is a commonly accepted model for the estimation of the Young's Modulus of composite materials known as the "Rule of Mixtures" [56]. This model states that the modulus of a composite can be approximated as the volume-fraction-weighted sum of the two constituent materials. This is written explicitly in Eqn. 5.3, where E_{comp} is the modulus

of the composite material, $E_{a,b}$ is the modulus of the constituent materials, and $V_{a,b}$ is the volume fractions of the constituent materials such that $V_a + V_b = 1$.

$$E_{comp} = V_a E_a + V_b E_b \tag{5.3}$$

At the point of this publication, it is the belief of the author that there exists no model published in the open literature which can be applied for estimation of the CTE of a composite thin film. However, Randy Hall of Conejo Valley Research has developed a model which has shown to be effective at estimating the effective CTE of multi-layer thin film stacks based on an adjusted, weighted volume fraction equation [6]. This model will be applied in this work as a way to estimate the CTE of composite mixed-oxide thin films, and will be referred to as the “Hall CTE Model”. This model is expressed in Eqn. 5.4, where CTE_{comp} is the CTE of the composite material, and $CTE_{a,b}$ is the CTE of the constituent materials.

$$CTE_{comp} = \frac{V_a CTE_a E_a + V_b CTE_b E_b}{(V_a E_a + V_b E_b)} \tag{5.4}$$

The “Rule of Mixtures” can be applied to the estimate the Young’s Modulus of the composite thin films, and the “Hall CTE Model” can be applied to estimate the CTE of the composite thin films. These two models applied to the SiO_2-Ta_2O_5 composite thin films grown for this study is shown in Figure 5.10. Notice that the “Rule of Mixtures” Model predicts a linear function for the Young’s Modulus as a function of composition, where the “Hall CTE Model” predicts that the CTE of the composite films will vary non-linearly with composition.

Using these two models, in conjunction with the known properties and thicknesses of the two substrates (Si and GaAs), the required film thicknesses can be plotted for each film composition. This estimate for sets of films on 270um thick Si substrates and 315um thick GaAs substrates is shown in Figure 5.11.

This figure contains come valuable insights into both the instrument system and the theory of thermal stress. First, the blue curves in the figure indicate the film thicknesses that would be required in order for the measured curvature to be equal to the noise threshold of the instrument, given the substrate material and properties indicated in the graph title. These thicknesses are plotted versus the composition of the film, with pure Ta_2O_5 on the left and pure SiO_2 on the right. As mentioned previously, the required film thicknesses can be decreased if deposited onto thinner substrates.

The orange curves indicate the difference between the CTE of the substrate and that of the film, predicted by the Hall CTE Model. As anticipated from the best-fit slope data shown in Figure 5.7, there is a composition which will match the CTE of the Si substrate exactly. The location of this match, which appears as the minimum in Figure 5.11 is determined by the CTE's of the two endpoint materials. Notice that as the CTE contrast approaches zero, the required film thickness approaches infinity. This simply indicates that if there is no CTE contrast, there will be no bending of the substrate with temperature. This means that there will be no thickness of film which will achieve a bending with temperature that exceeds the noise of the instrument, as the composition approaches that contrast minimum. In practice, if the bending of the substrate with temperature is in the noise of the instrument, the user has increasing confidence that the CTE contrast is small as the film thickness increases. Put another way, a thick film which shows very little change in

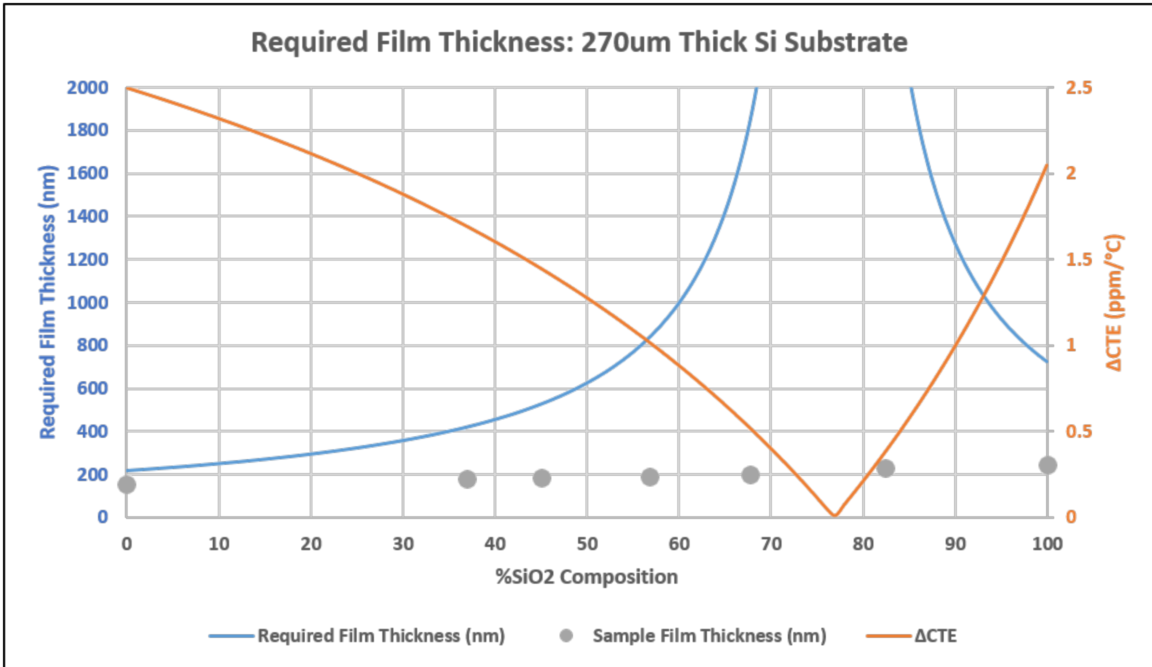

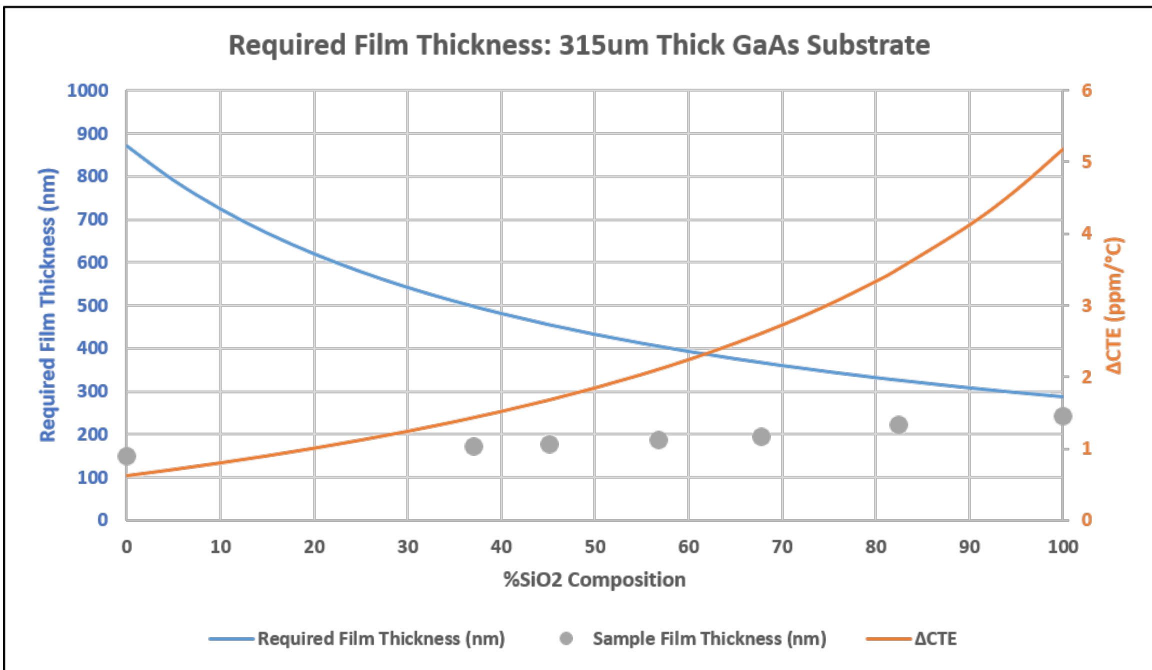

Figure 5.11: Required film thickness to be equal to the noise threshold of the instrument, for SiO_2-Ta_2O_5 composite films on 270um thick Si substrates (above), and 315um thick GaAs substrate (below). The orange line indicates the CTE contrast between the film and the substrate. The grey dots indicate the fabricated film thicknesses for this study.

curvature with temperature is likely indicating that the CTE of the film matches that of the substrate, creating an "athermal" coating.

Lastly, the grey dots in Figure 5.11 indicate the film thicknesses that were fabricated. Notice that each of the film thicknesses are below the estimated required threshold. This observation is consistent with the findings from Figure 5.9 which indicates that measured slopes are below the noise threshold of the instrument.

It is worth pausing here to compare this model against measurements made under other programs in order to give this model some validity.

5.2.1 Evidence in Support of the Sensitivity Model

The thermal stress measurement instrument described in this work was designed and built by Conejo Valley Research in support of an effort for the Air Force Research Laboratory, which was completed and documented in [6]. The instrument proved, with great success, its ability to measure the thermal stress in thin films similar to the ones fabricated under this study. This is part of the reason why the instrument was chosen for the measurement of the films for this study.

However, a great deal of the films measured during the course of this contract were thicker than the films fabricated for this study. With the proposal of this sensitivity model as an explanation for the high uncertainty in the measurements of the films fabricated for this study, it is useful to compare the uncertainty from measurements of thicker SiO_2 and Ta_2O_5 films, measured using this same instrument.

The hypothesis postulated in this work is that there is an instrument noise threshold in the range of 0.038 pixels/°C for the instrument measurement of curvature versus tempera-

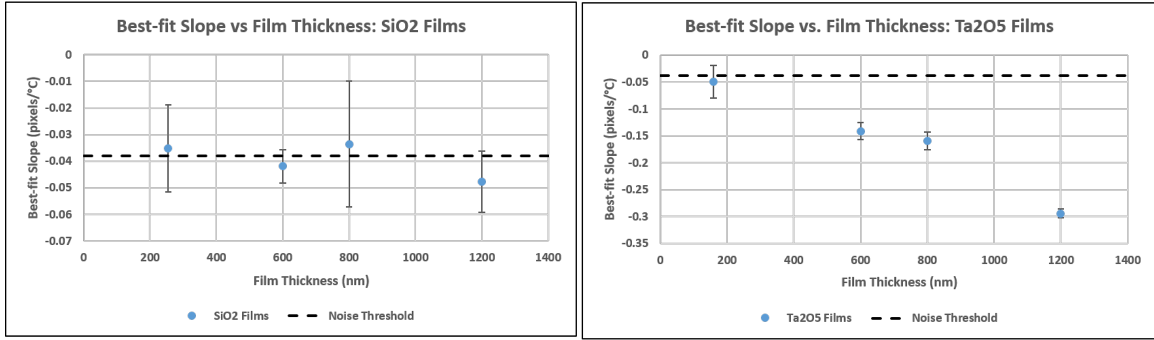

Figure 5.12: Plots of Best-fit slopes and associated error for SiO_2 and Ta_2O_5 films of different thicknesses grown under both this program as well as [6].

ture. This slope is influenced, in part by the CTE contrast between the film and substrate, and also influenced by the ratio of film thickness to substrate thickness, and the ratio of the film and substrate moduli.

Using measurements of SiO_2 and Ta_2O_5 films from this program [6], it is possible to compare films of different thicknesses (on Si substrates of roughly the same thickness as were used during this work). This can allow for an evaluation of the measured slope and its error to see how the error changes as a function of measured slope, and how the slope changes as a function of film thickness. This analysis is shown in Figure 5.12, and also includes the data points from films grown during this study.

Figure 5.12 shows the best-fit slope from the curvature versus temperature data, where the error bars on each data point represent the reported standard error of the slope. These data are plotted as a function of film thickness. This is then compared to the calculated noise threshold of the instrument, shown as a horizontal dashed line. Notice that all of the slopes are a negative value, meaning that slopes which have larger magnitude than the noise threshold are below the line.

The plots for the SiO_2 films show a very small change in the best-fit slope with thickness. For this material, there are only two points which measure a slope greater than the noise threshold, even for film thicknesses out to 1200nm. These two factors may indicate that the CTE contrast between the film and substrate may be less than what is estimated for the films made in this study. However, notice that the errors for the measurements with slopes greater than the noise threshold are significantly lower than those below this threshold.

The plots for the Ta_2O_5 films show a large variation in slope with film thickness, where the slope with temperature is just above the threshold for the thinner film fabricated in this study. As predicted in Figure 5.11, the Ta_2O_5 film on Si substrate is nearly thick enough to provide a force on the substrate with temperature to measure a slope above the noise threshold. Figure 5.12 confirms that the film is indeed just at this threshold. The other three thicknesses of Ta_2O_5 films provide a much larger slope, and indeed indicate a smaller error with slopes of increasing magnitude.

These two plots indicate that the model proposed in this paper is reasonable, and that the calculated instrument noise threshold is a reasonable estimate of the instrument noise.

5.3 Two-Substrate Method: Calculation of CTE & Young's Modulus

The measurements of curvature versus temperature discussed in Section 5.1.3 can be used, along with their associated uncertainties to calculate the CTE and Young's Modulus simultaneously using the Two-Substrate method described in Section 4.3.1, where Eqn. 4.18 outlines the manner in which the curvature versus temperature data from the measurements of the two films affects the calculation of both the CTE and the Young's Modulus.

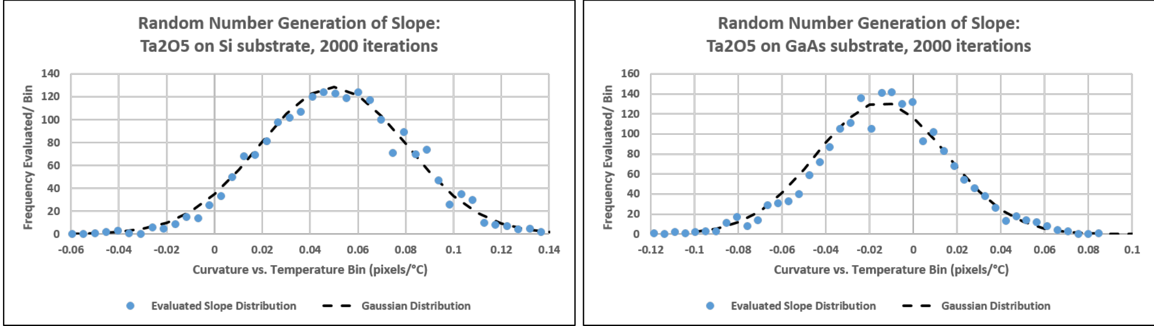

Figure 5.13: A histogram of he 2000 generated random numbers, with normal distribution centered around the best-fit slope, with a standard deviation equal to the standard error in the fit. The dashed lines represent a normal distribution with the properties outlined.

For this two-substrate method, there are two sources of measurement uncertainty which must be considered here. Each best-fit slope will together contribute to the uncertainty of the calculated values of the CTE and Young's Modulus. The general outline of how this is done is described in Section 4.3.3, however in this section an example of the process will be outlined, using the Ta_2O_5 films on GaAs and Si substrates.

The uncertainty from two measurements sources is incorporated into the calculations through the use of a random number generator. A random number is generated for each slope, where the generation is weighted by a normal distribution centered around the measured best-fit slope and with a standard deviation equal to the standard error of the slope fit. An example of this is shown in the form of histograms in Figure 5.13 where 2000 iterations were generated. This figure demonstrates the frequency at which each random number is generated, showing agreement with the normal distribution function. This weighted random number generator can be used to generate inputs for the values of the curvature versus temperature slopes.

Using this weighted random number generator for each slope input into Eqn. 4.18, the CTE and Young's modulus can then be evaluated 2000 times to form a distribution of calculated results. This normal distribution for the CTE and modulus each have an average and a standard deviation. The average of these distributions is reported as the calculated CTE, while the standard deviation of this distribution is reported as the uncertainty in the calculation.

The results of these calculations are shown in Figure 5.14, where the upper plot shows the results of these calculations at full scale to show the extent of the error bars, while the lower plot reduces the bounds to highlight the calculated values in the area of interest. Each data point represents the calculated average of the distribution of 2000 CTE calculations using the random number generator described above. The error bars represent the width of the distribution in the 2000 calculated values of the CTE.

While some of the uncertainty in these calculations using the two-substrate method can be orders of magnitude different, as shown in the upper graph in Figure 5.14, the lower graph demonstrates that the uncertainty in the calculations exceed the sensitivity needed to distinguish the effect that is being measured. This demonstrates one of the weaknesses of this two-substrate method: that any uncertainty present in the measurements is expounded in the calculation due to the necessity of incorporating two uncertainties in a single calculation.

The bottom line here is that the film thicknesses are too small to induce curvature change in the substrate which exceeds the instrument noise threshold. For these samples, in order to tease out any quality CTE information from these thermal stress measurements, it is imperative to reduce the uncertainty in the measurements. This can still be done with

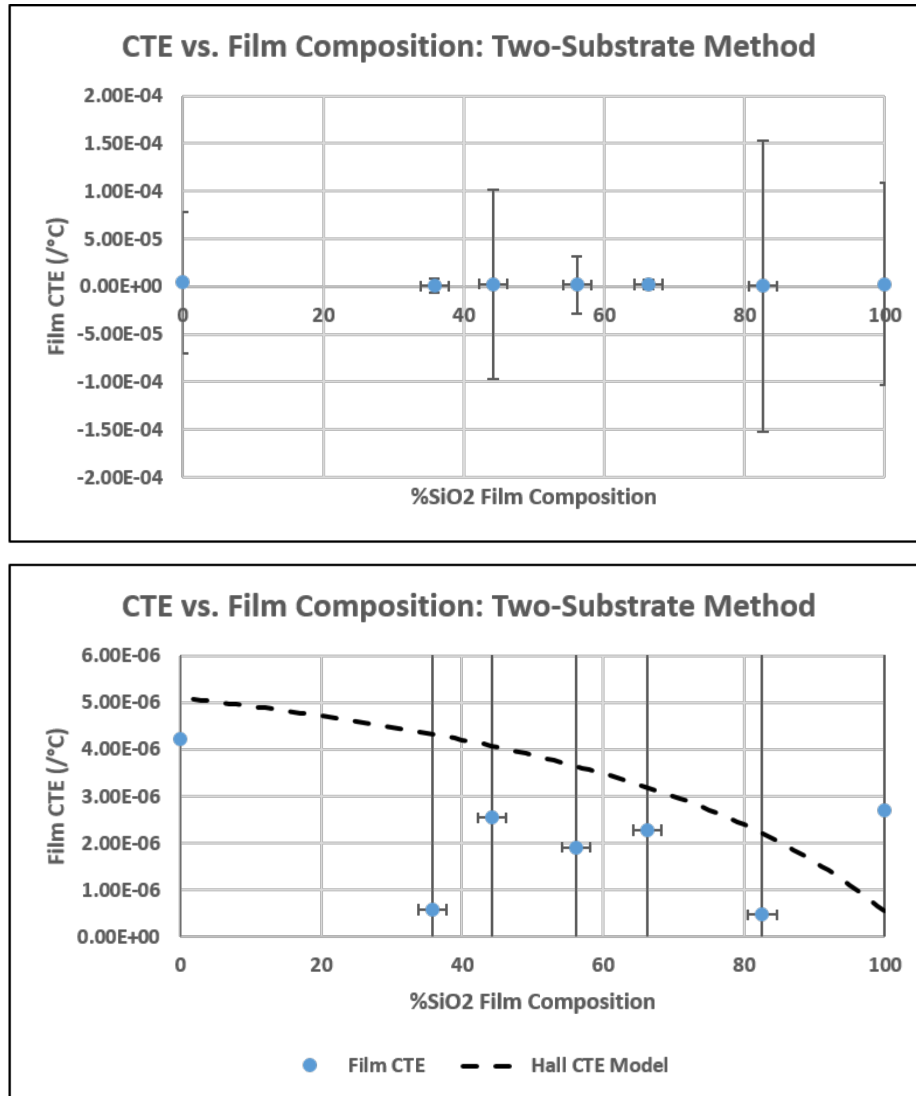

Figure 5.14: Calculated CTE vs. film composition using the two-substrate method. The top graph and the bottom graph hold the same data, but have different y-axis scales to highlight the uncertainty (top) and the calculated values (bottom). The dashed line represents the Hall CTE Model.

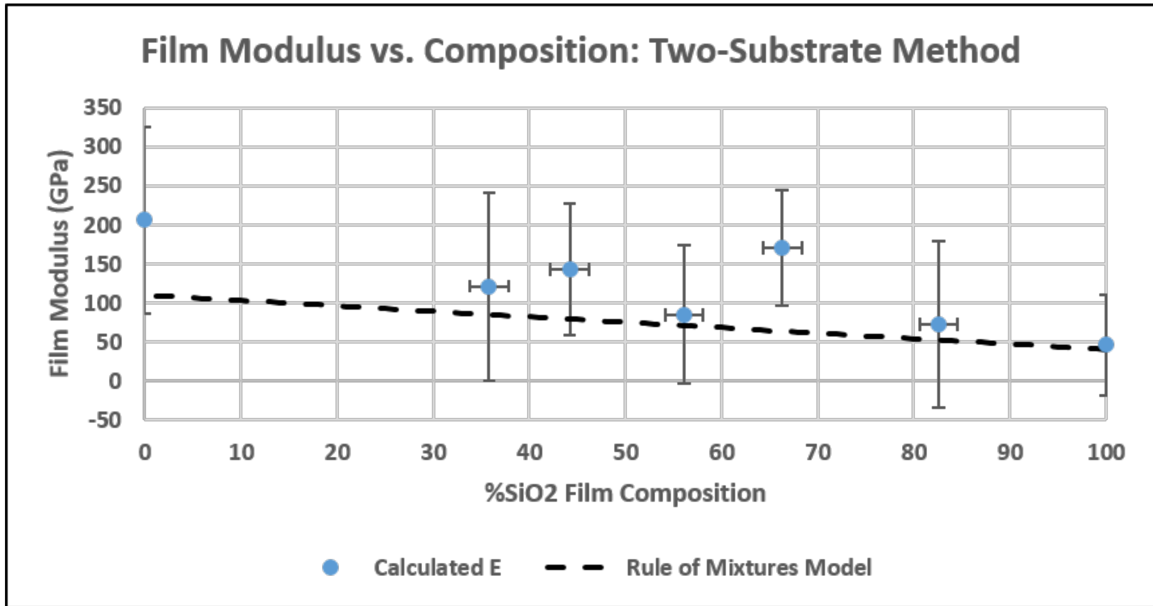

Figure 5.15: Calculated Young's Modulus using the Two-Substrate method.

the equipment available, using the same samples that were fabricated for this study. The improvement here is to measure the Young's Modulus directly, and to calculate the film CTE using the Single-substrate method. For these direct Young's Modulus measurements, the uncertainties are much lower, meaning that the total uncertainty in the calculated values will be lower.

The two-substrate method allows for the simultaneous calculation of the CTE and Young's Modulus from the same measurements. The Young's Modulus calculations are also done using Eqn. 4.18. Similarly to the CTE calculations, this uses as inputs for the curvature versus temperature, the same random number generator described above. Again, 2000 iterations of the modulus are calculated, the average of which is reported as the calculated modulus and the standard deviation of which is reported as the uncertainty in the measurement. These calculated data are shown in Figure 5.15.

It is noteworthy that the uncertainty in the Young's Modulus values are significantly lower than the uncertainty for the CTE calculations. While still high uncertainty, a trend can be observed, demonstrating a decreasing modulus with increasing SiO_2 composition. This trend is consistent with the expectations for these materials. The "Rule of Mixtures" model is plotted against the calculated data in Figure 5.15, which lies below all of the calculated data points, however almost all of the uncertainty bars from the calculated Modulus values fall in line with the model. This indicates that the anticipated values of the modulus endpoints are lower than the values predicted by these calculations.

In order to decrease the uncertainty in these calculations, the Young's modulus can be measured directly through nano-indentation. A discussion of this technique, along with a presentation of the measurements of these samples and the reduction in uncertainty in the CTE calculations is discussed in the following sections.

5.4 Young's Modulus Measurement Technique

The Young's Modulus, also known as the elastic modulus is the ratio of stress to strain for a material. In essence, it is a measure of how easily a material will change in size, given an applied pressure. Low values of Young's Modulus indicate an elastic material, meaning that the material has a large change in size for a given applied pressure. High values of Young's Modulus indicate an inelastic material, meaning that the material changes in size only very little given an applied pressure.

For bulk materials, this relationship is often measured using a Universal Testing Machine, where a rod of the material is fixed at two ends and pressure is applied to the rod by pulling one end of the material away from the other, elongating the rod. The elongation

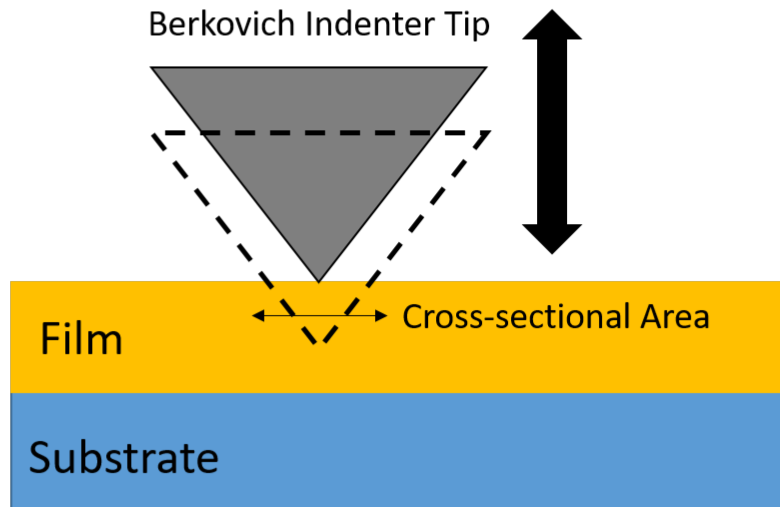

Feature	Size	Berkovich indenter
Semi-angle (α)	65.3 (Degree)	
Apex half angle (θ)	76.9 (Degree)	
Tip radius	200 (nm)	
Height (h)	1 (μm)	
Base length (L)	7.52 (μm)	

Figure 5.16: A diagram of the nano-indentation process, along with a description of the Berkovich tip [7].

length, along with the applied force and cross-sectional are of the rod together give a direct measure of the Young's Modulus.

For thin film materials, it can be expected that the material properties can diverge from the bulk material properties, based on the growth method (film structure and density). Therefore, a different method must be employed in order to measure the Young's Modulus of thin film materials. This method is known as nano-indentation.

Nano-indentation is a method in which a small indenter tip is used to locally deform the exterior layer of the material. For this work, the Berkovich tip was used, and is shown in Figure 5.16. This tip is slowly forced into the material, while the applied force and the penetration depth are monitored. The cross-sectional area of the indenter can be calculated using the geometry of the tip, leading to a direct measure of the material's response to the applied pressure. The measured quantities are the load on the indenter, and the displacement of the indenter, which can be used to calculate the Young's Modulus of the film.

It is important to note that for measurements of thin films, the material properties of the substrate will play a role in the response of the nano-indentation instrument. However, the properties of the substrate can also be measured, and included in the model used by the instrument to calculate the correct properties of the film.

The nano-indentation instrument used in this study was the iNano nano-indenter from NanoMechanics Inc, now part of KLA-Tencor Corporation [57]. This instrument is designed for measurement of thin films, and has the capability to provide 50mN of loading force, with 50um indentation depth. The system is also designed with an integrated microscope so that any imperfections in the surface quality of the film can be identified and the points at which the nano-indenter measures can be chosen based on feedback about the local surface quality. An image of this instrument is shown in Figure 5.17, with the exterior of the instrument shown on the left, and the interior of the instrument shown on the right, where two samples have been loaded for measurement.

Each thin film measurement protocol collected data from 16 measurement sites, and reported the average and the standard deviation of these measurements. The measurement

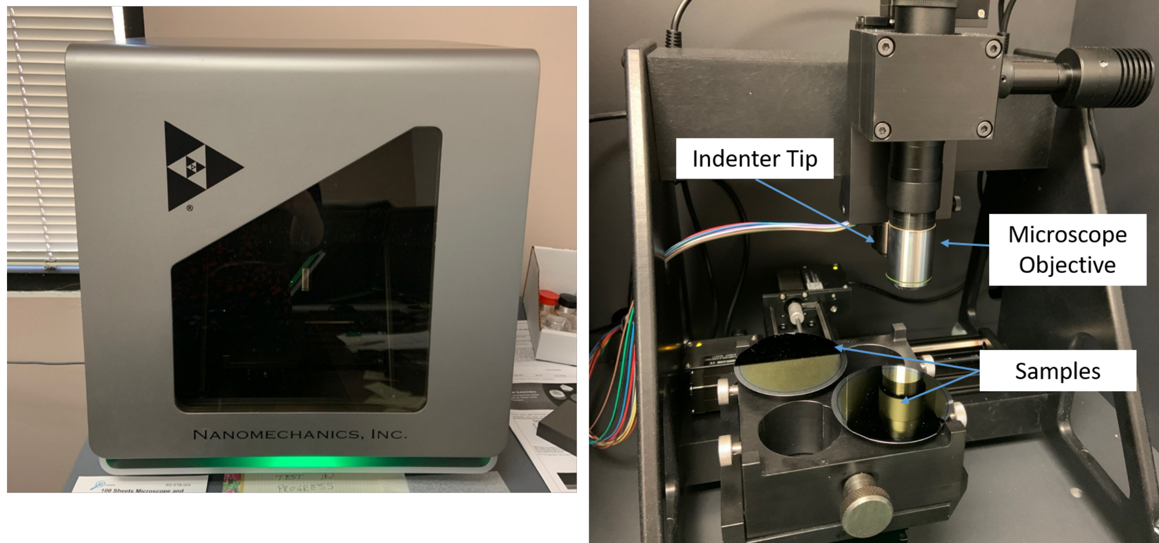

Figure 5.17: Images of the iNano instrument exterior (left) and interior (right).

depth is equal to half of the film thickness. The Young's Modulus of the substrate materials were also measured directly, and incorporated into the thin film model in order to report the most accurate information about the properties of the thin films.

Nano-indentation data from each film was collected using the iNano instrument, and the Young's Modulus is reported as a function of film composition in Figure 5.18, and shown also in Table 5.2.

One observation about these data from the nano-indentation is that they all fall closely along the model of the Rule of Mixtures for composite materials whose endpoints are the average of the two film measurements of SiO_2 and Ta_2O_5. These data also have uncertainties which are between 8 and 30 times smaller than the uncertainties calculated in the two-substrate method, which will be useful in reducing the uncertainty in the calculations of the film CTE.

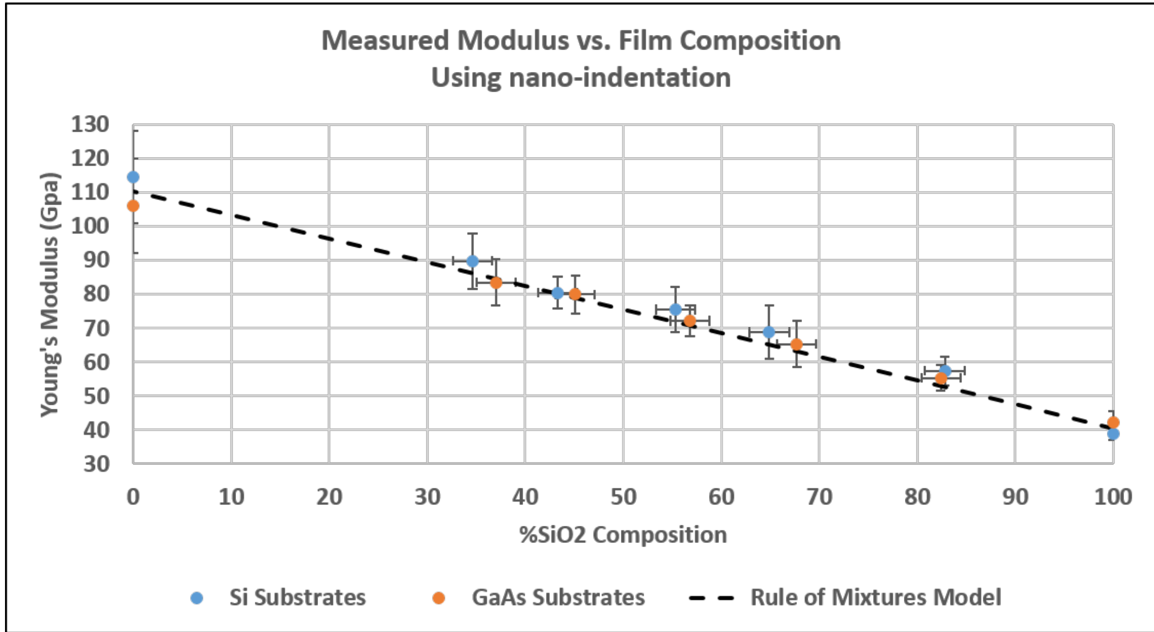

Figure 5.18: Young's Modulus determined using nano-indentation as a function of film composition. The dashed line indicates the "Rule of Mixtures" model.

Table 5.2: Measured Young's Modulus, using the iNano nanoindenter, for both Si substrates and GaAs substrates, as compared to the calculated modulus using the two-substrate method. All values are reported in GPa unless otherwise stated.

	Si Subs: iNano		GaAs Subs: iNano		Two-Substrate Method	
Target Powers	Modulus	Stdev	Modulus	Stdev	Modulus	Stdev
0WTa, 200WSi	39.03	2.08	42.09	3.38	46.17	64.28
30WTa, 200WSi	57.47	4.21	55.39	3.91	72.59	106.76
50WTa, 200WSi	68.80	7.80	65.29	6.76	170.82	73.20
65WTa, 200WSi	75.45	6.64	72.14	4.64	84.79	88.63
80WTa, 200WSi	80.43	4.63	79.93	5.54	143.39	84.12
95WTa, 200WSi	89.79	8.11	83.50	6.92	121.24	120.04
95WTa, 0WSi	114.53	13.50	105.98	13.88	206.07	120.04

The measurements of the Young's Modulus for the SiO_2 films can also be compared to the reported value of the modulus for Fused Silica, which is 71.2-74.8 GPa [51]. These measurements can also be compared to other papers which report the modulus of SiO_2, one of which reportedly found the modulus of their SiO_2 films, grown using dual-ion beam sputtering were 91 GPa [11]. The nano-indentation measurements show that the modulus of these SiO_2 films are closer to 40 GPa, indicating more elastic films.

Similarly, the modulus found using nano-indentation of Ta_2O_5 films can be compared to the calculated in [11], which were reported to be 137-8 GPa. These values are also larger than the measured values for the Ta_2O_5 films fabricated for this study: 106-114 GPa.

As discussed in [11], it is expected that the micro-structure of the film can play a role in the mechanical properties of the thin film. It is expected that the thin film material can have mechanical properties which vary from the bulk material properties, and which can vary based on deposition conditions. This is even indicated as a motivation in the paper to develop methods, used in this work, to characterize the mechanical properties of the thin films. The deposition conditions for the films fabricated under this effort and those made for the referenced paper are different. The result being that the films fabricated under this effort are more elastic.

There are many discussions in the literature about tailoring of the deposition conditions to achieve different intrinsic stresses, however tailoring of the deposition conditions to achieve films of specific elasticity could also be used to tailor the thermal stress in the thin film system. Films which are more elastic are able to withstand a greater stress without damage or fracture, which could be used to create more durable systems.

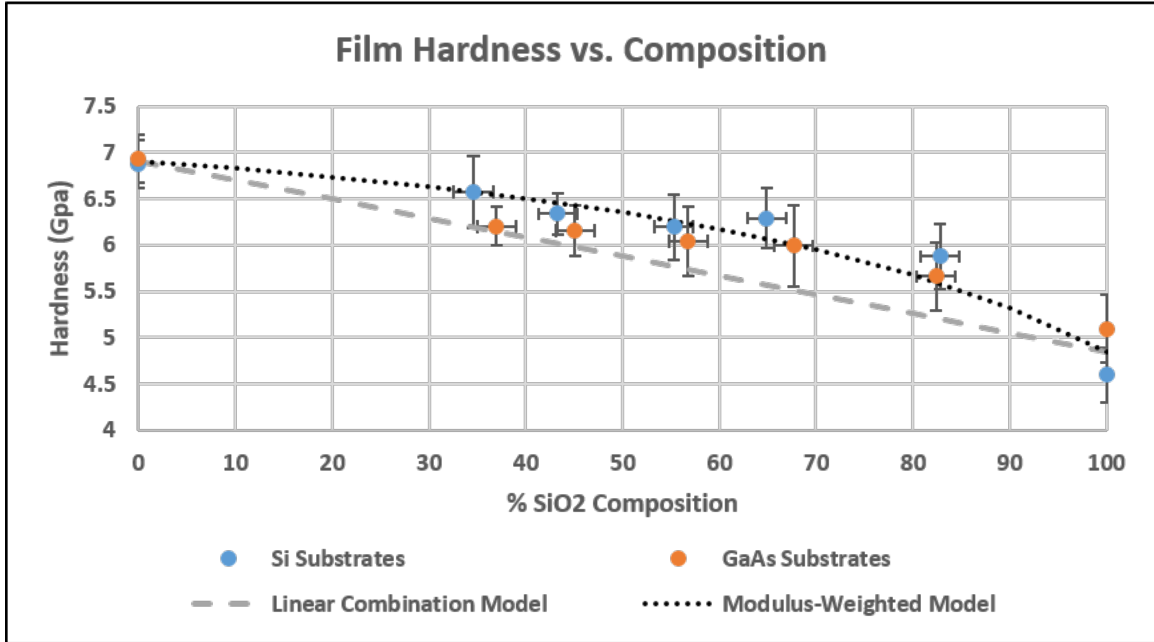

Figure 5.19: The measured Hardness of the films, along with their reported uncertainty, using nano-indentation. The models compare the data with a linear mixing model and a modulus-weighted model.

In addition to the modulus calculations, the iNano instrument also reports film material hardness, which will be reported here for each fabricated film. Hardness is the ability of the material to resist deformation, which can be reported in the units of pressure (GPa). The measurements of the hardness for each film is shown in Figure 5.19 and reported in Table 5.3.

The first observation that comes from these measurements is that Ta_2O_5-rich films exhibit larger hardness values than SiO_2-rich films. Additionally, the manner in which the hardness changes as a function of composition does not appear to be a simple linear combination.

Table 5.3: Measured Hardness, using the iNano nanoindenter, for both Si substrates and GaAs substrates.

	Si Substrates: iNano		GaAs Substrates: iNano	
Target Powers	Hardness (GPa)	Stdev (GPa)	Hardness (GPa)	Stdev (GPa)
0WTa, 200WSi	4.60	0.29	5.10	0.37
30WTa, 200WSi	5.88	0.35	5.66	0.37
50WTa, 200WSi	6.29	0.33	5.99	0.44
65WTa, 200WSi	6.20	0.35	6.04	0.37
80WTa, 200WSi	6.34	0.23	6.16	0.27
95WTa, 200WSi	6.58	0.38	6.20	0.21
95WTa, 0WSi	6.88	0.26	6.94	0.26

In Figure 5.19, two models are posed which demonstrate possible ways in which the hardness of the co-sputtered films might vary with composition. The first is a simple linear combination model, which predicts that the hardness of the composite material is equal to the hardness of the two constituent materials, weighted by their volume fractions. This uses the same principle as the "Rule of Mixtures" model used for the Young's Modulus of the composite materials.

The second model for the hardness of the co-sputtered films as a function of composition follows the principles of the Hall CTE model [6], where the Hardness values are weighted by the Young's Modulus of the film. This is a plausible model for the hardness of the composite materials, as the resistance to deformation (hardness) and the elasticity (extent of deformation with applied load) are related quantities.

Lastly, the measurements of the hardness of the SiO_2 films and the Ta_2O_5 films can be compared to other measurements. The reported hardness of Fused Silica ranges from 4.5-5.0GPa [51], while [50] reports that the hardness of their SiO_2 films are closer to 9.5GPa. This article also reports a measured hardness for Ta_2O_5 of about 7.0GPa. Interestingly, the

measurements of the films fabricated under these efforts match very closely the values of the Ta_2O_5 made in [50], but the films of SiO_2 align more closely with the hardness of Fused Silica.

The finding that the hardness of the composite oxide thin films varies are the Modulus-weighted average of the constituent materials provides a valuable finding for the tailoring of the mechanical properties of thin film coatings. Additionally, the deposition of films which match the hardness of bulk fused silica and other reported Ta_2O_5 film, while having a smaller Young's Modulus (being a more elastic film) could be valuable in the reduction of thermal stress in the thin films, while maintaining the film hardness.

5.5 Single-Substrate Method: Calculation of CTE using Measured Modulus

The direct measurement of the Young's Modulus using nano-indentation for each individual film has significatnly reduced its uncertainty, by up to 30 times. These direct measurements allow for the calculation of the thermo-mechanical properties of each film, using only a single substrate, as outlined in [6, 50]. Additionally, the reduction in uncertainty from these measurements allow for a calculation of the CTE of each film with higher precision than is available for these films using the two-substrate method.

The strengths of the single-substrate method come from being able to calculate the CTE and the Young's Modulus without having to fabricate and measure two identical films on different substrate materials. In the case of this study, where it was discovered that the films grown were not thick enough to induce a curvature change with temperature larger than the instrument noise, there is the additional benefit of increased precision of the calculated CTE values based on the reduction of noise from the modulus measurements.

The theoretical basis for these calculations are outlined in Section 4.3.2, which uses Eqn. 4.16 to calculate the film CTE. For this method, there are still two sources of measurement error which must be accounted for in the calculation of the film CTE uncertainty. These are the uncertainty in the modulus measurements, reported by the nano-indentation instrument, along with the uncertainty in the best-fit slope for curvature versus temperature, as discussed at length in Section 5.1.3.

The same method for handling the two sources of measurement uncertainty is used in these calculations as was outlined in the calculation of the CTE and modulus using the two-substrate method. Both the modulus and the curvature versus temperature are determined by an random-number generator, which outputs a random number which has a weighted distribution equal to a normal distribution whose peak is located at the reported value, and whose standard deviation is the standard deviation of the reported value. These random numbers are used as inputs to the film CTE calculation which is evaluated 2000 times. The average of this distribution of evaluations is reported as the calculated film CTE, while the standard deviation of these 2000 evaluations is reported as the uncertainty in the calculated film CTE.

For the two-substrate method, only a single film CTE value was reported for each composition, as both the films on the Si substrates and those on the GaAs substrate contributed to the calculation of the CTE. For the single-substrate method, the film CTE can be calculated for each of the 14 fabricated samples, which allows for the comparison of two CTE calculations for the films of given composition.

A plot of the calculated CTE vs. film composition, using this Single-Substrate method is shown in Figure 5.20, and reported in Table 5.4. The results from all 14 samples are

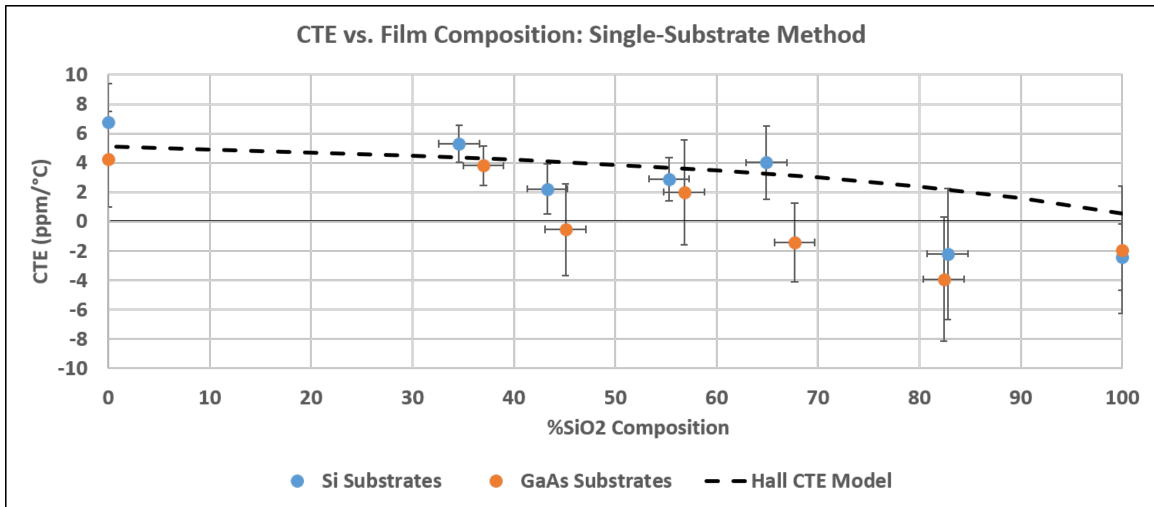

Figure 5.20: Plot of the CTE vs. film composition, as calculated using the Single-Substrate method with Young's modulus measured with nano-indentation.

Table 5.4: Calculated CTE and uncertainty of each film using the Single-Substrate Method. All values are reported in units of ppm/°C unless otherwise stated.

	Si Substrates		GaAs Substrates	
Target Powers	CTE (ppm/°C)	Stdev	CTE (ppm/°C)	Stdev
0WTa, 200WSi	-2.44	2.26	-1.93	4.34
30WTa, 200WSi	-2.20	4.45	-3.92	4.24
50WTa, 200WSi	4.01	2.48	-1.43	2.66
65WTa, 200WSi	2.89	1.46	2.00	3.58
80WTa, 200WSi	2.22	1.70	-0.54	3.13
95WTa, 200WSi	5.29	1.25	3.81	1.33
95WTa, 0WSi	6.76	2.64	4.24	3.24

evaluated and compared to the Hall CTE Model, where the SiO_2 CTE value is that of fused silica (0.55 ppm/°C), and the Ta_2O_5 CTE value is the reported value from (5.1 ppm/°C) [6].

The first observation is the uncertainty in the reported CTE values has decreased significantly from the incorporation of the Young's Modulus from the nano-indentation measurements, by up to 60 times. This demonstrates how the two-substrate method is very sensitive to uncertainty in the curvature versus temperature measurements, and how the incorporation of the two error sources compound together to magnify the uncertainty in these reported values. To belabor this point, the reduction in the uncertainty in the Young's Modulus values was reduced up to 30 times by using the nano-indentation method for these thin films, due to the change in curvature with temperature being below the noise threshold of the instrument. The reduction in uncertainty of the CTE calculations was reduced up to 60 times, due to the incorporation of the more precise modulus measurements. This is due to the high sensitivity of the CTE calculations to the measurement error, when using the two-substrate method.

Another observation of these calculated values is that for each set of two films with the same (or very similar) composition, the error bars of the two calculated CTE values overlap, with only one exception at approximately 65% SiO_2 whose values come within 0.3 ppm/°C of each other. This indicates general agreement in calculated CTE between the two sets of films. It is possible that for the set of films which do not match, that the nature of the random number generator for the calculation of the CTE and its uncertainty played a role, as high error in this case means a very broad normal distribution. It is also worth noting that this is the set of films whose reported composition is the most different between the

two films (2.8%). This might also contribute to the difference between the two measured calculated values of the CTE.

This measurement set is the first test of the Hall CTE Model for the application of co-sputtered thin films. While the individual uncertainty of each measurement is still high due to the small ratio of film-to-substrate thickness, trends in the data can still be analyzed. Figure 5.20 shows that 10 out of the 14 points have error bars which fall on the Hall CTE Model, indicating that this is a reasonable description of the films. It should be noted that each of these calculated values which do not intersect with this Hall CTE Model report values of CTE which are negative, indicating that the film is contracting with increasing heat. It is not the belief of the author that a negative CTE is a realistic scenario for the materials presented in this work, and that it is an artifact of the high measurement uncertainty. Indeed, 13 of the 14 samples have error bars which allow for positive values of the film CTE, and the only film which has this exception comes to within 0.18 ppm/°C. It is possible that for the film which does not allow a positive value of CTE, the nature of the random number generator for the calculation of the CTE and its uncertainty played a role in this film maintaining its negative reported value, as the high uncertainty indicates broad distributions.

These data generally support the use of the Hall CTE Model as a way to predict the CTE of a co-sputtered oxide film. The trend of increasing CTE with higher Ta_2O_5 composition supports the idea that the CTE of the Ta_2O_5 films will be larger than the SiO_2 films. Lastly, it has been demonstrated that direct measurements of the Young's Modulus, using nano-indentation can be used as a method to increase the precision in the calculated CTE of the films, when the uncertainty is high.

CHAPTER VI

CONCLUSION

This study set out to learn about the thermo-mechanical properties of composite-oxide thin films. The film properties, namely the coefficient of thermal expansion (CTE) and the Young's Modulus of the films in comparison with the properties of the substrate drive the extent of thermal stress in a system. Generally, research regarding thin film stress focuses on the intrinsic stress in the film, which is a consequence of the film deposition conditions. However, there are two categories of systems where thermal stress can be on the same order or magnitude or larger than the intrinsic stress in the system: systems designed to experience high temperature fluctuations, and systems where the thermo-mechanical properties of the film and substrate are very different.

There are studies which demonstrate these thermo-mechanical properties of single-materials thin films [6, 11, 50], however these studies focus only on single-material thin film layers. Not all thin film applications use discrete single-material layers, and can include graded-index films where two materials are co-deposited together to form a composite. The optical properties of these systems are well-known and used in creating novel interference filters [18], but the thermo-mechanical properties which play a role in the durability of these films for incorporation into systems has only begun to be explored with this work.

During the course of this research, two matching sets of films were deposited, one onto silicon substrates, the other onto gallium arsenide substrates. The two sets of films ranged in composition from SiO_2, a commonly used low-index dielectric material, to Ta_2O_5, a commonly used high-index optical material. A total of 14 films were fabricated using Reactive Pulsed-DC Magnetron Sputtering, by varying the power to the tantalum target. High reflectance at the laser wavelength of the thermal stress instrument was a high priority, so

the physical thickness of each film was targeted to allow for a constant optical thickness of 330nm across all of the samples. In-situ ellipsometry was used in real-time during deposition to achieve the targeted optical thickness to within 30nm.

After deposition of these series of films, ex-situ variable-angle spectroscopic ellipsometry (VASE) was used. These measurements use the properties of the polarization state of light reflected from the film to calculate its physical thickness, its index dispersion, and its surface roughness. Additionally, based on the reported index dispersion, and using the Bruggeman Effective Medium Theory, an estimate of the film compositions could be determined. Additionally, energy-dispersive X-Ray spectroscopy (EDX), was attempted for these samples in order to more directly measure the film composition. However during measurement, it was determined that the difference between the silicon and tantalum energy lines were below the instrument resolution, making it an unreliable method of determining the composition for SiO_2-Ta_2O_5 films. Therefore, the film composition reported in this work used the results from the optical measurements.

After optical characterization of the films, the thermal stress in the film-substrate system was measured by calculating the curvature change with temperature from parallel beams reflected from the film surface. Measurement of the film stress must be measured indirectly by its effect on the substrate. Gerald Stoney was the first to express this relationship analytically in 1909 [48], and the principles that he outlined over 100 years ago are still being used today to investigate the material properties of thin films.

It is expected that the materials involved will have a constant CTE in the measurement temperature range from 0-100°C, leading to a linear relationship between the substrate curvature and the temperature. However, during analysis of the thermal stress in the film-

substrate system, the fits showed high variance from a linear model. Both the data and the system were carefully investigated, with modifications incorporated in the measurement protocol to reduce uncertainty from systematic sources. After careful examination, it was determined that the source of the high variance from the linear model was because the measurements were close to the instrument's noise limits.

The factors that contribute to an increase in signal were investigated, and a model was built which inputs estimates for film and substrate material properties and outputs the required film thickness that must be fabricated in order to achieve a signal which is equal to the instrument noise. This was used to evaluate the samples fabricated for this study, and can be used in the future to guide a design of experiments.

Additionally, data from thicker films of SiO_2 and Ta_2O_5 which were grown under a different program and measured using the same instrument were discussed [6]. The data from these samples further supports the model and hypothesis laid out that the instrument noise is around 0.038 pixels/°C, and that thicker films can produce higher-precision measurements due to an increase in the signal-to-noise ratio.

Future work can incorporate the knowledge gained in this study, including the in-depth investigation of the instrument noise threshold to choose an appropriate film and substrate thickness to reduce the uncertainty in the measurements of these film materials, and others.

It is recommended that the single-substrate method is used in the future, in order to maintain the ability to measure both CTE and Young's Modulus of a single film, removing the need to deposit two identical films. Additionally, it may be of interest measure the thermo-mechanical properties of films with relatively small physical thickness. This can be done by designing experiments based on the instrument sensitivity threshold, while

maintaining films having physical thicknesses representative of what might be included in optical interference filter designs.

If maintaining film physical thicknesses of 100-300 nm is important in future experiments, it is recommended to try decreasing the substrate thickness. This factor has the greatest ability to decrease the measurement uncertainty. However, there may be some practical limit to how thin of a substrate can be utilized (handling challenges, availability/cost, flatness). Additionally, it is important to keep in mind that Stoney's equation is valid only for circumstances where the film thickness is orders of magnitude less than the substrate thickness. If increasingly thin substrates are pursued, this must be carefully evaluated. To combat some of this, the measurement temperature range can be expanded by a factor of two, which will increase the measurement precision of thin films.

The CTE and Young's Modulus of the films were determined using two different methods. The first of these methods utilized the same film material grown on two different substrate materials. With the assumption that the two films are indeed the same, a thermal stress equation from each film-substrate system can be solved to find both the CTE and Young's Modulus of the film material using the same data sets. The measured values for the inputs to these equations were the curvature versus temperature of the film-substrate systems.

For these measurements in particular, it was important to properly characterize the uncertainty in the CTE and Young's Modulus calculations, as the uncertainty in the calculated values were the result of the uncertainty in two measurement sources: curvature versus temperature on the silicon and the gallium arsenide substrates. In order to incorporate both sources of uncertainty into the calculations, a method was developed which used a

random number generator, weighted to a normal distribution with the center at the best-fit value and the standard deviation equal to the standard error in the fit. Then the reported CTE and modulus value was the average of 2000 iterations of calculations of the CTE and modulus, using these random numbers as inputs for the curvature versus temperature. The uncertainty reported in the CTE and modulus value was then considered to be the standard deviation in these 2000 iterations.

The calculations of the CTE and Young's Modulus using the two-substrate method showed high uncertainty, beyond the magnitude of effect which was attempting to be understood. An understanding was developed of the high-sensitivity of the two-substrate method to uncertainties in the measurements.

Luckily, a second method could be used to determine the Young's Modulus of the films directly, through nano-indentation, reducing the uncertainty in the modulus by up to a factor of 30. Using this measurement method, it was shown that the modulus of the films vary linearly with composition, as predicted by the "Rule of Mixtures" [56].

Additionally, the nano-indentation provided information about the film hardness, which was shown to vary non-linearly as the volume-fraction weighted by the Young's Modulus. This finding would be worth further investigation in the future. An in-depth comparison on this finding to other models for composite materials would be of interest.

Lastly, the CTE could be calculated again, using the more precise measurements of film modulus from nano-indentation. The same method was used in these calculations to incorporate the source of uncertainty from the curvature versus temperature measurements, along with the uncertainty from the nano-indentation measurements. Due to the increase

in measurement precision, the uncertainty in the CTE calculations was reduced by up to a factor of 60.

The understanding of the sensitivity of the two methods (two-substrate, and single-substrate) to measurement uncertainty was developed in this work. Future film measurements can be evaluated using this new lens, in order to determine the most appropriate method to use for calculating film thermo-mechanical properties.

While the uncertainty in the calculated CTE values was still high due to the low signal-to-noise ratio for these samples, evaluation of the data can be used to determine trends. It has been postulated by Randy Hall of Conejo Valley Research that the effective CTE of a multi-layer thin film can be expressed as a modulus-weighted average, based on the volume fraction of the two constituent materials [6]. This Hall CTE Model is used here as a prediction of the CTE of the co-sputtered composite materials. The results of CTE versus composition from the single-substrate method are in general agreement with this model, when applied to film composition. Further work will need to be done to confirm this finding with high precision, however this work provides a first step to understanding the variation of thermo-mechanical properties of thin films as a function of composition, and proposes a model for the CTE of these composite films.

BIBLIOGRAPHY

[1] I. Safi, "Recent aspects concerning DC reactive magnetron sputtering of thin films: a review," *Surface and Coatings Technology*, vol. 127, no. 2-3, pp. 203–218, May 2000. [Online]. Available: https://linkinghub.elsevier.com/retrieve/pii/S0257897200005661

[2] M. Hughes, "What Is Sputtering? Magnetron Sputtering?" Nov. 2014. [Online]. Available: http://www.semicore.com/what-is-sputtering

[3] Trumpf Huettinger Inc., "TruPlasma DC 4002 DC Generator User Manual," 2016.

[4] "Interaction of Light and Materials," library Catalog: www.jawoollam.com. [Online]. Available: https://www.jawoollam.com/resources/ellipsometry-tutorial/interaction-of-light-and-materials

[5] R. G. Brown, "Anomalous Dispersion, and Resonant Absorption," Dec. 2007. [Online]. Available: https://webhome.phy.duke.edu/ rgb/Class/phy319/phy319/node50.html

[6] W. H. Southwell, R. L. Hall, J. E. Peeples, and G. Jones, "Thermo-Mechanical Stress Design Optimization in Optical Coatings," ECMS Technical Report AFRL-RX-WP-TR-2021-0036, Jun. 2021.

[7] A. Karimzadeh, S. S. Rahimian Koloor, M. R. Ayatollahi, A. R. Bushroa, and M. Yahya, "Assessment of Nano-Indentation Method in Mechanical Characterization of Heterogeneous Nanocomposite Materials Using Experimental and Computational Approaches," *Scientific Reports*, vol. 9, Oct. 2019.

[8] Y. Kovo, "3.0 Power," Mar. 2020. [Online]. Available: http://www.nasa.gov/smallsat-institute/sst-soa-2020/power

[9] mars.nasa.gov, "Mars Facts | All About Mars," library Catalog: mars.nasa.gov. [Online]. Available: https://mars.nasa.gov/all-about-mars/facts

[10] "Ask an Astronomer," library Catalog: coolcosmos.ipac.caltech.edu. [Online]. Available: http://coolcosmos.ipac.caltech.edu/ask/168-What-is-the-temperature-on-the-Moon-

[11] E. etinrg, "A new method to experimentally determine the thermal expansion coefficient, Poissons ratio and Youngs modulus of thin films," *Journal of Materials Science*, vol. 44, no. 8, pp. 2167–2170, Apr. 2009. [Online]. Available: https://doi.org/10.1007/s10853-009-3365-3

[12] M. Hla, R. Vernhes, O. Zabeida, J.-E. Klemberg-Sapieha, and L. Martinu, "Reactive HiPIMS deposition of SiO2/Ta2O5 optical interference filters," *Journal of Applied Physics*, vol. 116, no. 21, p. 213302, Dec. 2014, publisher: American Institute of Physics. [Online]. Available: http://aip.scitation.org/doi/full/10.1063/1.4903285

[13] M. Wuttig and N. Yamada, "Phase-change materials for rewriteable data storage," *Nature Materials*, vol. 6, no. 11, pp. 824–832, Nov. 2007. [Online]. Available: http://www.nature.com/articles/nmat2009

[14] P. Guo, A. M. Sarangan, and I. Agha, "A review of germanium-antimony-telluride phase change materials for non-volatile memories and optical modulators," *Applied Sciences*, vol. 9, no. 3, 2019. [Online]. Available: https://www.mdpi.com/2076-3417/9/3/530

[15] I.-M. Park, J.-K. Jung, S.-O. Ryu, K.-J. Choi, B.-G. Yu, Y.-B. Park, S. M. Han, and Y.-C. Joo, "Thermomechanical properties and mechanical stresses of Ge2Sb2Te5 films in phase-change random access memory," *Thin Solid Films*, vol. 517, no. 2, pp. 848–852, Nov. 2008. [Online]. Available: https://linkinghub.elsevier.com/retrieve/pii/S0040609008010201

[16] "Coefficients of Linear Thermal Expansion - Silver CTE | MSE Supplies L." [Online]. Available: https://www.msesupplies.com/pages/list-of-thermal-expansion-coefficients-cte-for-natural-and-engineered-materials

[17] S. Song, Z. Song, L. Wu, B. Liu, and S. Feng, "Stress reduction and performance improvement of phase change memory cell by using Ge2Sb2Te5TaOx composite films," *Journal of Applied Physics*, vol. 109, no. 3, p. 034503, Feb. 2011, publisher: American Institute of Physics. [Online]. Available: https://aip.scitation.org/doi/full/10.1063/1.3544432

[18] B. G. Bovard, "Rugate filter theory: an overview," *Applied Optics*, vol. 32, no. 28, pp. 5427–5442, Oct. 1993, publisher: Optical Society of America. [Online]. Available: https://www.osapublishing.org/ao/abstract.cfm?uri=ao-32-28-5427

[19] W. H. Southwell, "Gradient-index antireflection coatings," *Optics Letters*, vol. 8, no. 11, p. 584, Nov. 1983. [Online]. Available: https://www.osapublishing.org/abstract.cfm?URI=ol-8-11-584

[20] D. E. Aspnes, "Optical properties of thin films," *Thin Solid Films*, vol. 89, no. 3, pp. 249–262, Mar. 1982. [Online]. Available: http://www.sciencedirect.com/science/article/pii/0040609082905909

[21] M. Cevro, "Ion-beam sputtering of (Ta2O5)x (SiO2)1x composite thin films," *Thin Solid Films*, vol. 258, no. 1, pp. 91–103, Mar. 1995. [Online]. Available: http://www.sciencedirect.com/science/article/pii/0040609094063567

[22] Y. Pu, Z. Qiao, G. Wang, F. Qiu, P. Ma, and S. Wang, "Stress reduction and structural properties of Ta2O5/SiO2 mixture films produced by ion-beam sputtering," in *8th International Symposium on Advanced Optical Manufacturing and Testing Technologies: Advanced Optical Manufacturing Technologies*, vol. 9683. International Society for Optics and Photonics, Oct. 2016, p. 968323. [Online]. Available:

https://www-spiedigitallibrary-org.libproxy.udayton.edu/conference-proceedings-of-spie/9683/968323/Stress-reduction-and-structural-properties-of-Ta2O5-SiO2-mixture-films/10.1117/12.2244163.short

[23] A. Sarangan, "Nanofabration," in *Fundamentals and Applications of Nanophotonics*, J. W. Haus, Ed. Woodhead Publishing, Jan 2016.

[24] ——, *Nanofabrication: Principles to Laboratory Practice.* CRC Press, Oct. 2016.

[25] "Magnetron sputtering," library Catalog: www.fhr.biz. [Online]. Available: https://www.fhr.biz/en/thin-film-technology/sputtering-technology/magnetron-sputtering/

[26] M. Schoff, "Sputter Target Erosion and its Effects on Long Duration DC Magnetron Sputter Coating," Ph.D. dissertation, University of California, San Diego, Center for Energy Research, Jun. 2009.

[27] J. Musil, P. Baroch, J. Vlek, K. Nam, and J. Han, "Reactive magnetron sputtering of thin films: present status and trends," *Thin Solid Films*, vol. 475, no. 1-2, pp. 208–218, Mar. 2005. [Online]. Available: https://linkinghub.elsevier.com/retrieve/pii/S0040609004009332

[28] "RF Sputtering." [Online]. Available: https://angstromengineering.com/tech/magnetron-sputtering/rf-sputtering/

[29] AJA International, "Stiletto & CT-X Series Magnetron Sputtering Sources Installation & Operation Manual," Sep. 2004.

[30] "Thermal mass flow sensors, theory of operation & design," Sep. 2018. [Online]. Available: https://www.omega.com/en-us/resources/thermal-mass-flow-working-principle-theory-and-design

[31] H. Tompkins and E. A. Irene, *Handbook of Ellipsometry.* William Andrew, Jan. 2005, google-Books-ID: 6PQf1fSzHHEC.

[32] H. G. Tompkins, *A User's Guide to Ellipsometry.* Courier Corporation, Jul. 2006, google-Books-ID: NH71DAAAQBAJ.

[33] H. Fujiwara, *Spectroscopic Ellipsometry: Principles and Applications.* John Wiley & Sons, Sep. 2007, google-Books-ID: tTMn0NKcpjsC.

[34] E. Collett, *Field Guide to Polarization.* SPIE Digital Library, Sep. 2005, publisher: International Society for Optics and Photonics. [Online]. Available: https://www-spiedigitallibrary-org.libproxy.udayton.edu/ebooks/FG/Field-Guide-to-Polarization/Classical-Measurement-of-the-Stokes-Parameters/Classical-Measurement-of-the-Stokes-Parameters/10.1117/3.626141.p16

[35] V. Lucarini, J. J. Saarinen, K.-E. Peiponen, and E. M. Vartiainen, *Kramers-Kronig Relations in Optical Materials Research.* Springer Science & Business Media, Apr. 2005, google-Books-ID: U21PMIXyk7IC.

[36] G. E. Jellison and F. A. Modine, "Parameterization of the optical functions of amorphous materials in the interband region," *Applied Physics Letters*, vol. 69, no. 3, pp. 371–373, Jul. 1996. [Online]. Available: http://aip.scitation.org/doi/10.1063/1.118064

[37] Z. Guo, W. Yuan, Y. Sun, Z. Cai, and Z. Qiao, "Thermodynamic Assessment of the Si-Ta and Si-W Systems," *Journal of Phase Equilibria and Diffusion*, vol. 30, no. 5, p. 564, Sep. 2009. [Online]. Available: https://doi.org/10.1007/s11669-009-9579-x

[38] M. E. Schlesinger, "The Si-Ta (silicon-tantalum) system," *Journal of Phase Equilibria*, vol. 15, no. 1, pp. 90–95, Feb. 1994. [Online]. Available: http://link.springer.com/10.1007/BF02667688

[39] A. G. Revesz and T. D. Kirkendall, "FilmSubstrate Interaction in Si/Ta and Si / Ta2 O 5 Structures," *Journal of The Electrochemical Society*, vol. 123, no. 10, pp. 1514–1519, Oct. 1976. [Online]. Available: https://iopscience.iop.org/article/10.1149/1.2132629

[40] A. Christou and H. M. Day, "Silicide formation and interdiffusion effects in Si-Ta, SiO2-Ta AND Si-PtSi-Ta thin film structures," *Journal of Electronic Materials*, vol. 5, no. 1, pp. 1–12, Feb. 1976. [Online]. Available: https://doi.org/10.1007/BF02652882

[41] G. A. Niklasson and C. G. Granqvist, "Effective medium models for the optical properties of inhomogeneous materials," *Applied Optics*, vol. 20, no. 1, p. 5, Jan. 1981.

[42] T. C. Choy, *_USEffective Medium Theory: Principles and Applications.* Oxford University Press, publication Title: Effective Medium Theory Section: Effective Medium Theory. [Online]. Available: http://www.oxfordscholarship.com/view/10.1093/acprof:oso/9780198705093.001.0001/acprof-9780198705093-chapter-1

[43] E. D. Palik, Ed., *Handbook of Optical Constants of Solids.* Elsevier, 1985, vol. 1. [Online]. Available: https://linkinghub.elsevier.com/retrieve/pii/C20090209202

[44] W. H. Southwell, "Coating design using very thin high- and low-index layers," *Applied Optics*, vol. 24, no. 4, pp. 457–460, Feb. 1985, publisher: Optical Society of America. [Online]. Available: https://www-osapublishing-org.wrs.idm.oclc.org/ao/abstract.cfm?uri=ao-24-4-457

[45] A. Nanakoudis, "EDX Analysis - SEM - EDS Analysis - Accelerating Microscopy," Nov. 2019. [Online]. Available: https://www.thermofisher.com/blog/microscopy/edx-analysis-with-sem-how-does-it-work/

[46] "JEOL Posters | Browse the Collection." [Online]. Available: https://www.jeolusa.com/RESOURCES/JEOL-Posters

[47] H. Windischmann, "Intrinsic stress in sputter-deposited thin films," *Critical Reviews in Solid State and Materials Sciences*, vol. 17, no. 6, pp. 547–596, Jan. 1992, publisher: Taylor & Francis _eprint: https://doi.org/10.1080/10408439208244586. [Online]. Available: https://doi.org/10.1080/10408439208244586

[48] G. G. Stoney, "The tension of metallic films deposited by electrolysis," *Proceedings of the Royal Society of London. Series A, Containing Papers of a Mathematical and Physical Character*, vol. 82, no. 553, pp. 172–175, May 1909, publisher: Royal Society. [Online]. Available: http://royalsocietypublishing.org/doi/abs/10.1098/rspa.1909.0021

[49] "TLP Library Coating mechanics - The biaxial modulus." [Online]. Available: https://www.doitpoms.ac.uk/tlplib/coating_mechanics/biaxial.php

[50] E. Cetinorgu, B. Baloukas, O. Zabeida, J. E. Klemberg-Sapieha, and L. Martinu, "Mechanical and thermoelastic characteristics of optical thin films deposited by dual ion beam sputtering," *Applied Optics*, vol. 48, no. 23, pp. 4536–4544, Aug. 2009, publisher: Optical Society of America. [Online]. Available: https://www.osapublishing.org/ao/abstract.cfm?uri=ao-48-23-4536

[51] "Properties: Silica - Fused Silica (Silicon Dioxide)." [Online]. Available: https://www.azom.com/properties.aspx?ArticleID=1387

[52] "Gallium Arsenide (GaAs) Semiconductors," Mar. 2013, section: Materials Article. [Online]. Available: https://www.azom.com/article.aspx?ArticleID=8349

[53] "Thermal properties of Silicon (Si)." [Online]. Available: http://www.ioffe.ru/SVA/NSM/Semicond/Si/thermal.html

[54] A. Elements, "Silicon Wafer." [Online]. Available: https://www.americanelements.com/silicon-wafer-7440-21-3

[55] C.-L. Wu, Y.-J. Hung, R. Fan, D.-H. Ou, J.-Y. Huang, T.-H. Yen, Y.-J. Chiu, M.-H. Shih, Y.-Y. Lin, A.-K. Chu, and C.-K. Lee, "Tantalum pentoxide (Ta_2O_5) based athermal micro-ring resonator," *OSA Continuum*, vol. 2, no. 4, p. 1198, Apr. 2019. [Online]. Available: https://www.osapublishing.org/abstract.cfm?URI=osac-2-4-1198

[56] "Derivation of the rule of mixtures and inverse rule of mixtures." [Online]. Available: https://www.doitpoms.ac.uk/tlplib/bones/derivation_mixture_rules.php

[57] "iNano Nanoindentation | Indentation Hardness." [Online]. Available: https://www.kla-tencor.com/products/instruments/nanoindenters/inano